Dissertation

Non-Stationarity in Vehicular Wireless Channels

ausgeführt zum Zwecke der Erlangung des akademischen Grades
eines Doktors der technischen Wissenschaften

eingereicht an der
Technischen Universität Wien
Fakultät für Elektrotechnik und Informationstechnik

von

Laura Bernadó

Wien, 23. April 2012

TECHNISCHE
UNIVERSITÄT
WIEN
Vienna University of Technology

Supervisor

Prof. Christoph Mecklenbräuker

Institut für Nachrichtentechnik und Hochfrequenztechnik

Technische Universität Wien, Austria

Examiner

Prof. Claude Oestges

Institute of Information and Communication Technologies,

Electronics and Applied Mathematics (ICTEAM)

Ecole Polytechnique de Louvain, Louvain-la-Neuve, Belgium

Kurzfassung

Bei der Funkkommunikation mit Fahrzeugen ändern sich die Wellenausbreitungsverhältnisse schnell. Der Schwundprozess des Fahrzeugkommunikationskanals ist zeit- und frequenzselektiv. Seine statistischen Eigenschaften sind nur für eine endliche Zeitdauer und eine endliche Bandbreite konstant bzw. schwach stationär. Die Gültigkeit der schwachen Stationarität im Zeitbereich (wide sense stationarity assumption, WSS), und im Frequenzbereich (uncorrelated scattering assumption, US) ist also begrenzt und der Schwundprozess des Fahzeugkommunikationskanals somit nicht stationär (non-WSSUS). Trotzdem kann ein nicht-stationärer Prozess in aufeinanderfolgende Stationariätsregionen aufgeteilt werden für die sich statistische Momente berechnen lassen.

In dieser Dissertation schätze ich die lokale zeit- und frequenzabhängige Streufunktion aus einer kurzen Beobachtung des nicht-stationären Schwundprozesses. Für die Schätzung der lokalen Streufunktion (local scattering function, LSF), einem zweidimensionalen Leistungsdichtespektrum, berechne ich den Mittelwert orthogonal gewichteter Einzelspektren. Ich benutze Funkkanalmessdaten, die während der DRIVEWAY09 Messkampagne aufgenommen wurden. DRIVEWAY09 konzentriert sich auf sicherheitsrelevante Verkehrsszenarien für intelligente Transportsysteme (ITS). Zuerst definiere ich eine *minimale Stationaritätsregion* und ich präsentiere eine optimale Parametrisierung des LSF Schätzers. Dafür wende ich die Struktur eines zwei-dimensionalen Wiener Filters an. Ich zeige, dass es eine optimale Parametrisierung des Schätzers gibt, die einen guten Kompromiss zwischen mittlerem quadratischen Fehler (mean square error, MSE) und Berechnungskomplexität liefert.

Weiters untersuche ich die Ausdehnung der *minimalen Stationaritätsregion*. Ich schlage vor, zwei spektrale Metriken zu benutzen, die zwei benachbarte LSFs vergleichen, um einen WSS und einen US-Test durchzuführen. Diese zwei Metriken sind die spektrale Divergenz und die Kollinearität. Ich beweise, dass der Schwundprozess in der Fahrzeugkommunikation stark non-WSS ist. Auerdem zeige ich zum ersten Mal (nach meinem besten Wissen) auch das non-US Verhalten des Funkkanals hauptsächlich in Szenarien, die reich an Streuung sind. Die *minimale Stationaritätsregion* hat eine Ausdehnung von 40 ms im Zeitbereich und 40 MHz im Fre-

quenzbereich.

Ich führe eine stochastische Charakterisierung der zeitveränderlichen statistischen Kanalparameter von Fahrzeugkommunikationskanälen durch. Dies sind das erste Moment, der K-Faktor, und die zweiten Momente, die Dispersion im Verzögerungs- und Dopplerbereich. Für die stochastische Charakterisierung wird eine bi-modale Gaussche Mischverteilung (Gaussian mixture) verwendet. Diese Verteilung ist für die Beschreibung der Kanalparameter geeignet, weil sie gleichzeitig die Bedingungen bei einer direkten Sichtverbindung (line of sight, LOS) und ohne Sichtverbindung (non-LOS) darstellen kann.

Der Schwundprozess der Einhüllenden der Kanalkomponente mit der kürzesten Verzögerung hat eine Rice-Verteilung, mit einem veränderlichen K-Faktor. Spätere Kanalkomponenten sind meistens Rayleigh verteilt. Ich demonstriere, dass der K-Faktor variabel in Zeit, Frequenz und Raum ist. Dies ist begründet durch die Frequenzabhängigkeit der Antennencharakteristik sowie durch die zeitabhängige Anzahl von aktiven Streuern. Ich analysiere die zeitveränderliche Dispersion im Verzögerungs- und Dopplerbereich anhand der LSF. Hohe Werte der Dispersion im Verzögerungsbereich sind bei Szenarien mit vielen Streuobjekten zu beobachten, während hohe Dispersion im Dopplerbereich habe ich vor allem in Vorbeifahrtszenarien gefunden.

Schlielich charakterisiere ich die Streuumgebung des Fahrzeugkommunikationskanals mithilfe des Konzepts des Clusters. Mehrwegekomponenten die im Verzögerungs- und Dopplerbereich eng benachbart sind werden mittels eines Gruppierungsalgorithmus zu Streugruppen zusammengefasst. Diese Streugruppe lässt sich nun einem physischen Streuer zuordnen. Ich wende den Clusteringalgorithmus auf die LSF an, und kann so zeitveränderliche Streugruppenparameter berechnen. Die Clusterform und die Anzahl der Cluster sind vom Reichtum der Streuumgebung und der Geschwindigkeit der Streuer abhängig. Der Cluster mit der kürzesten Verzögerung ist gröer im Vergleich zu den Streugruppen mit gröerer Verzögerung.

Abstract

In vehicular communications, the scattering environment changes rapidly. The fading process in these channels is time-, and frequency-selective, and its statistical properties do not remain constant (stationary) for infinite time and infinite bandwidth. The stationarity in the time domain is defined by the validity of the wide sense stationary (WSS) assumption, and the stationarity in the frequency domain by the validity of the uncorrelated scattering (US) assumption. Hence, the fading process in vehicular channels is non-stationary, i.e. non-WSSUS. However, a non-stationary process can be divided into consecutive stationarity regions with finite extension in time and frequency where the WSS and US assumptions are valid, allowing to calculate its statistical moments.

In this thesis, I estimate the time- and frequency-varying scattering function of an observed non-WSSUS fading process. For that, I use the multi-taper based local scattering function (LSF) estimator. I use radio channel measurements collected in the DRIVEWAY'09 measurement campaign. DRIVEWAY'09 focuses on scenarios for intelligent transportation systems. First, I define a *minimum stationarity region*, and I present an optimal parametrization of the LSF estimator. For that purpose, I use the structure of a two-dimensional Wiener filter and optimize the parameters of the estimator to obtain a low mean square error (MSE) at the output without implying a large computational complexity for the estimation of the LSF. I show that there is an optimal combination of the estimator parameters which provides a good trade-off between MSE and computational complexity.

I also investigate the extension of the *minimum stationarity region*. I propose to use two spectral metrics to be applied to neighboring LSFs in order to perform a WSS and a US test: the spectral divergence and the collinearity. I prove that the fading process in vehicular communications is strongly non-WSS. Furthermore, for the first time (to the authors' knowledge), I show their non-US behavior as well, mainly in scenarios with rich scattering. The dimensions of the *minimum stationarity region* are in the order of 40 ms in time and 40 MHz in frequency.

I stochastically characterize the time-varying vehicular channel parameters in terms of its first order moment (K-factor), and its second order moment (root mean square (RMS) delay and Doppler spread). I fit the obtained data to a bi-modal Gaus-

sian mixture distribution, which is adequate for describing the channel parameters when both line of sight (LOS) and non-line of sight (LOS) conditions occur.

The small-scale fading of the envelope of the first delay bin is Ricean distributed with a varying K-factor. The later delay bins are mostly Rayleigh distributed. I demonstrate that the K-factor can not be assumed to be constant in time, frequency, and space. I show that the frequency-varying antenna radiation patterns as well as the time-varying number of active scatterers are the cause of these variations.

I also analyze the time-varying RMS delay and Doppler spreads, derived from the LSF. High RMS delay spread values are observed in situations with rich scattering, while high RMS Doppler spreads are obtained in drive-by scenarios.

Finally, I characterize the scattering environment by using a clustering algorithm to group multipath components stemming from the same scatterer. I apply the clustering algorithm on the LSF and calculate the time-varying cluster parameters. The cluster shape and the number of clusters depend on the richness of the scattering environment and the velocities of the scatterers. The cluster with the shortest delay has larger extension in comparison with later clusters.

Contents

List of Figures

List of Tables

Acronyms

AOA	angle-of-arrival
AOD	angle-of-departure
BER	bit error rate
CDF	cumulative density function
CIR	channel impulse response
DBSCAN	density-based spatial clustering of applications with noise
DPSS	discrete prolate spheroidal sequences
DSD	Doppler power spectral density
ETSI	European Telecommunications Standards Institute
GoF	goodness of fit
GSCM	geometry-based stochastic channel model
ITS	intelligent transportation systems
KS	Kolmogorov-Smirnov
LOS	line of sight
LSF	local scattering function
MIMO	multiple-input multiple-output
MoM	method of moments
MPC	multipath component
MSE	mean square error

OFDM	orthogonal frequency division multiplexing
PDP	power delay profile
RMS	root mean square
RT	ray-tracing
RX	receiver
SD	spectral divergence
SISO	single-input single-output
SNR	signal to noise ratio
TDL	tapped-delay line
TX	transmitter
US	uncorrelated scattering
V2I	vehicle-to-infrastructure
V2V	vehicle-to-vehicle
WSS	wide sense stationary
WSSUS	wide sense stationary uncorrelated scattering
RC-swt	road crossing - suburban with traffic
RC-swot	road crossing - suburban without traffic
RC-usl	road crossing - urban single lane
RC-uml	road crossing - urban multiple lane
GLO-h	general LOS obstruction - highway
ML-r	merging lanes - rural
TC-st	traffic congestion - slow traffic
TC-atj	traffic congestion - approaching traffic jam
IT	in-tunnel

OB	on-bridge
GoF	goodness of fit

1 Introduction

Nowadays, mobility has become a need and has brought a large number of vehicles driving on the streets. Unfortunately, it has also brought an increase of deaths on the roads. It will become the third cause of deaths worldwide by 2020 if nothing is done to prevent it (in 1990 it was on the ninth position [7]). From the environmental point of view, cars driving in a non-efficient way result in an increase of fuel consumption and CO_2 emissions. Traffic accidents and fuel waste have also an economical impact, which is very harmful in developing countries. Only a joint effort at social, economical, and technological level can contribute to a significant reduction of these negative side effects brought by the increase of mobility.

Vehicular communications are intended to support a wide range of applications ranging from traffic safety, traffic management, to private entertainment. However, priority is given to safety applications such as warning notification or driving assistance. Communications from vehicle-to-vehicle (V2V) and vehicle-to-infrastructure (V2I), where the infrastructure is controlled by the road operator, is envisioned to provide information about the traffic flow such that the traffic accidents rate could be reduced, and vehicles could drive in a more environmentally friendly way.

The radio channel observed in V2V and V2I links is characterized by being highly time-varying and it is described by a *non-stationary* fading process. The low antenna position, the high velocities of transmitter (TX) and receiver (TX), and the large number of scattering objects make the propagation characteristics of the radio waves very peculiar. As a result, the deployment of a trustworthy and highly reliable system for vehicular communications is a challenging task.

A deep understanding of the underlying radio propagation channel is needed for setting up an efficient vehicular communication system. In general, computer simulations allow system design, transceiver testing, etc., in realistic settings without the need for expensive, and difficult to reproduce, field tests. However, such simulations can only be realistic if all their components, including the channel model, reflect the realities of deployment. Hence, system engineers must rely on good channel emulators, for their simulations. Trustworthy channel models can only be derived after observing and investigating the radio channel itself, i.e. measuring it.

In this thesis, we provide an extensive parameter characterization of the vehicular

radio channel, taking into account its non-stationarity.

1.1 State of the Art

In this section, we review the state of the art concerning the vehicular radio channel topics that is relevant for this thesis. In particular, we look at the vehicular radio channel measurements and characterization, channel modeling approaches, and the non-stationarity of the vehicular channel.

1.1.1 Vehicular Measurement Campaigns and Channel Characterization

In order to get a proper understanding of the channel behavior, radio channel measurements have to be conducted. Different types of channel sounders can be used for that purpose. When conducting channel measurements, one needs to bear in mind that in V2V communications, the channel is doubly-selective, meaning that it introduces frequency and time selectivity. Wideband channel sounding can accurately capture these attributes.

Several research groups have been collecting loads of measurement data, which is used for channel characterization and modeling afterwards. The first V2V measurement campaigns used a single-input single-output (SISO) measurement set-up normally with a monopole type antenna mounted on the roof-top of the vehicle.

We can classify the measurement campaigns based on different criteria:

- *Number of used antennas*: The first measurement campaigns considered a TX and a RX equipped with only one antenna, generally a monopole type [8], [9], [10], [11], [12], [13], [14], or [15], among others. However, systems considering several antennas at the TX, at the RX, or at both ends, offer the possibility of exploiting diversity techniques and thus improve the link capacity. Therefore, a multiple-input multiple-output (MIMO) measurement set-up was adopted. More recent measurement campaigns consider multiple antenna elements, such as [16] with 2×2 elements, [17] and [18] with 4×4 elements, or [19] with 30×30 elements.

- *Center frequency*: The first vehicular communications were meant for electronic toll collection operated at the 900 MHz frequency band. Also the first vehicular radio channel measurements were carried out at 900 MHz [8], [9], [20], [21]. Nevertheless, there was a growing interest towards intelligent transportation systems (ITS) communication systems, which aim to improve safety and

intelligent driving on the road. In October 1999, the Federal Communication Comission (FCC) in the United States allocated a frequency band of 75 MHz at 5.9 GHz to be used for ITS. This initiative was followed later in 2008 by the European Telecommunications Standards Institute (ETSI), who also allocated a 30 MHz frequency band at 5.9 GHz. This motivated a measurement frequency change towards the 5 GHz band [22], [13], [23], [24], [17], [14], [19], [16]. Nevertheless, there have also been measurements carried out in the unlicensed band at 2.45 GHz [10], [11], [25].

- *Bandwidth*: Deciding the bandwidth of the measurements determines the kind of data analysis one can do afterwards. Narrowband measurements allow for time-selectivity analysis of the channel as well as small-scale fading characterization, such Doppler spread or K-factor analysis. The first vehicular measurement campaigns often considered narrowband measurements [8], [9], [22], but also later ones did as in [14]. However, V2V communications require wideband channel sounding in order to capture the time- and frequency-selectivity of the channel. Therefore, measurement campaigns have adopted larger bandwidths, for instance the measurement campaign in [15] uses 20 MHz, in [12] and [23] the bandwidth is 50 MHz, 60 MHz are used in [19]. A big step in terms of bandwidth is done by [17] and [18] where 240 MHz are used, and the wideband measurements with the largest bandwidth are provided in [16] and [26] with 1 GHz.

- *Measurement scenarios*: Initially, the settings for conducting measurement campaigns were derived from the cellular communications. The first measurement scenario classification that was made consisted in highway, rural, suburban, and urban scenarios. Many measurements were performed under this definition [22], [10], [11], [12], [24], [15], [27]. Slowly, the research groups realized that the scenario definition should be modified to make it more especific for vehicular communications. Hence, the difference between convoy and oncoming measurements was introduced [17], [16], [19]. However, an even more precise definition of the measurement scenarios for safety-critical oriented situations as in [18], [28], [29], such as intersections or in-tunnel, needs to become more wide spread in its use.

Aside from these general characteristics, each individual measurement campaign is characterized by its particularities, like used vehicles, measured scenarios, used antennas, etc.

Channel parameters	Pathloss exponent n	RMS delay spread σ_τ[ns]	RMS Doppler spread σ_ν[Hz]	Ref.
Highway	–	–	120	[22]
	1.8	247	–	[17]
	1.85	41	92[4]	[15]
	–	141 – 398[2]	761 – 978[2]	[14]
	1.9/4 0[1]	–	–	[30]
	–	165	–	[19]
	–	53/127[3]	–	[31]
	3.59/2.21[7]	–	–	[29]
	1.77/63.3/3.1/3.3 [8]	–	–	[4]
	1.8/3.08 [9]	–	–	[32]
Rural	1.79	52	108[4]	[15]
	–	22	782	[14]
	2.3/4 0[1]	–	–	[30]
	3.18/–[7]	–	–	[29]
Suburban	2.5	–	–	[27]
	2.1/3 9[1]	–	–	[27]
	–	104	–	[19]
	3.5/ – [7]	–	–	[29]
	1.59/64.6/2.1/N/A [8]	–	–	[4]
	1.8/3.00 [9]	–	–	[32]
Urban	–	–	86	[22]
	1.61	47	33[4]	[15]
	–	158 – 321[5]	263 – 341[5]	[14]
	–	373	–	[19]
	–	126/236[6]	–	[31]
	2.88/1.83[7]	–	–	[29]
	1.68/62.0/1.7/1.5 [8]	–	–	[4]

Table 1.1: Channel parameters. [1]breakpoint model, [2]TX-RX separation of 300 – 400 m, [3]low/high traffic density, [4]median value, [5]TX-RX separation of 200 – 600 m, [6]antenna inside/outside the car, [7]on-coming/convoy traffic, [8]$n/PL_0/\sigma/PL_c$ from equation (5) in [4], [9]LOS/discrete scatterer contributions.

The next step that follows data collection is parameter extraction, which will then be used for channel modeling. All the measurement campaigns presented previously extracted parameters describing fading characteristics. The most common ones are the pathloss exponent, the root mean square (RMS) delay and Doppler spreads, the distribution of the signal envelope, the power delay profile (PDP), and the Doppler spectra.

The pathloss describes the signal attenuation due to the propagation distance and shadowing from objects like other vehicles, buildings etc. The RMS delay spread expresses how the channel disperses the signal in time, and similarly, the RMS Doppler spread describes the dispersion of the signal in the frequency domain. The RMS delay spread indicates the severity of the frequency selectivity, while the time selectivity is reflected by the RMS Doppler spread

Investigations on the small-scale fading statistics carried out for vehicular communications at the 5 GHz frequency band can be found in [33], [25], [22], [27], [19]. It is a general finding that the amplitude of the first delay bin follows a Ricean distribution. In [33] and [19], a V2V communication link is considered for a highway scenario. Urban scenario results are presented in [25], [22], [27] but always considering convoy measurements. All these contributions assume a constant K-factor.

Pathloss exponent values have been found between 1.59 in urban environment [4], and 4 in rural environment [30]. Noteworthy is that values around 1.8, below the free-space pathloss exponent, are often observed [17], [15], [30], [4], [32]. This indicates that a larger amount of energy is available due to multipath propagation in addition to the line of sight (LOS) component, leading to a smaller pathloss than for free-space propagation conditions.

Regarding the RMS delay spread, the shortest value is obtained in rural environments [15], [14], and the largest in urban environments [14], [19], [31]. Even though different measurement campaigns have reported more homogeneous results regarding the pathloss exponent, we see larger differences for the RMS delay spread results. Even fewer results have been covered in the literature with respect to the RMS Doppler spread [22], [15], [14]. They show again large discrepancies among them.

In Tab. 1.1 we list the extracted parameters from some recent vehicular radio channel measurement campaigns.

1.1.2 Vehicular Channel Models

Channel models are important in order to test different transmission techniques on computer simulations before deploying a new system. An accurate channel model

will deliver reliable results. Parameters extracted from measurement campaigns are used for feeding the channel models so that they create channel impulse responses (CIRs) for different environments. In this section, we will discuss different channel modeling approaches and their suitability for V2V channels.

A channel model is a mathematical representation of the CIR. The generated CIRs are used for system performance simulation purposes. In wireless communications for vehicular applications there are basically three channel modeling approaches in use:

Deterministic - Replay Model The CIRs collected in measurement campaigns can be used as a direct input for the channel in system simulations. The advantage of this method is their repeatability and accuracy, but only for very specific sites, namely the ones where the measurements were taken [22], [34].

Deterministic - Ray-Tracing
The CIRs are the result of solving the Maxwell equations for a specific site. However, it is not possible to solve them in practice, and an approximated solution can be obtained using the ray-tracing (RT) channel modeling approach. It is very important to correctly define the physical objects present in the environment to be simulated as well as their precise electromagnetic properties. The resulting CIRs are very accurate at the expense of a highly demanding computational process. The RT channel models are used in vehicular communications for investigation of antenna position on the vehicle or placement of access point [35], [36].

Stochastic - Tap-Delay Line Model
The main characteristic of the stochastic approach is to generate CIRs with specific statistical properties of the fading process, without assuming an underlying geometry. These properties are defined in the model through channel parameters, such as RMS delay and Doppler spreads, angle-of-departure (AOD) and angle-of-arrival (AOA), or power spectra and their distributions.

We can classify the stochastic channel models into two sub-groups depending on whether they are narrow- or wide-band. The narrow-band stochastic approach models the time-selectivity of the fading process by defining its Doppler spectrum [37]. The wide-band stochastic approach models also the frequency-selectivity of the fading process. The generated CIRs are time-frequency dependent.

The most used channel model of this kind is the tapped-delay line (TDL) model. The CIR consists of a finite number of delay taps, each one of them fades independently following a given Doppler spectrum. The TDL channel model is

based on the WSSUS assumption [1]. The complexity of such channel models is fairly low, but they do not always represent realistic properties for the V2V channel. Nevertheless, it has been adopted by the IEEE 802.11p standard [38] as reference channel model due to its flexibility and easy implementation [11], [25].

Geometry-Based Stochastic Channel Model (GSCM)
The GSCM is a combination of the two aforementioned approaches. The generation of the CIRs is done using simplified RT on scatterers stochastically placed in the physical environment to be simulated. Each one of the scatterers has associated fading properties chosen from parameters distributions obtained from measurement campaigns.

Within the GSCM approach we can distinguish two kind of models depending on where the scatterers are placed: *(i) ring-models*, and *(ii) physically-realistic models*. The *ring-models* place the scattering points around the TX and RX in a shape of a circle or ellipse [39], [40], [41], [42]. The *physically-realistic models* only place scattering points on physically realistic positions. For instance, in a vehicular GSCM the scatterers representing other vehicles are placed on a parallel position (lane) with respect to the TX and RX (also placed on a lane) [33], [41], [43], [44].

The GSCMs are accurate and represent the properties of the V2V channels well. The channel model generates CIRs for different environments by using the right parameter set, thus it is flexible. However, the computational complexity is relatively high, mostly for the *physically-realistic models*, where a large number of scatterers are needed to reproduce the contribution of diffuse components. Nevertheless, there exist methods for reducing the complexity of this calculation [5], [6]. Noteworthy is that these channel models inherently include the non-stationarities of the fading process, since they include the objects movement.

In the following, we are going to compare the methodologies presented previously. We discuss the most adequate channel model to be used for V2V system performance evaluation. We demand from a channel model that it generates *accurate* CIRs, which represent *realistic V2V properties*. The channel model should be *easy to implement and compute*. A *flexible* channel model will offer the system engineer more possibilities when testing algorithms for different situations. And finally, the channel model has to include this *non-stationarity* particular of V2V channels. Hence, a good vehicular channel model should be *accurate*, *realistic*, *low-complex*, and include *non-stationarities*.

In Tab. 1.2 we summarize the main properties of the channel modeling approaches previously presented, stressing their significance for V2V channels. We list the advantages for V2V of each approach with the sign "+" and the

Type	Technique	Characteristics
Deterministic	Replay model	+ Very good accuracy - Large amount of data has to be stored - Only valid for one specific site Used for network planning
	RT	+ Very good accuracy + Non-stationarities well represented - Very high computational complexity Used for determining antenna and acces point placement
Stochastic	TDL	+ Flexible: different environments are easy to parametrize + Relatively low computational complexity - It does not include the non-stationarities of the channel Used in simulations for system performance evaluation
GSCM		+ Good accuracy + Non-stationarities well represented + Flexible: different environments are easy to parametrize - Relatively high computational complexity (2) Used in simulations for system performance evaluation

Table 1.2: Summary of channel models approaches and their main characteristics. Desirable properties for vehicular communications are listed with "+", on the contrary, the drawbacks of each model are listed with "-". (2) A technique for reducing computational complexity in GSCM can be found in [5], [6]

drawbacks with "-". Based on them, we conclude that the GSCM approach is the most appropriate for modeling vehicular channels. The only negative aspect they present is the high complexity. However, as mentioned before, with using complexity reduction methods [5], [6] the GSCM becomes definitely the most suitable approach.

Clustering in Channel Modelling
The complexity of a GSCM is rather large. The clustering of MPCs with similar statistical properties might help to reduce it. The use of clustering for GSCM is well investigated [45], [46], [47], [48]. When deriving a cluster-based channel model, clusters need to be parametrized from measurements [49]. Most of the research in this direction has been put into defining the space localization of the clusters, in terms of AOD, AOA, power, and spread. There is a large number of publications studying the cluster parametrization for indoor scenarios [50], [48], or outdoor-to-indoor and indoor-to-outdoor [51], [52]. On the other hand, few results have been shown for outdoor mobile environments. The authors in [53] characterize and model the clusters for a V2I scenario at 2.5 GHz. V2I clustering results are also provided in [54] for an urban environment at 5.2 GHz.

1.1.3 The non-Stationarity

In the well studied cellular scenario, the statistical properties of the channel usually vary slowly with time. In these cases, the wide sense stationary uncorrelated scattering (WSSUS) assumption holds with good accuracy [1]. A process is wide sense stationary (WSS) when its statistical properties do not change with time, they are stationary in time. Similarly, the process is uncorrelated scattering (US) when its statistical properties do not change with frequency, they are stationary in frequency. This is commonly formulated as: *contributions with different Doppler frequencies are uncorrelated, and contributions at different delays are uncorrelated* [1]. However, due to the rapidly changing environment in vehicular communications the fading process describing the vehicular radio channels is non-stationary. The second order statistics can be approximated as constant for a finite region in time and frequency [55].

A number of papers has investigated the topic of non-stationarity in the past years, as the interest on vehicular communications has increased. A first definition of the stationarity time and stationarity bandwidth was proposed in [2], computed from the local scattering function (LSF) and the channel correlation function. It is a theoretical methodology derived for infinite time and frequency intervals, and it is difficult to apply to measurements.

In [56], the correlation between PDPs is used for assessing stationarity in urban environments. The authors introduce the use of a threshold for determining the length of the stationarity region. Based on this methodology, the correlation distance metric was proposed by [57] for characterizing stationarity in MIMO channels for the first time. Kattenbach in [58] establishes a framework for indoor non-stationary fading channels.

There is also an increasing number of experimental contributions that are describing the non-stationarity of the vehicular channel in time, i.e. the non-WSS behavior. The investigations in [59], [60], [61] measure the distance between locally defined power spectra of the fading process, and determines the range of validity of the WSS assumption. In [60], [61], the WSS assumption is characterized in terms of the stationarity distance. There, longer distances are observed in the presence of a strong LOS component and in convoy measurements. In [62], [63] statistical tests are defined based on the evolutionary spectrum of a signal estimated at different time instances, finding that the length of the WSS interval decreases with the number of antennas in a MIMO system, and that the number of WSS consecutive intervals is larger than the non-WSS consecutive intervals. A Rao test applied on time-varying auto-regressive model is proposed in [64] for testing WSS. However, the US assumption has been tested far less - to the best of our knowledge, never in V2V channels, and even for V2I channels only in a few cases (e.g., [65]).

1.2 Outline and own Contributions

This thesis consists of four chapters, as well as the introduction and the conclusions. The contents of this document are to a great extent also included in the following peer-reviewed publications:

[66] L. Bernadó, T. Zemen, A. Paier, G. Matz, J. Karedal, N. Czink, F. Tufvesson, M. Hagenauer, A. F. Molisch, and C. F. Mecklenbräuker, "Non-WSSUS vehicular channel characterization at 5.2 GHz - spectral divergence and time-variant coherence parameters," in *Assembly of the International Union of Radio Science (URSI)*, August 2008, pp. 9-15.

[67] L. Bernadó, T. Zemen, A. Paier, J. Karedal, and B. Fleury, "Parametrization of the local scattering function estimator for vehicular-to-vehicular channels," in *Vehicular Technology Conference Fall (VTC 2009-Fall), 2009 IEEE 70th*, September 2009, pp. 1-5.

[68] L. Bernadó, T. Zemen, J. Karedal, A. Paier, A. Thiel, O. Klemp, N. Czink, F. Tufvesson, A. Molisch, and C. Mecklenbräuker, "Multi-dimensional K-factor analysis for V2V radio channels in open sub-urban street crossings," in *Personal Indoor and Mobile Radio Communications (PIMRC), 2010 IEEE 21st International Symposium on*, September 2010, pp. 58-63.

[69] L. Bernadó, T. Zemen, A. Paier, and J. Karedal, "Complexity reduction for vehicular channel estimation using the filter-divergence measure," in *Asilomar Conference on Signals, Systems, and Computers*, November 2010, pp. 1-5.

[70] L. Bernadó, A. Roma, N. Czink, A. Paier, and T. Zemen, "Cluster-based scatterer identication and characterization in vehicular channels," in *Wireless Conference 2011 - Sustainable Wireless Technologies (European Wireless), 11th European*, April 2011, pp. 1-6.

[3] L. Bernadó, A. Roma, A. Paier, T. Zemen, N. Czink, J. Karedal, A. Thiel, F. Tufvesson, A. F. Molisch, and C. F. Mecklenbräuker, "In-tunnel vehicular radio channel characterization," in *Vehicular Technology Conference (VTC Spring), 2011 IEEE 73rd*, May 2011, pp. 1-5.

[71] L. Bernadó, T. Zemen, F. Tufvesson, A. Molisch, and C. Mecklenbräuker, "The (in-)validity of the WSSUS assumption in vehicular channels," in *Personal Indoor and Mobile Radio Communications (PIMRC), 2012 IEEE 23rd International Symposium on*, September 2012, *submitted*.

And the following book chapter:

[72] L. Bernadó, N. Czink, T. Zemen, A. Paier, C. F. Mecklenbräuker, and A. F. Molisch, *Vehicular Channels in the book: LTE Advanced and Beyond Wireless Networks: Channel Modeling and Propagation*, John Wiley & Sons Ltd., 2012, *to be published*.

The chapters are organized as follows:

Chapter 2: The DRIVEWAY'09 Measurement Campaign
The channel measurements used in this thesis are described in this chapter. The data used for analysis was collected in a vehicular radio channel measurement campaign named DRIVEWAY'09. A brief introduction to the sounding principle is given in the beginning of this chapter. Afterwards, we summarize the technical details regarding the measurements as well as the chosen scenarios and their main characteristics. Furthermore, we describe the particularities of sounding a rapidly time-varying radio channel. The measurement errors obtained for such channels are discussed and checked for the DRIVEWAY'09 data.

Chapter 3: Locally Defined Power Spectral Densities
In this chapter, we introduce the tools needed for characterizing non-stationary channels. First, a review on the stochastic radio channel characterization based on Bello's work [1] is given. The wide sense stationary and uncorrelated scattering assumptions, as well as the combined WSSUS assumption are revisited. The relationships between the deterministic and the stochastic description of the channel as in [1] are reformulated for the discrete case, since the whole thesis is based on the discrete representation of these functions. In addition, we provide an extension of the WSSUS relationships which allows a non-WSSUS characterization of the fading channel. By doing that, we set the basis of the stationarity assessment and characterization which is used for the rest of the document.

We reformulate the LSF multitaper-based estimator from [2], [55] in a discrete-time setting suitable for our measurements. The LSF estimator is used to calculate the scattering function of non-stationary processes. In order to parametrize the estimator, we define the MSE based on the structure of a two-dimensional (2D) Wiener filter. We show that the Wiener filter coefficients can be calculated from the LSF. We choose the parameters used for the estimation of the LSF based on the minimum MSE obtained at the output of the 2D Wiener filter with low computational complexity.

Once we have set the parameters to be used for estimating the LSF, we derive the time-varying and frequency-varying PDP and DSD from the LSF. We analyze the PDP and the DSD for three representative measurements and derive some general comments on them.

Chapter 4: The (in-)validity of the WSSUS Assumption in Vehicular Channels:
A non-WSSUS fading process can be split into so-called stationarity regions, where the WSS and the US properties hold approximately [1], [55]. In this chapter, we characterize the extend of the stationarity region of a non-WSSUS process. First, we assess the non-stationarity in terms of spectral distance. For that, we make use of two spectral distance metrics: the spectral divergence (SD), and the collinearity.

The SD is an unbounded distance metric between strictly positive definite power spectra. We apply it to neighboring LSFs for assessing stationarity. In order to qualitatively assess the extension of the stationarity in time and in frequency, we relate the SD metric to the MSE degradation using mismatched statistical knowledge for designing a 2D-Wiener filter. The mismatch results from using the filter coefficients calculated for a past stationarity region. The filter coefficients are derived from the LSF. Furthermore, we highlight the noise dependency of the SD metric.

Besides the SD, we use the collinearity for quantitatively assessing the stationarity. The collinearity is a modification of the correlation distance metric, introduced in [57] for characterizing stationarity. We extend the use of the collinearity for testing the WSS and the US assumptions on the vehicular radio channel. Since the collinearity is a bounded distance metric, it allows us to set a threshold for quantifying the extension of the stationarity region. Using the collinearity between LSFs, we characterize the stationarity of the vehicular fading process in time and in frequency.

Chapter 5: Time-Varying Stochastic Characterization of the Vehicular Channel:
Following the main conclusion derived from the previous chapter, we proceed here to fully stochastically characterize the data collected in the DRIVEWAY'09 vehicular measurement campaign. We investigate the first order moment of the fading process by means of its K-factor, the second order moment through the RMS delay and Doppler spreads, respectively. All sections in this chapter consist of the mathematical definition of the parameter to be characterized, a detailed analysis on an illustrative measurement, and modeling for the whole data ensemble.

The novelty in the analysis of the first order moment of the vehicular fading process lies on the introduction of its time-, frequency-, and space-dependency. We investigate the per-delay-bin narrow-band small-scale fading statistics, and characterize it by means of the K-factor. We first make a partition of the measurement bandwidth into sub-bands with 10 MHz each, according to IEEE 802.11p (standard for vehicular communications). Since the communication system for vehicular communications is orthogonal frequency division multiplexing (OFDM) based, we

also perform a second evaluation, which considers the whole bandwidth, and the narrow-band K-factor is calculated for each frequency bin.

The second order moment description of the fading channel is given by its RMS delay and Doppler spreads. In contrast to the previous published literature, the time-variability of these parameters is taken into account. In this thesis, the originality of the results does not only root from the uniqueness of the measured data, but also from the consideration of the time-varying characterization.

In the last section of this chapter, we move towards a geometry-based stochastic description of the time-varying power spectral density of the fading process in vehicular channels. We present an efficient method for detecting only the relevant MPCs, related to a physical scattering object, in the delay-Doppler spectral plane. By using a clustering algorithm we group the MPCs stemming from the same scatterer. We propose to use the MPC distance from [73] in the *density-based spatial clustering of applications with noise* algorithm [74]. Furthermore, we fully characterize the time-varying cluster parameters: number of clusters (scatterers), and cluster extension in the delay and Doppler domains.

1.3 Notation

Throughout the thesis, discrete variables are used most of the time, we are listing them together with their equivalent in the continuous domain in order to make the reading easier:

Variable name	Continuous domain	Discrete domain
time	t	m
frequency	f	q
delay	τ	n
Doppler shift	ν	p

2 The DRIVEWAY'09 Measurement Campaign

The investigation of the radio propagation properties relies on channel measurements that well represent real communication situations. Until now, the vehicular measurement campaigns were defined following the guidelines established for cellular systems. However, the low antenna position, the high velocities of TX and RX, and the large number of scattering objects make the propagation characteristics of the radio waves in vehicular channels very peculiar. Therefore, a redefinition of the measurement setting and scenarios is needed. The data used for evaluation in this thesis was collected in a measurement campaign called DRIVEWAY'09 (DiRectional hIgh-speed channel characterization for VEhicular Wireless Access sYstems). The DRIVEWAY'09 measurement campaign was carried out in 2009 in Lund, Sweden, and its vicinity. The main characteristics of the DRIVEWAY'09 measurement campaign are:

- directional MIMO measurements,
- use of realistic vehicular antennas and placement,
- use of passenger cars, and
- measurement scenarios defined based on safety-critical driving situations.

All these aspects are discussed in detail in this chapter.We also comment on some considerations to be taken into account when sounding the vehicular radio channel.

2.1 Measurement Equipment

The channel sounder used in DRIVEWAY'09 is the RUSK LUND channel sounder, from the company MEDAV [75]. This channel sounder uses the switched array principle [76]. Figure 2.1 shows the working principle for a 4×4 MIMO set up. The used transmit signal has a constant power spectral density throughout the measurement bandwidth B.

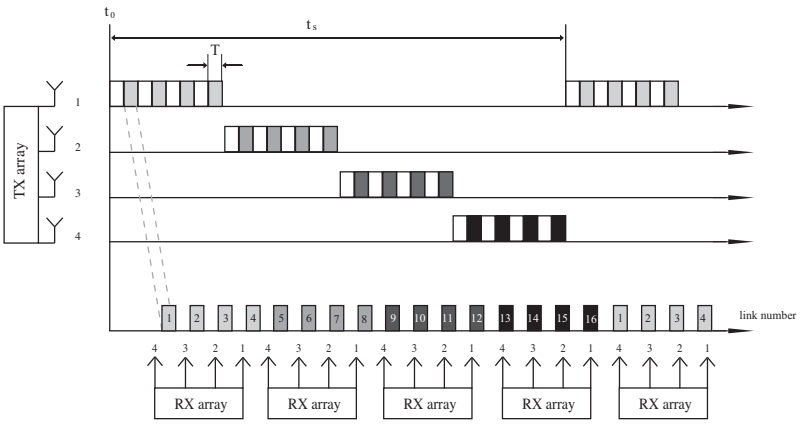

Figure 2.1: Switched array sounding principle.

The received signal is correlated in the frequency domain at the RX with the transmitted signal in order to obtain the channel frequency response, which is done for each antenna pair individually. Each antenna pair gives rise to a measured link. Table 2.1 lists the mapping of antenna pair to link number, also shown in Fig. 2.1.

Table 2.1: Links and corresponding TX -RX antenna pairs

Link	1	2	3	4	5	6	7	8	9	10	11	12	13	14	15	16
TX ant.	1	1	1	1	2	2	2	2	3	3	3	3	4	4	4	4
RX ant.	4	3	2	1	4	3	2	1	4	3	2	1	4	3	2	1

It is extremely important that the TX and the RX are perfectly synchronized, therefore, the RUSK LUND channel sounder is provided with a Rubidium clock at the TX and the RX side. In order to ensure this synchronization, the TX and the RX parts of the channel sounder were always synchronized over night the day before we conducted the measurements.

2.2 Particularities of the DRIVEWAY'09 Radio Channel Measurement Campaign

In DRIVEWAY09 our aim was to perform channel measurements considering the propagation conditions occurring in safety-related ITS applications. Therefore, we used passenger cars with vehicular antennas, and an scenario definition based on safety-related applications in ITS. In the following we will explain the particularities

of the DRIVEWAY'09 measurement campaign in detail.

2.2.1 The Vehicles and the Antennas

The size and shape of the vehicle carrying the measurement equipment influences the measured channel frequency responses. Therefore, in order to obtain results representing real propagation conditions, we used passenger cars. The channel sounder and the batteries needed for power supply were loaded in the trunk of the TX and the RX cars.

The output of the channel sounder after a high speed switch were connected to a four element uniform linear array mounted on the roof top of each car. The antenna elements were specially designed for this measurement campaign [77]. The array consists of four patch antennas separated a distance of $\lambda/2$. The four circular patches were tuned in order to make directional their radiation pattern. Each element was modified such that the main radiating directions were *front, back, right*, and *left* with respect to the driving direction. The array-combined antenna radiation pattern resembles an omnidirectional one.

The directionality of the patterns is achieved by setting the feeding point at an antenna edge, different for each element, and the addition of a parasitic element, which acts as a director, as depicted schematically in Fig. 2.2. The array and the parasitic elements were encapsulated into a conventional vehicular antenna module, with the particularity that it was mounted perpendicular to the driving direction in order to allow for directional analysis.

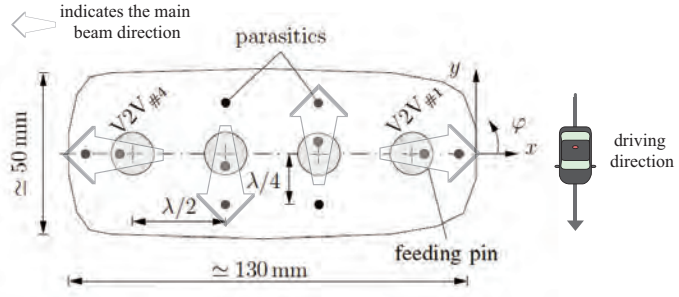

Figure 2.2: Four element uniform linear array antenna used for the DRIVEWAY'09 measurements.

The antennas were matched for a frequency range in accordance to the measurement frequency and bandwidth, and were designed such that the antenna gain remains on average within a variation of 10 dB for the whole bandwidth. More details

regarding the antennas can be found in [77].

2.2.2 Channel Sounding Parameters

A total of 16 links were measured at a carrier frequency of 5.6 GHz, which is the highest supported by the RUSK LUND channel sounder setup. Nevertheless, it is close enough to 5.9 GHz frequency band, meant for ITS communications in Europe. Propagation characteristics will not be significantly different at these two carrier frequencies.

We measured a total bandwidth of 240 MHz using a transmit power of 27 dBm. The snapshot repetition time was set to $t_s = 307.2\,\mu$s, with a sampling sequence length of $T = 3.2\,\mu$s. Due to the storage limitatios of the channel sounder, measurement runs of 10 to 20 seconds were recorded. With these parameter settings we achieved a maximum resolvable Doppler shift of 1.6 kHz, and delay 4.17 ns. Table 2.2 summarizes the main DRIVEWAY'09 sounding parameters.

Table 2.2: DRIVEWAY'09 measurement campaign parameter details

Parameters	Measurement
Channels:	4×4 MIMO
Carrier frequency:	5.6 GHz
Measurement bandwidth:	240 MHz
Transmit power:	27 dBm
Sampling sequence length:	$3.2\,\mu$s
Snapshot repetition time:	$307.2\,\mu$s
Recording time:	$10 - 20$ s

2.2.3 Measured Scenarios

Previous vehicular radio channel measurement campaigns focused on the scenario description taken from the well studied GSM cellular systems [45]. They include slight adaptations, such as consideration of vehicle speed, and driving direction. However, a new scenario definition is needed, based on safety-related ITS applications [18].

In the following we present this new scenario definition with their particularities as well as their possible applications:

- *Road crossing*: This scenario consists of a conventional road crossing in rural, suburban, and urban environments, where both vehicles approach the crossing from perpendicular directions, Fig. 2.3. Within this category we define

four sub-scenarios so that we can measure crossings under various configurations: (a) *suburban with traffic*, (b) *suburban without traffic*, (c) *urban single lane*, and (d) *urban multiple lane*. Possible safety-related applications for this scenario are emergency vehicle warning, intersection collision warning, or pre-crash sensing warning.

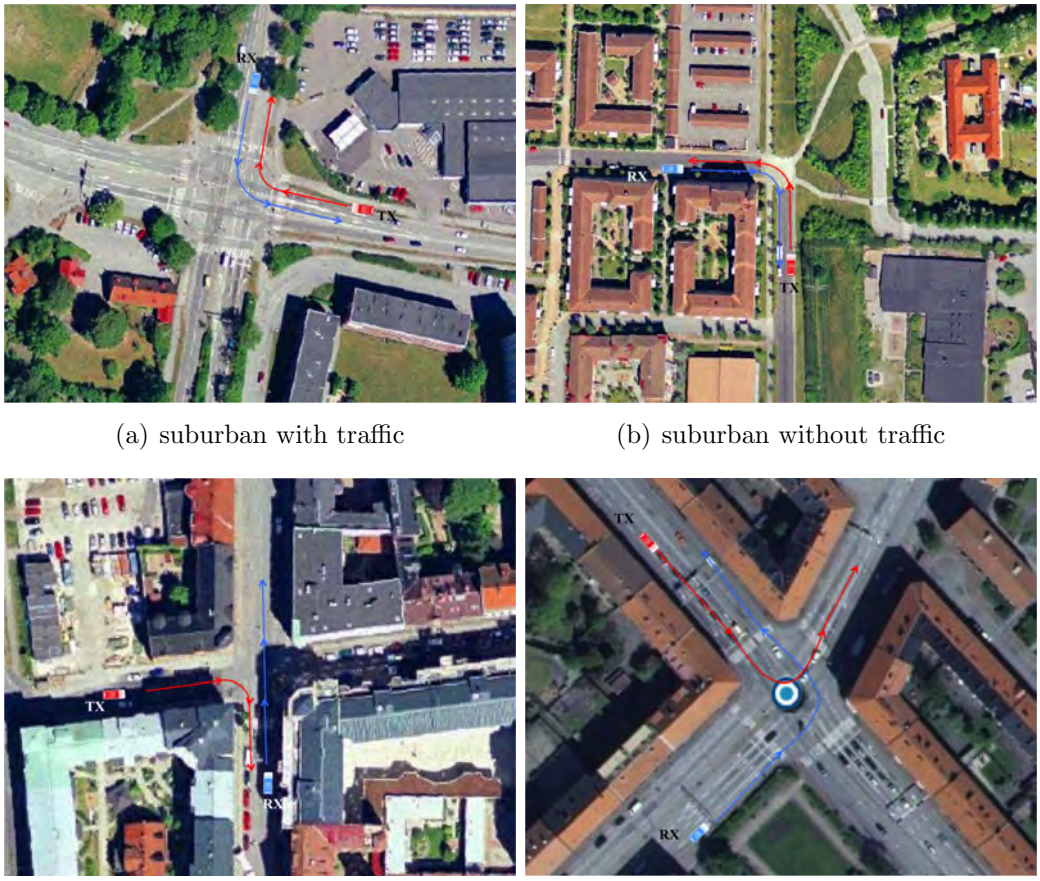

(a) suburban with traffic

(b) suburban without traffic

(c) urban single lane

(d) urban multiple lane

Figure 2.3: Measurement locations for the road crossing scenario.

- *General LOS obstruction - highway*: This scenario investigates the influence of LOS obstruction in highway environments. TX and RX are driving in the same direction on the highway. There are other big trucks which are intermittently obstructing the LOS between TX and RX , Fig. 5.2. Vehicular communications might help in this situation for hazardous location notification.
- *Merging lanes - rural*: Here we consider a special case of intersections, a ramp intersecting a main road with partly obstructed junction. V2V communications

Figure 2.4: Measurement location for the general LOS obstruction on the highway scenario.

occur between cars driving in the same direction at high speeds, Fig. 2.5. Possible application one can easily imagine are cooperative merging assistance, and wrong way driving warning.

Figure 2.5: Measurement location for the merging lanes scenario.

- *Traffic congestion*: Different situations in a traffic congestion are considered here: Slow traffic, where both TX and RX car are stuck in a traffic jam. They move in the same direction with slow velocities, and are surrounded by other vehicles moving with similar speed, Fig. 2.6 (a). We also consider the case of approaching a traffic jam, where one of the cars is stuck in a traffic jam while the other one approaches from behind, Fig. 2.6 (b). Vehicular communications might help here to reduce rear end collisions.

(a) slow traffic (b) approaching traffic jam

Figure 2.6: Measurement locations for the traffic congestion scenario.

- *In-tunnel*: Two cars drive in the same direction at more or less similar velocities inside a tunnel. The tunnel allocates only one driving direction with two lanes, Fig. 2.7. Overtaking in tunnel or hazardous notification could benefit from radio communication in this environment.

Figure 2.7: Measurement location for the in-tunnel scenario.

- *On-bridge*: Two cars drive in the same direction over a bridge with a separation of about 150 m, Fig. 2.8. The bridge is composed by big metallic structures, equidistantly spaced. The specific bridge where measurements were performed is held over the sea.

We have carried out from 5 to 15 measurement runs per scenario in order to enable meaningful statistical analysis.

Figure 2.8: Measurement location for the on-bridge scenario.

2.3 Abbreviations used for the Measurements

The names we used for the scenario description are rather long. Their use in a sentence might difficult conveying its main message. Therefore, we use a short version of the scenario naming during the remaining of the thesis as:

- road crossing - suburban with traffic (RC-swt)
- road crossing - suburban without traffic (RC-swot)
- RC-usl
- road crossing - urban multiple lane (RC-uml)
- GLO-h
- merging lanes - rural (ML-r)
- traffic congestion - slow traffic (TC-st)
- traffic congestion - approaching traffic jam (TC-atj)
- in-tunnel (IT)
- on-bridge (OB).

An schematic representation of the described measurements is depicted in Fig. 2.9 using the introduced abbreviations.

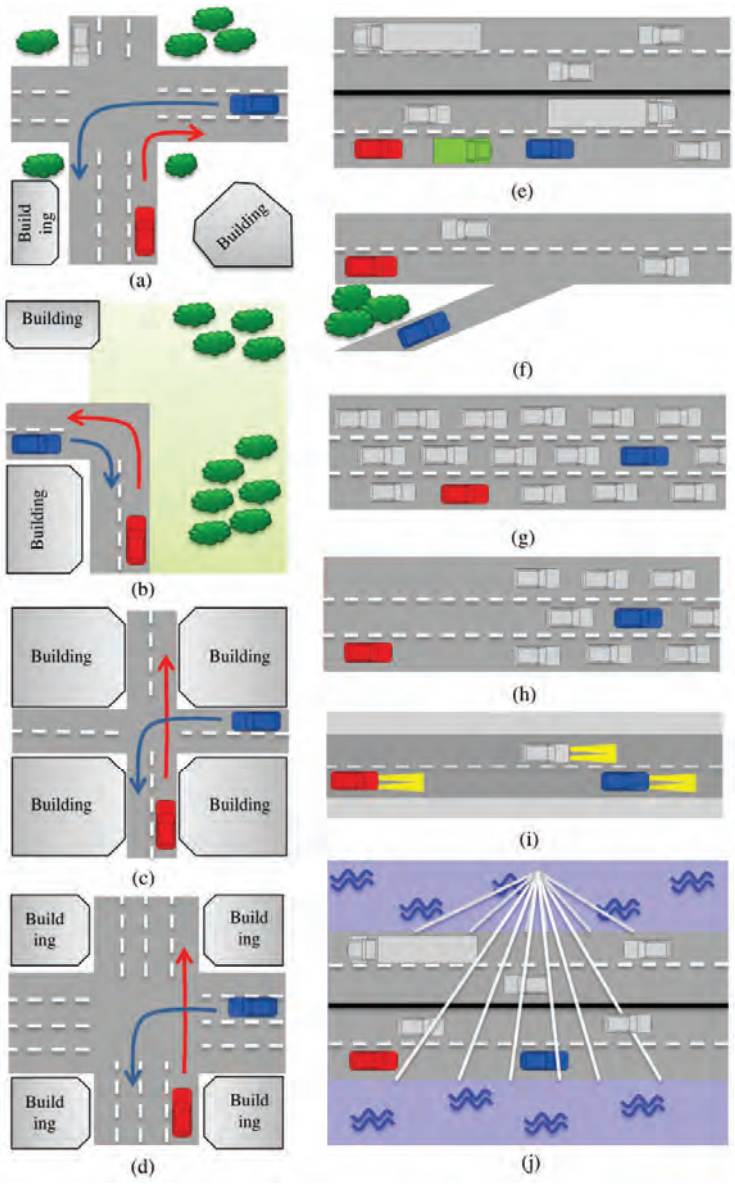

Figure 2.9: DRIVEWAY'09 scenarios: (a) *road crossing - suburban with traffic*, (b) *road crossing - suburban without traffic*, (c) *road crossing - urban single lane*, (d) *road crossing - urban multiple lane*, (e) *general LOS obstruction - highway*, (f) *merging lanes - rural*, (g) *traffic congestion - slow traffic*, (h) *traffic congestion - approaching traffic jam*, (i) *in-tunnel*, (j) *on-bridge*.

2.4 Vehicular Channel Sounding

The vehicular channel is time-varying and frequency selective. In order to properly collect these channel properties, a wideband channel sounder system has to be used for sounding the channel [78].

2.4.1 Channel Sounding

Some important issues concerning the sounding of wideband rapidly time-varying channels have to be considered when sounding the vehicular radio channel. Otherwise, they might lead to measurement errors and therefore to wrongly recorded channel frequency responses [79]. In the channel sounding process, we are actually measuring the concatenation of the TX bandpass filter G_{TX} (which determines the measuring bandwidth B), the time-varying channel frequency response $\tilde{H}$ (which is not necessarily band-limited), and the RX bandpass filter G_{RX} (which uses the same bandwidth as the TX filter). We denote this chain as

$$H(t,f) = G_{\mathrm{TX}}(f)\tilde{H}(t,f)G_{\mathrm{RX}}(f). \tag{2.1}$$

Before the sounding signal goes through the TX filter, it is multiplied and up-converted to the desired carrier frequency f_c. At the end of the chain, after the RX filter, a demodulator shifts it back to the baseband. For simplicity, we will consider here the baseband representation of the measured frequency response as in Eq. (2.1). Note that the channel frequency response $H(t,f)$ and the channel impulse response $h(t,\tau)$ are equivalent and are related by a one dimensional Fourier transformation [1] as:

$$H(t,f) = \int_{-\infty}^{\infty} h(t,\tau)\mathrm{e}^{-2j\pi\tau f}d\tau. \tag{2.2}$$

Equation (2.1) in the delay domain reads $h(t,\tau) = g_{\mathrm{TX}}(\tau) * \tilde{h}(t,\tau) * g_{\mathrm{RX}}(\tau)$, where $*$ stands for convolution. The convolution applies on the τ variable as

$$H(t,f) = \int_{-\infty}^{\infty}\int_{-\infty}^{\infty} g_{\mathrm{TX}}(\tau)\tilde{h}(t,\tau-\tau')g_{\mathrm{RX}}(\tau-\tau'-\tau'')d\tau' d\tau''. \tag{2.3}$$

2.4.2 Fundamental Channel Sounding Errors

For the DRIVEWAY'09 measurement campaign we used a correlative channel sounder. Nevertheless, this type of channel sounding technique is based on the fact that the channel $\tilde{H}$ and the RX filter commute, whereas this cannot be applied for rapidly time-varying channels. Moreover, several measurements of the channel

(snapshots) have to be performed in order to track the fluctuations of the channel. These two main points give rise to four types of systematic measurement errors [79].

In order to minimize the effect of these errors, the sounding parameters have to be chosen accurately. In the following we list the errors described in [79] and corroborate the negligible measurement error in the DRIVEWAY'09 measurements:

1. The *commutation error* arises from the assumption that the RX filter and the channel $\tilde{H}$ commute. The error is 0 for time-invariant channels.

2. Ideally, the convolution of the TX and RX filter results in the dirac function, i.e. $g_{TX}(t) * g_{RX}(t) = \delta(t)$. However, this is not the case in practice, which creates the *pulse-compression error*. Back-to-back calibration intends to reduce this error.

   The mitigation of these two errors (commutation and pulse-compression errors) can be achieved by properly selecting the filter length (or sounding sequence length) T based on [79]

   $$T = \frac{2^{l_{\text{opt}}} - 1}{B} \qquad \text{with} \qquad l_{\text{opt}} = \text{round}\left\{\log_2\left(\sqrt{\frac{4B}{\pi\bar{\nu}}} + 1\right)\right\}, \tag{2.4}$$

   where $\bar{\nu}$ is the mean Doppler shift. The term $2^{l_{\text{opt}}} - 1$ is needed for practical implementation. Since in practice, we do not know this value a priori, we calculate Eq. (2.4) using an assumed maximum Doppler shift $\nu_{\max}$, and obtain a $T_{\min}$ for the sounding sequence length.

3. The maximum delay of the channel $\tau_{\max}$ and the maximum Doppler shift of the channel $\nu_{\max}$ determine the *aliasing error*. Nevertheless, the error is 0 for channels such that

   $$\tau_{\max} \leq T \leq \frac{1}{2\nu_{\max}K}, \tag{2.5}$$

   where $K = T/t_s$ is the repetition period of the measurement and t_s is the sampling rate. The condition (2.5) requires that $2\tau_{\max}\nu_{\max} \ll 1$, which defines a channel as *doubly underspread* [55]. A doubly underspread channel is characterized by having its spreading function within a compact support region delimited by $\tau_{\max}$ in delay, and $\nu_{\max}$ in Doppler, otherwise it is 0 [55].

4. Finally, the *misinterpretation error* results from the fact that what the channel sounder actually estimates is the output delay spread function $h^{\text{O}}(t,\tau)$ instead of the CIR $h(t,\tau)$, also called input delay spread function [1]. The channel is a

linear, time-varying system, which relates its input $x(t)$ with the output $y(t)$ through a kernel function κ_H as

$$y(t) = \int_{-\infty}^{\infty} \kappa_H(t, t')x(t')dt'. \tag{2.6}$$

The input and the output delay spread functions represent the same channel seen from the input or seen from the output of the system. When performing channel sounding, we measure the channel at the output (RX), i.e. the response of the channel is at time $t + \tau$, and not at $t - \tau$, which would be the response of the channel seen at the input (TX).

The input delay spread function is given by setting the kernel function $\kappa_H(t, t-\tau)$, whereas the output spread function is obtained by setting $\kappa_H(t + \tau, t)$ as in [1]. These two functions are related as follows

$$h(t, \tau) = h^{\mathrm{O}}(t - \tau, \tau), \tag{2.7}$$

which makes the error correction rather easy by just properly interpreting $h(t, \tau)$.

2.4.3 Validation of the DRIVEWAY'09 Sounding Parameters

In the DRIVEWAY'09 measurement campaign we recorded the sampled version of the time-varying frequency response for each individual link $l \in \{1, \ldots, L\}$ as

$$H_l[m, q] := H_l(t_{\mathrm{s}}m, f_{\mathrm{s}}q), \tag{2.8}$$

where $m \in \{0, \ldots, S-1\}$ represents time sampled at a rate $1/t_{\mathrm{s}}$, with S being the total number of recorded snapshots, and $q \in \{0, \ldots, Q-1\}$ denotes frequency, with Q being the number of measured frequency bins. The measurement bandwidth is denoted by B and defines a frequency resolution of $f_{\mathrm{s}} = B/Q$.

These parameters were chosen for the DRIVEWAY'09 measurements as $Q = 769$ frequency bins in $B = 240$ MHz total measured bandwidth, collected over $L = 16$ links. Further details on the measurement campaign are described in te beginning of this chapter.

In what follows, we are going to analyze the four systematic measurement errors described previously for the DRIVEWAY'09 data.

We used a $T = 3.2\,\mu$s sounding sequence, which satisfies $T \leq T_{\min} = 2.1\,\mu$s calculated from Eq. (2.4) with considering a maximum Doppler shift of $\nu_{\max} = 2\,$kHz. In this way, we assure to palliate the *commutation* and *pulse-compression errors*.

Considering that we have a 4×4 system, the resulting sampling time $t_s = KT = 2 \times 4 \times 4 \times 3.2\,\mu\text{s} = 102.4\,\mu\text{s}$, with $K = 32$. The factor 2 results from the guard interval between snapshots in the channel sounder. However, due to storage constraints in the channel sounder, with this parameter setting only channel frequency responses of 3.3 s length can be stored generating a 1 GB file.

Nevertheless, we are interested in longer measurement periods, but at the same time we would like to be able to resolve large maximum Doppler shifts. This is why we decided to increase K from 32 to 96 and therefore the snapshot repetition time $t_\text{s} = 307.2\mu\,\text{s}$. With that, we can resolve Doppler shifts up to $\nu = 1/2t_\text{s} = 1.63\,\text{kHz}$, which corresponds to a relative velocity between TX and RX of 314 km/h (87.19 m/s) at a carrier frequency $f_c = 5.6\,\text{GHz}$. We consider this relative speed to be reasonable for vehicular communications.

By setting $t_s = 302.7\,\mu\text{s}$ we take the risk of suffering from *aliasing error*. For that purpose we first confirm the doubly underspread property of the channel ($2\tau_\text{max}\nu_\text{max} \ll 1$) with $\tau_\text{max} = T = 3.2\,\mu\text{s}$ and $\nu_\text{max} = 1.63\,\text{kHz}$ resulting in $5.2 \cdot 10^{-3} \ll 1$. With that, the fulfillment of the condition (2.5) is achieved with equality, and therefore we can consider the *aliasing error* to be zero in our measurements.

In the next chapter, we derive a framework for channel characterization based on the sampled frequency response $H[m, q]$, or its equivalent CIR, $h[m, n]$, therefore from now and for the remaining of the document we will use the discrete variables as introduced in Chap. 1, i.e. m for the discrete time index, q for the discrete frequency index, n for the discrete delay index, and p for the discrete Doppler index. Further discrete variables will be introduced when needed.

3 Locally Defined Power Spectral Densities

In vehicular communications, the environment changes rapidly due to the high mobility of the RX, the TX, and scatterers. Furthermore, the antennas are placed on the roof top of the cars, which enlarges the multipah propagation effects. These two effects determine a time-varying frequency-selective CIR. It is of special interest to characterize the dispersion of the signal through the channel in the delay domain, due to multipath propagation, and in the Doppler domain, due to mobility.

Due to the fast changing propagation conditions, which are a key feature of vehicular communications, the statistical characterization of this dispersion is valid only for a finite region in time and frequency.

In this chapter we present some analytical tools that allow to properly characterize the fading process in vehicular channels.

3.1 Non-WSSUS: a Time-Frequency Dependent WSSUS Extension

A doubly underspread non-WSSUS channel [55] can be seen as an extension of the WSSUS case in the way that the dependency on time and frequency is added to the stochastic analysis. In other words, it is a time-frequency dependent extension of Bello's work [1]. This is represented in Fig. 3.1, where this extension is highlighted in bold face.

3.1.1 The WSS and the US Assumptions

First we review the concepts of the wide sense stationary (WSS) and the uncorrelated scattering (US).

Wide Sense Stationarity (WSS)
A process is considered to be wide sense stationary WSS when its first and second

order statistical moments are independent of absolute time. Since wireless radio channels are random, the mean is usually assumed to be zero, and we only consider its second order moment, i.e. the time auto-correlation function. Then, the fading process is WSS when the time auto-correlation function does not depend on m and m', but on its difference $\Delta m = m - m'$ as

$$R_{\mathrm{H}}[m, m'; q, q'] = R_{\mathrm{H}}[\Delta m; q, q'], \tag{3.1}$$

where R_{H} is the time-frequency channel correlation function. The delay cross spectral density, the Doppler cross spectral density, and the scattering function can be obtained by performing the corresponding Fourier transformations as indicated in Fig. 3.1. The WSS condition can be rephrased as: *contributions with different Doppler shifts are uncorrelated.*

Uncorrelated Scattering (US)
The US assumption is the parallel version of the WSS assumption in the frequency domain, i.e. the second order statistical description of the channel remains independent of the absolute frequency, and in terms of the time-frequency correlation function reads

$$R_{\mathrm{H}}[m, m'; q, q'] = R_{\mathrm{H}}[m, m'; \Delta q], \tag{3.2}$$

where $\Delta q = q - q'$. Here again, the rest of the functions can be obtained by Fourier transforming the time-frequency channel correlation function as indicated in Fig. 3.1. The US condition is also often rephrased in the dual domain as: *contributions at different delays are not correlated.*

Wide Sense Stationary Uncorrelated Scattering (WSSUS)
The channel happens to be WSSUS when both aforementioned assumptions hold, i.e. when the statistics of the fading process do not change neither in time nor in frequency

$$R_{\mathrm{H}}[m, m'; q, q'] = R_{\mathrm{H}}[\Delta m; \Delta q]. \tag{3.3}$$

This results in a huge simplification of the statistical representation of the wireless channel, since the functions depend on only two variables instead of four.

Non-Wide Sense Stationary Uncorrelated Scattering (non-WSSUS)
Nevertheless, in vehicular channels the environment changes very rapidly and the WSS and US assumptions can not be guaranteed to be fulfilled for infinite time and bandwidth. Methods have been proposed to deal with non-WSSUS processes by repeating the experiment and performing the second-order statistics calculation

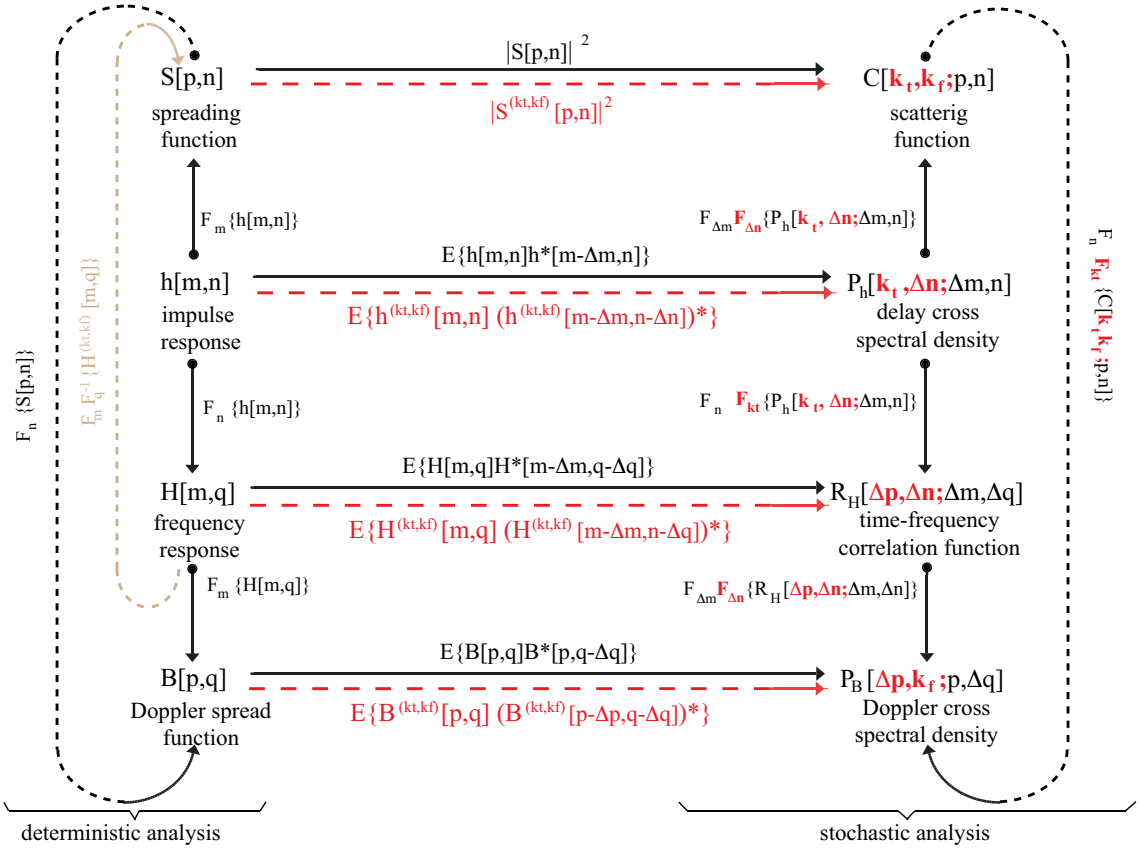

Figure 3.1: Interrelationships between channel functions on the left hand side, and between channel correlation functions on the right hand side as in [1]. In red bold-face we denote the addition of time-frequency dependence in the stochastic analysis. This is required for describing non-WSSUS processes. In brown bold-face we denote the path followed for calculating the locally defined scattering function as described in [2].

with the obtained samples [80]. In reality it is very difficult to obtain different realizations of the same experiment while keeping the same experimental conditions. Therefore, we assume the fading process to be ergodic and split its observations in small regions, within which we can assume that the WSSUS property holds [55]. By doing so, we make possible the stochastic analysis of the fading process, and dependent on the time and the frequency, as represented in Fig. 3.1.

3.2 Locally Defined Power Spectrum by means of the local scattering function (LSF)

When describing a fading process, it is unfeasible to do it deterministically. Therefore, it is meaningful to describe its statistical moments. We first assume that the first order moment is zero, afterwards, in Chap. 5 we will investigate the first order description of the fading process by means of its K-factor. A representation of the second order moment is done through the auto-correlation function, or through its two dimensional Fourier transform, which defines the power spectrum of the fading process (see Fig. 3.1).

We assume a-priori that the fading process is non-WSSUS. We can define a time-frequency region, where we assume that the WSSUS properties locally hold. We call this WSSUS time-frequency region *minimum stationarity region*, and define its size with M samples in time and N samples in frequency.

The delay and Doppler shift resolution of the resulting power spectra is given by $\tau_\mathrm{s} = 1/(Nf_s)$ and $\nu_\mathrm{s} = 1/(Mt_s)$, respectively. One should be careful in defining the length of M and N, taking into account the trade-off between resolution and the probability of violating the local stationarity assumption.

3.2.1 The LSF Estimator

When estimating the power spectrum of a process using measurements, it is very difficult to obtain statistically independent realizations of the same process. By tapering the measurement data using orthogonal windows, and by estimating the spectrum of each individual resulting windowed data set, we obtain multiple independent spectral estimates from the same sample. The total estimated power spectrum is then calculated by averaging over all tapered spectra. Through this averaging, the resulting estimate presents low variance. Nevertheless, by using multiple windows on the data, the bias of the estimator increases. Therefore, the number of tapers used is a key parameter determining the performance of the estimator.

We apply the multitaper spectral estimation technique [81] [82] for estimating the LSF using a sliding window on the recorded time-varying frequency response $H[m, q]$. For that, we use the discrete version of the LSF multitaper based estimator, introduced in [2] for the continuous-time case.

As mentioned before, we assume that the fading process is locally stationary within the stationarity region with dimension $M \times N$, in time and frequency, respectively. Then, we calculate the LSF for consecutive stationarity regions. The time and the frequency index of each stationarity region is $k_t \in \{1, \ldots, \lfloor \frac{S-M}{\Delta_t} \rfloor\}$,

and $k_f \in \{1, \ldots, \lfloor \frac{Q-N}{\Delta_f} \rfloor\}$, respectively and correspond to its center. The relative time index within each stationarity region is denoted by the variable $m' \in \{-M/2, \ldots, M/2-1\}$, and the relative frequency index by $q' \in \{-N/2, \ldots, N/2-1\}$. The relationship between the relative and absolute time index is given by $m = [(k_t - 1)\Delta_t + m'] + M$, where Δ_t denotes the time shift between consecutive stationarity regions. In the frequency domain the relationship is $q = [(k_f - 1)\Delta_f + q'] + N$, where Δ_f denotes the frequency shift.

We compute an estimate of the discrete LSF [55], [59] as

$$\hat{\mathcal{C}}[k_t, k_f; n, p] = \frac{1}{IJ} \sum_{w=0}^{IJ-1} \left| \mathcal{H}^{(\boldsymbol{G}_w)}[k_t, k_f; n, p] \right|^2 \tag{3.4}$$

where $n \in \{0, \ldots, N-1\}$ denotes the delay index, and $p \in \{-M/2, \ldots M/2-1\}$ the Doppler index, respectively. The LSF at k_t, k_f corresponds to the center value of the time-frequency stationarity region. The windowed frequency response reads

$$\mathcal{H}^{(G_w)}[k_t, k_f; n, p] = \sum_{m'=-M/2}^{M/2-1} \sum_{q'=-N/2}^{N/2-1} H[m' - k_t, q' - k_f] G_w[m', q'] \mathrm{e}^{-\mathrm{i}2\pi(pm' - nq')}. \tag{3.5}$$

The window functions $G_w[m', q']$ shall be well localized within the support region $[-M/2, M/2-1] \times [-N/2, N/2-1]$.

We apply the discrete time equivalent of the separable frequency response used in [55], $G_w[m', q'] = u_i[m'+M/2]\tilde{u}_j[q'+N/2]$ where $w = iJ+j$, $i \in \{0, \ldots, I-1\}$, and $j \in \{0, \ldots, J-1\}$. The sequences $u_i[m']$ are chosen as the discrete prolate spheroidal sequences (DPSS) [83] with concentration in the interval $\mathcal{I}_M = \{0, \ldots, M-1\}$ and bandlimited to $[-I/M, I/M]$. The DPSS are the solutions to the Toeplitz matrix eigenvalue equation [83], [82]

$$\sum_{\ell=0}^{M-1} \frac{\sin(2\pi \frac{I}{M}(\ell - m'))}{\pi(\ell - m')} u_i[\ell] = \lambda_i u_i[m'] \,. \tag{3.6}$$

The sequences $u_j[q']$ are defined similarly with concentration in the interval $\mathcal{I}_N = \{0, \ldots, N-1\}$ and bandlimited to $[-J/N, J/N]$ as

$$\sum_{\ell=0}^{N-1} \frac{\sin(2\pi \frac{J}{N}(\ell - q'))}{\pi(\ell - q')} u_j[\ell] = \lambda_j u_j[q'] \,. \tag{3.7}$$

The DPSSs are orthonormal on $[0, M-1]$ in the time domain, and orthonormal on $[0, N-1]$ in the frequency domain. The eigenvalues λ_i determine the order of the

sequences as $1 > \lambda_0 > \lambda_1 > \ldots > \lambda_{M-1} > 0$ in time. The order of the sequences in frequency is defined by the eigenvalues in frequency in the same way.

The eigenvalues λ_i and λ_j, and the sequences u_i and u_j are a function of the time-bandwidth product defined by $2\mathcal{N}_\mathrm{t}\mathcal{W}_\mathrm{t} = M(I/M)$ in time, where $\mathcal{N}_\mathrm{t} = M$ is the length in time of the minimum stationarity region, and $2\mathcal{W}_\mathrm{t} = (I/M)$ is the resolution in the Doppler domain. The time-bandwidth product in frequency is defined as $2\mathcal{N}_\mathrm{f}\mathcal{W}_\mathrm{f} = N(J/N)$, with $\mathcal{N}_\mathrm{f} = N$ being the length in frequency of the minimum stationarity region, and $2\mathcal{W}_\mathrm{f} = (J/N)$ is the resolution in the delay domain. The first $2\mathcal{N}\mathcal{W}$ eigenvalues are considerably close to 1, and their respective sequences have the greatest fractional energy concentration in $(-\mathcal{W}, \mathcal{W})$. Afterwards, the eigenvalues decay rapidly to 0, this is why we only need to consider $I \leq 2\mathcal{N}_\mathrm{t}\mathcal{W}_\mathrm{t}$ and $J \leq 2\mathcal{N}_\mathrm{f}\mathcal{W}_\mathrm{f}$.

The number of tapers (I, J) used for the LSF estimation controls the bias-variance trade-off and it is going to be investigated in a later section within this chapter. In Fig. 3.2 we can observe the LSF estimated at different stationarity regions.

Another important parameter is the size of the stationarity region in time and frequency. Its extend in time determines whether the WSS assumption holds, and its extend in frequency determines whether the US assumption holds.

If we set $Mt_\mathrm{s} < T_\mathrm{stat}$ stationarity time (time span where the process is WSS), the LSF is calculated within a region for which the WSS assumption is fulfilled. Similarly in the frequency domain by setting $Nf_\mathrm{s} < F_\mathrm{stat}$ stationarity bandwidth (frequency bandwidth where the process is US), we ensure the US assumption to hold. This topic is going to be investigated in the next chapter, and the concepts of stationarity time and stationarity bandwidth will be introduced.

3.2.2 The Physical Interpretation of the LSF

Even though the LSF is not necessarily real-valued and positive, it can be interpreted as the generalized spreading function [84] for a stationarity region, under the assumption of doubly-underspread channels ($2\tau_\mathrm{max}\nu_\mathrm{max} \ll 1$). It is composed of several spectral peaks at different positions in the delay-Doppler plane. These peaks correspond to a physical object (scatterer) which originates MPCs with different power and delay-Doppler coordinates. The first peak is generally the strongest one corresponding to the LOS path from TX to RX (in obstruction free scenario).

Later peaks relate to other scatterers, such as other cars or trucks, driving beside the TX-RX link, or traffic signs and big metallic structures. Generally, peaks with negative Doppler indicate objects moving away from the TX-RX pair, whereas a positive Doppler shift indicates approaching objects. We understand approaching/leaving with respect to the TX-RX link, i.e. an object can be static but due to

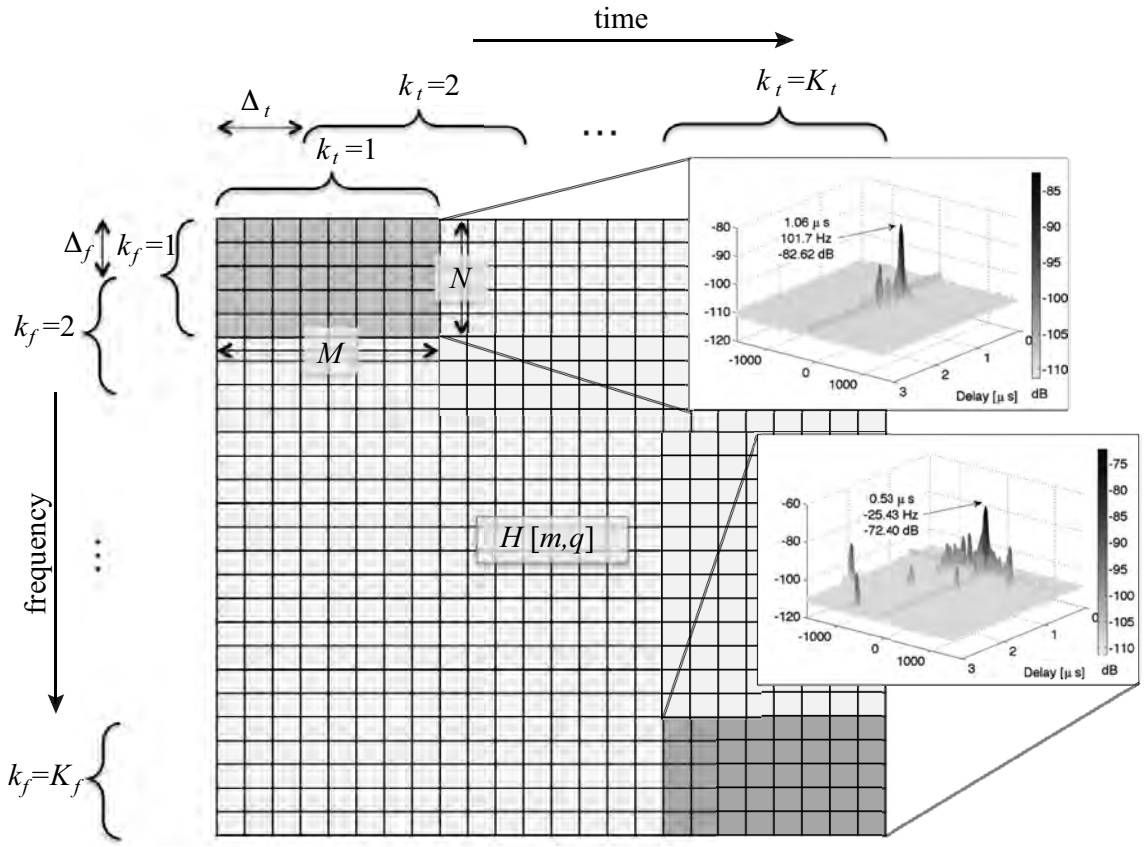

Figure 3.2: Schematic representation of the time-frequency sliding stationarity region window used for the LSF estimation. The sampling time of the data used for this figure is $t_\mathrm{s} = 307.2\,\mu$s. The total bandwidth of $B = 240\,$Hz consists of 769 frequency bins. The stationarity region dimensions are chosen to be $M = 128$ samples in time and $N = 256$ samples in frequency. For simplicity, in the figure $K_t = \lfloor \frac{S-M}{\Delta_t} \rfloor$ and $K_f = \lfloor \frac{Q-N}{\Delta_f} \rfloor$.

the TX and RX movement, it appears as approaching. The delay component of the peaks indicates the distance at which the scatterers are placed.

Furthermore, the peaks move in the delay-Doppler plane with time and frequency, which corroborates the high time-variability of the channel and the violation of the WSSUS assumption.

Note the position of the first peak in the two LSFs plotted in Fig. 3.2. The two LSFs correspond to two different stationarity regions for a highway opposite directions measurement. The peak in the first plot presents a Doppler shift of 101.7 Hz and delay of 1.06 μs. The TX and the RX are approaching each other with a relative speed [1] of 19.6 km/h (5.45 m/s) and they are separated 480 m. Note that at this point we only have few scattering components represented by the peaks beside the LOS peak. On the lower LSF figure, the peak of the LOS has coordinates -25.43 Hz and 0.53 μs. The negative Doppler shift tells us that the TX and RX are leaving with a relative speed of 4.9 km/h (1.36 m/s), and from the delay we know that the distance between them is 159 m. In this second LSF plot, there are more spectral peaks indicating a richer scattering environment. Note that the strength of the LOS peak also changes over time and frequency.

3.2.3 The local scattering function Parametrization

We have presented the LSF estimator as a tool for treating non-WSSUS processes. Nevertheless, we have also seen that there are many parameters involved in its calculation, such as the number of tapers to be used in the time and the frequency domain I and J, as well as the extent of the *minimum stationarity region*, defined by M and N. In this section we compute the optimal parametrization of the multitaper-based LSF estimator in terms of the number of tapers I and J. The choice of M and N will be investigated in the next chapter.

In Fig. 3.3 we show the outcome of the LSF estimator applied to a measured channel on the highway with intermittent LOS obstruction between cars driving in the same direction. For calculating these estimates, we select $M = 128$ and $N = 512$ samples in the time and in the frequency domain respectively.

Subfigure (a) displays the estimated LSF using only $I = 1$ window in time and $J = 1$ window in frequency. Strong peaks can be distinguished, but weak peaks

[1] We obtain an approximate relative speed v_{rel} directly from the Doppler shift component if the distance between TX and RX is larger than the maximum road width, which we consider to be at most 20 m. In that case, the angle Θ_{TX-RX} between the speed vectors of both vehicles is small enough so that $\cos(\Theta_{TX-RX}) \approx 1$, and therefore $v_{\text{rel}} = \nu c/f$, where ν is the Doppler shift, c the speed of light, and f the carrier frequency.

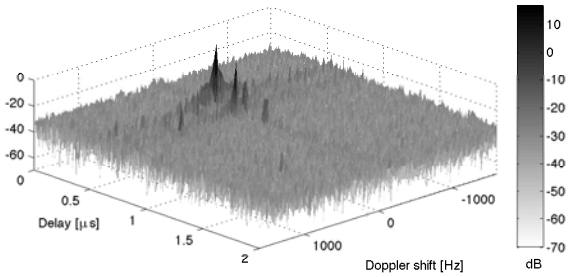

(a) LSF estimated with I=1 and J=1.

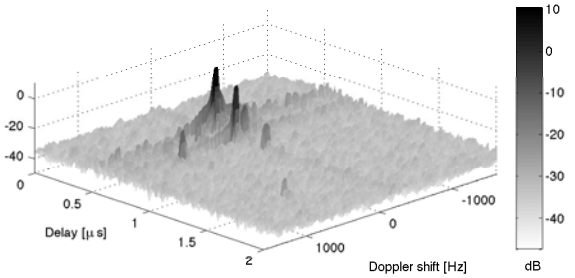

(b) LSF estimated with I=3 and J=2.

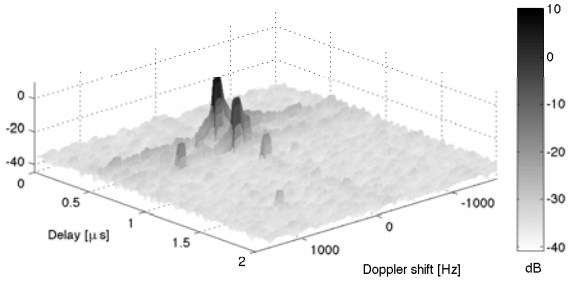

(c) LSF estimated with I=4 and J=6.

Figure 3.3: LSF estimated for a highway convoy measurement with intermittent LOS obstruction using $M = 128$ and different number of tapers (I, J).

might not be well represented because they are masked by the noise. For instance, the peak at 1.7 μs and 1000 Hz in subfigure (a).

If we increase the number of used tapers, the variance of the estimate is reduced at expenses of an increased bias. The variance reduction can be appreciated mostly on the noise floor, which becomes flatter, whereas the effect of the bias is manifested on the broadening of the peaks.

Subfigure (b) shows the estimated LSF of the same measurement using $I = 3$ and $J = 4$. Now, look at the same peak at position 1.7 μs and 1000 Hz, it appears more clear due to the reduction of the variance. On the other hand, notice the width of the strongest peak, which is now larger.

These two effects become more accentuated when increasing the number of tapers used by the estimator. For instance in the LSF estimated using $I = 4$ and $J = 6$ in subfigure (c), the variance has enormously decreased, notice the flatness of the noise floor, but the peaks have lost their acuteness and now have a rectangular shape.

We therefore, would like to find out what is the (I, J) pair which delivers the optimal trade-off between these two effects. In order to do that, we need to quantify the estimation error by comparing the outcome of the estimator and the true value of the variable we are estimating.

Ideally, we would like to have the true LSF of the process, but in reality, we only have at our disposal the measured finite length channel frequency responses $H[m, q]$. First, we need to find a way that allows us to obtain a relationship between the outcome of a second-order statistics estimator, i.e. the LSF estimator, and the true (measured) first order description of the process, i.e. the frequency response.

3.2.3.1 2D Wiener Filter Approach

In order to assess the performance of the estimator, we define the MSE based on the structure of a two-dimensional (2D) Wiener filter [85], because the Wiener filter coefficients can be calculated from the LSF. We point out that we do not use the Wiener filter for filtering a signal, but for characterizing the performance of the estimator. We do that by optimizing the parameters used for estimating the LSF with which we obtain the minimum MSE at the output of the 2D-Wiener filter described in Fig. 3.4 [85].

We consider a signal $R[m, q]$ to be filtered, which consists of the true (measured) channel transfer function $H[m, q]$ corrupted with additive complex Gaussian noise $N[m, q]$ as $R[m, q] = H[m, q] + N[m, q]$. The noise $N[m, q]$ is complex Gaussian distributed with zero mean and σ_N^2 variance. The filter coefficients are calculated from the estimated scattering function with the LSF estimator. The optimum LSF

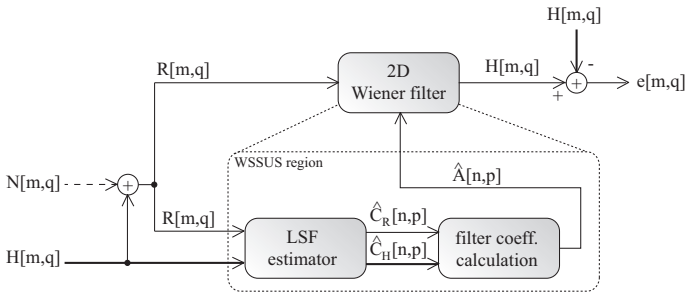

Figure 3.4: 2D Wiener filter scheme.

parameter set minimizes the MSE between the output of the filter $\hat{H}[m,q]$ and $H[m,q]$, without involving high computational complexity in the estimation process.

The estimated transfer function at the filter output reads

$$\hat{H}[m,q] = \sum_{m_i=0}^{M-1} \sum_{q_j=0}^{N-1} a[m,q] R[m-m_i, q-q_j] \tag{3.8}$$

where $a_{i,j}$ are the filter coefficients and M and N denote the length of the sequence $R[m,q]$ in time and frequency respectively. The MSE is given by

$$\mathcal{E} = E\{|e[m,q]|^2\}$$

where $e[m,q] = H[m,q] - \hat{H}[m,q]$ and $E\{\cdot\}$ denotes expectation. In order to find the coefficients of this 2D filter, we use the orthogonality principle [86]:

$$E\{e[m,q]\hat{H}^*[m'',q'']\} = 0$$

to obtain the Wiener-Hopf equation

$$E\{H[m,q]R^*[m'',q'']\} = \sum_{m',q'} a[m',q',m,q] E\{R[m',q']R^*[m'',q'']\}. \tag{3.9}$$

We assume that the noise $N[m,q]$ is a zero-mean process statistically independent of the channel frequency response $H[m,q]$. Under this assumption we can rewrite Eq. (3.9) as

$$E\{H[m,q]H^*[m'',q'']\} = \sum_{m',q'} a[m',q',m,q] E\{R[m',q']R^*[m'',q'']\}. \tag{3.10}$$

From Eq. (3.10) we see that $E\{H[m,q]H^*[m'',q'']\}$ is the time-frequency auto-correlation function of $H[m,q]$. Similarly, $E\{R[m',q']R^*[m'',q'']\}$ is the time-frequency auto-correlation function of $R[m,q]$. For short we rename these two time-frequency auto-correlation functions as R_H and R_R. In order to define the Wiener

filter, we must assume to have stationary processes, therefore the time-frequency auto-correlation functions will depend only on the time and frequency lags and can be expressed as $R_H[\Delta m, \Delta q]$ and $R_R[\Delta m, \Delta q]$.

3.2.3.2 Filter Implementation

The time-frequency filter can be written as the 2D time-frequency-convolution (see Eq. (3.8))

$$\hat{H}[m,q] = a[m,q] * R[m,q], \tag{3.11}$$

with $a[m,q]$ denoting the filter coefficients. Performing the Fourier transform in both dimensions, we can express (3.11) as

$$\begin{aligned} \mathcal{F}_m\mathcal{F}_q^{-1}\left\{\hat{H}[m,q]\right\} &= \mathcal{F}_m\mathcal{F}_q^{-1}\left\{a[m,q] * R[m,q]\right\} \\ S_{\hat{H}}[p,n] &= A[p,n]S_R[p,n], \end{aligned} \tag{3.12}$$

where $S_{\hat{H}}[p,n]$ and $S_R[p,n]$ are the Doppler-delay spreading functions of $\hat{H}[m,q]$ and $R[m,q]$. In (3.12) $\mathcal{F}$ and $\mathcal{F}^{-1}$ denote the Fourier transform and its inverse respectively. The filter coefficients $A[p,n]$ are given by

$$A[p,n] = \mathcal{F}_m\mathcal{F}_q^{-1}\left\{\frac{R_H[\Delta m, \Delta q]}{R_R[\Delta m, \Delta q]}\right\} = \frac{|S_H[p,n]|^2}{|S_R[p,n]|^2} = \frac{C_H[p,n]}{C_R[p,n]}, \tag{3.13}$$

with $C_H[p,n]$ and $C_R[p,n]$ denoting the Doppler-delay scattering functions of $H[m,q]$ and $R[m,q]$ respectively. Since we know the true channel transfer function, we are able to calculate $S_H[m,q]$ and $C_H[m,q]$ directly from $H[m,q]$. In order to obtain $\hat{H}[m,q]$ we only need to reverse the sequence of Fourier transforms performed in Eq. (3.12) at the output of the filter.

3.2.3.3 Calculation of the Filter Coefficients

The filter coefficients determined in Eq. (3.13) depend on the scattering functions $C_R[p,n]$ and $C_H[p,n]$. We calculate an estimate of them using the LSF estimator. Since we are dealing with non-WSSUS processes, the observed signal at the input of the filter is divided in time-frequency regions over which we can assume that the WSSUS property holds. This allows us to calculate the second-order moments of the process and, consequently, the filter coefficients.

The filter coefficients defined in Eq. (3.13) are locally valid for each WSSUS region indexed with (k_t, k_f). They are use to filter $R[m,q]$ after the estimation procedure (Fig. 3.4).

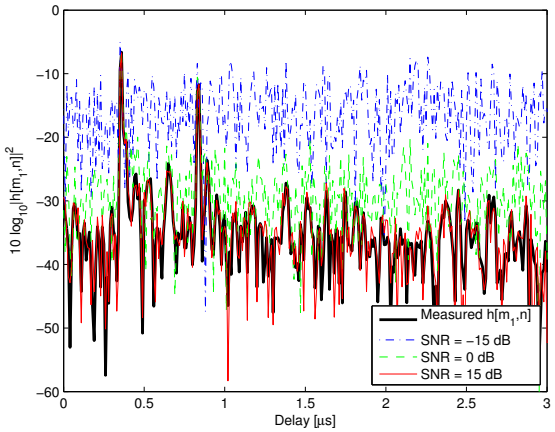

Figure 3.5: Snapshot of a channel impulse response with additive Gaussian noise for different SNRs values.

The filter coefficients are calculated from estimated functions, therefore we will use estimates of the filter coefficients, $\hat{A}[p,n]$. The local filter coefficients for the WSSUS region defined by k_t and k_f read

$$\hat{A}[k_t,k_f;n,p]=\frac{\hat{C}_H[k_t,k_f;n,p]}{\hat{C}_R[k_t,k_f;n,p]}.$$

It is known that this solution is optimal for noise filtering [86]. Nevertheless, we note here that the problem we aim to solve is the optimum choice of the parameters used for estimating the LSF. In the estimator (3.4) there is an optimal number of windows in time and frequency that reduces the overall MSE.

3.2.3.4 LSF Parameters Optimization

Since the measured time-varying channel transfer function $\tilde{H}[m,q]$ has a SNR of roughly 40 dB, we consider $\tilde{H}[m,q]$ as the true transfer function, $H[m,q]\simeq\tilde{H}[m,q]$. The noise-corrupted transfer function $R[m,q]$ is created by adding random complex Gaussian noise to $H[m,q]$. For the investigation here we consider different σ_N^2 values in order to achieve SNR of $-15\,\mathrm{dB}$, $0\,\mathrm{dB}$, and $15\,\mathrm{dB}$. Figure 3.5 shows the noise-corrupted channel impulse response for different SNR values. We investigate the effect of different SNRs in order to analyze the dependency of the optimization result with respect to the amount of added noise.

For this investigation we use $S=32500$ samples covering a recorded time of 10 s, and $Q=512$ frequency bins for $B=240\,\mathrm{MHz}$ bandwidth of a single link

$l = 10$, which corresponds to the TX-antenna element 3 and RX-antenna element 3 radiating towards the driving direction.

We optimize the number of tapers I and J used in the LSF estimator in time, and in frequency, respectively. This optimization is performed given a *minimum stationarity region* with dimension $M \times N$. M has to be selected in order to ensure the WSS property and N the US property. Choosing M properly, we can ensure that contributions at different delays are not correlated (they come from different scatterers). For now, we assume that values of $M < 512$ samples ensure the fulfillment of the WSS property and with that, we consider the US property to hold for the whole measurement bandwidth. For the sake of simplicity, in this analysis we set $M = 64, 128, 256, 512$, $N = 512$ and SNR= 0 dB.

Based on that, we drop the index k_f from expressions (3.4) and (3.14), leaving only the dependence on k_t.

The choice of the time-bandwidth product determines the number of tapers used in the estimation process [81]: $I < 2\mathcal{N}_t\mathcal{W}_t$ in the time domain and $J < 2\mathcal{N}_f\mathcal{W}_f$ in the frequency domain, where $\mathcal{N}_t\mathcal{W}_t = i/\Delta m$ and $\mathcal{N}_j\mathcal{W}_f = j/\Delta n$ ($\mathcal{N}_t\mathcal{M}_t = i$ and $\mathcal{N}_f\mathcal{M}_f = j$ when using normalized Δm and Δn).

The term to be optimized is the MSE, computed over a total number of K_t WSSUS regions. The normalized MSE is defined as

$$\mathcal{E} = \frac{1}{K_t}\sum_{k_t=1}^{K_t}\frac{\sum_{m'=-M/2}^{M/2-1}\sum_{q=-N/2}^{N/2-1}|H^{(k_t)}[Mk_t+m',q]-\hat{H}^{(k_t)}[Mk_t+m',q]|^2}{\sum_{m'=-M/2}^{M/2-1}\sum_{q=-N/2}^{N/2-1}|H^{(k_t)}[Mk_t+m',q]|^2} \quad (3.14)$$

with $K_t = \lfloor\frac{S-M}{\Delta_t}\rfloor$, $I < 2i$, $J < 2j$, and $M \times N$ denoting the extent of the WSSUS region.

Our optimization problem is thus to find the minimum (I, J) pair giving a reasonable low MSE. With that we want to obtain a good estimate of the LSF without having high computational complexity, since we are going to apply the estimator to a large amount of data.

We evaluate the MSE for all possible combinations of I and J from, for $I \in \{1, \ldots, 6\}$ and $J \in \{1, \ldots, 6\}$.

Figure 3.6 plots the obtained MSEs versus (I, J) for an urban single lane intersection measurement (subfigures 3.6 (a) and (c)), and for a convoy highway measurement with intermittent LOS obstruction (subfigures 3.6 (b) and (d)). We choose these two measurements in order to represent two very different environments: urban with rich scattering driving in opposite directions, and highway with less scattering driving in the same direction. The results shown in Fig. 3.6 (a) and (c) consider an SNR=15 dB, and in (b) and (d) the SNR=0 dB.

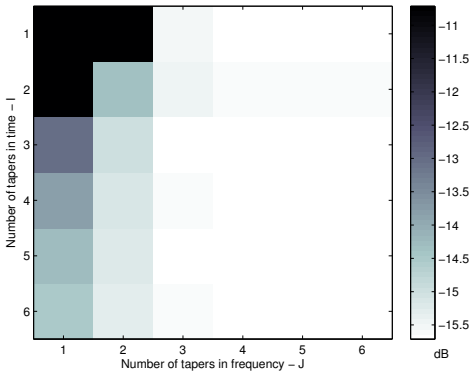

(a) MSE versus (I, J) for scenario RC-usl with $M = 64$ samples and SNR=15 dB.

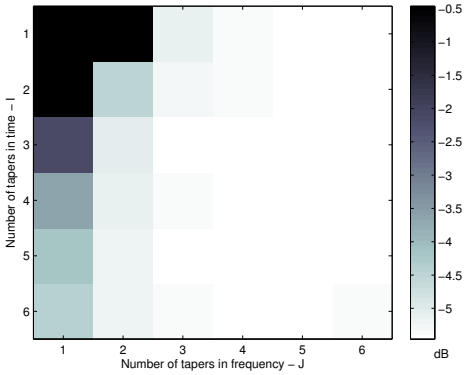

(b) MSE versus (I, J) for scenario GLO-h with $M = 64$ and $M = 512$ samples and SNR=0 dB.

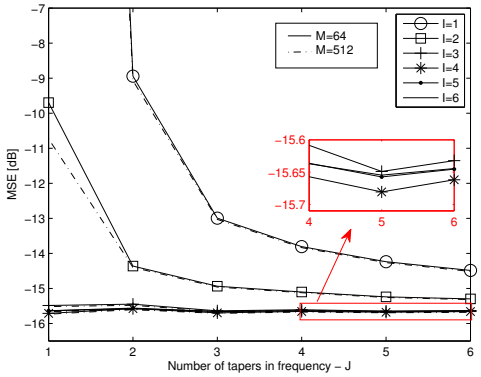

(c) MSE versus (I, J) for scenario RC-usl with $M = 64$ and $M = 512$ samples and SNR=15 dB.

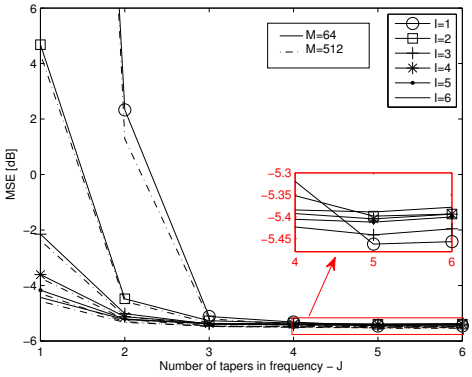

(d) MSE versus (I, J) for scenario GLO-h with $M = 64$ samples and SNR=0 dB.

Figure 3.6: MSE versus number of tapers (I, J) for two different measurements, (a) and (c) are a road crossing - urban single lane, and (b) and (d) are a general LOS obstruction - highway.

First we want to highlight that the MSE decreases slowlier with increasing I than with increasing J. This indicates that the LSF estimator needs more tapers to correctly describe the time/Doppler fluctuations of the channel.

Secondly, the MSE converges to a minimum after considering 3 tapers in both domains. Nevertheless, the minimum is reached for another (I, J) pair, look at the sub-plots highlighted in red in Figs. 3.6 (c) and (d). For the road crossing measurement with an SNR=15 dB, the minimum is achieved for $I = 4$, and $J = 5$. For the highway measurement with an SNR=0 dB, the minimum is achieved for $I = 1$, and $J = 5$. In order to make the choice of (I, J) independent of the scenario and the SNR, we select $I = 3$ and $J = 3$, and consider that with these values, the estimator performs well without an unnecessarily increased computational complexity.

Furthermore, we also include the results obtained with $M = 512$ samples in Figs. 3.6 (c) and (d), plotted in dash-dotted line. Noteworthy is that the convergence to the minimum MSE agrees for both choices of M, i.e. the resulting MSE does not depend strongly on the parameter M. Results for other M values are in between the lines for 64 and 512 samples.

Regarding the SNR investigation, the remark here is that the achieved minimum MSE is smaller for larger SNRs, as one might expect. Even though the results for the different SNRs depicted in Fig. 3.6 correspond to two different measurement scenarios, the observed effect of the SNR on the MSE holds for all measurements in all scenarios.

We performed the same (I, J) optimization analysis in 10 different measurement runs, each one representing one vehicular scenario, as described in Chap. 1, and validated that:

- The MSE decreases slowlier with increasing I than with increasing J, thus confirming the strong time-variation of the channel.
- The MSE reaches a minimum for $I = 3$ and $J = 3$ number of tapers in time and frequency.
- The size of M does not have a strong influence neither on the MSE results, nor on the (I, J) choice.
- The larger the SNR, the smaller the MSE, but the optimal number of tapers (I, J) remains the same.

3.3 The Delay and Doppler Projections of the LSF the PDP and DSD

The LSF $\hat{\mathcal{C}}[k_t, k_f; n, p]$ as defined in Eq. (3.4) is a function of four variables, time index k_t, frequency index k_f, delay index n, and Doppler shift index p. Nevertheless, an easier representation of the LSF is preferable. The use of the power delay profile (PDP) and the Doppler power spectral density (DSD) functions for describing how the signal power is spread by the channel in time and frequency is widely used. The PDP is the projection of the LSF in the delay domain, whereas the DSD is the projection of the LSF in the Doppler domain.

For non-WSSUS channels, the PDP and the DSD are time-frequency dependent. Based on $\hat{\mathcal{C}}[k_t, k_f; n, p]$, the time-frequency-varying PDP and time-frequency-varying DSD can be defined as

$$\hat{P}_\tau[k_t, k_f; n] = E_p\{\hat{\mathcal{C}}[k_t, k_f; n, p]\} = \frac{1}{M} \sum_{p=-M/2}^{M/2-1} \hat{\mathcal{C}}[k_t, k_f; n, p] \tag{3.15}$$

and

$$\hat{P}_\nu[k_t, k_f; p] = E_n\{\hat{\mathcal{C}}[k_t, k_f; n, p]\} = \frac{1}{N} \sum_{n=0}^{N-1} \hat{\mathcal{C}}[k_t, k_f; n, p], \tag{3.16}$$

where $E_x\{\cdot\}$ denotes expectation over the variable x.

We consider the combined LSF for $L = 16$ links in order to resemble an omnidirectional antenna radiation pattern as

$$\hat{\mathcal{C}}[k_t, k_f; n, p] = \frac{1}{L} \sum_{l=1}^{L} \hat{\mathcal{C}}^{(l)}[k_t, k_f; n, p], \tag{3.17}$$

where $\hat{\mathcal{C}}^{(l)}[k_t, k_f; n, p]$ is the LSF estimated for each individual link l as in Eq. (3.4).

We show in Fig 3.7 the time-varying PDP and the time-varying DSD for two different frequencies obtained for a convoy highway measurement. The WSSUS region is chosen to be $M = 128$ samples in time and $N = 256$ samples in frequency, which results in a 40 ms long and 80 MHz wide WSSUS region. The time shift $\Delta k_t = 64$, and the frequency shift $\Delta k_f = 128$.

First, we would like to highlight the strong time-variability of the PDP and the DSD, mainly observed in the PDP. On the other hand, there are not such big frequency variations, compare Fig. 3.7 (a) with (c), and (b) with (d). The impact of the time-variability and frequency-variability of the LSF is going to be investigated in the next chapter. But as an introductory remark, we note here already the difference

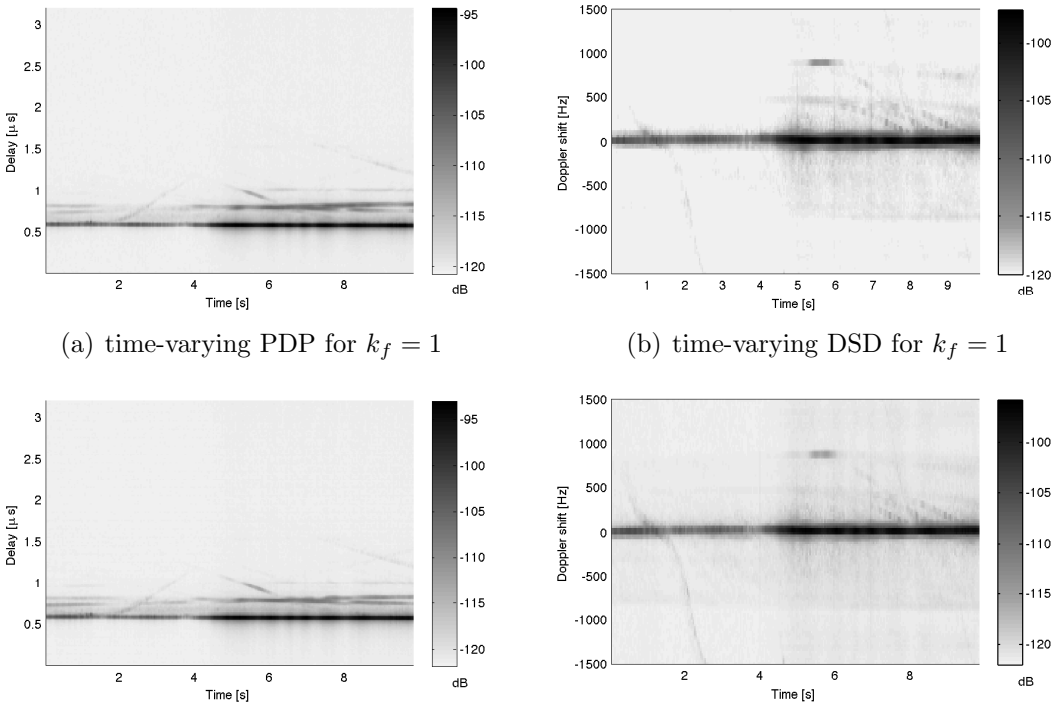

(a) time-varying PDP for $k_f = 1$

(b) time-varying DSD for $k_f = 1$

(c) time-varying PDP for $k_f = 5$

(d) time-varying PDP for $k_f = 5$

Figure 3.7: Time-varying PDP and DSD for a WSSUS region of dimensions $M = 128$ time samples, i.e. 40 ms, and $N = 256$ frequency samples, i.e. 80 MHz. A $k_f = 1$ limits a frequency region of 80 MHz bandwidth centered at 40 MHz, a $k_f = 5$ limits a frequency region of 80 MHz bandwidth centered at 200 MHz.

between time-variability and frequency-variability, being the time fluctuations much more pronounced.

As commented before, the size of M and N is going to determine the resolution achieved in the LSF in the delay and Doppler domains, and consequently the resolution of the PDP and the DSD.

3.3.1 Examples and General Comments

Based on the observation we made from the results plotted in Fig. 3.7, let us consider here the whole bandwidth for the calculation of the LSF and the resulting PDP and DSD. We then eliminate the frequency dependence k_f in Eq. (3.15) and (3.16). With that, we can plot the PDP with more resolution.

In Fig. 3.8 we plot the the PDP and the DSD of the same scenario now with $M = 128$ time samples and $N = 769$ frequency samples. Besides it, we also plot the results of three other representative measurements. Subfigures (a) and (b) show the results for a general LOS obstruction - highway measurement, subfigures (c) and (d) are for a road crossing - urban single lane measurement, and finally, (e) and (f) plot the results for a in-tunnel measurement. In order to make the analysis easier to follow, in each one of the PDPs and DSDs we indicate in roman numerals the contribution of different scatterers. An illustrative example of the PDP and the DSD for the rest of the measured scenarios can be found in the App. A.

General LOS obstruction - highway (GLO-h)
We analyze first the GLO-h time-varying PDP and DSD in Figs. 3.8 (a) and (b). The TX-RX link is obstructed by a truck, all three vehicles are driving at about 120 km/h (33.33 m/s). During the measurement run, which lasts 10 seconds, the truck in between the two cars changes lane and leaves the LOS without obstruction.

Since this is a convoy measurement, the Doppler shift component remains constant at 0 Hz, because the relative speed between TX and RX does not change. We can also appreciate that by looking at the PDP in subfigure 3.8 (a), where the first component remains also constant in delay.

It is possible to identify 5 relevant MPCs, visually more evident in the PDP in Fig. 3.8 (a):

(i) The LOS path, which has the smallest delay and the highest power. Noteworthy here is that the strength of the LOS increases at 4.2 s when the truck changes lane, this can be more clearly appreciated in the DSD plot, in Fig. 3.8 (b).

(ii) Reflections stemming from trucks driving in the opposite direction. We identify three intervals. During the first interval, the truck is approaching the TX from

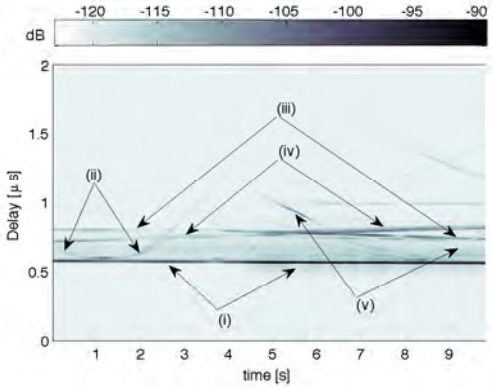

(a) time-varying PDP for a general LOS obstruction - highway measurement

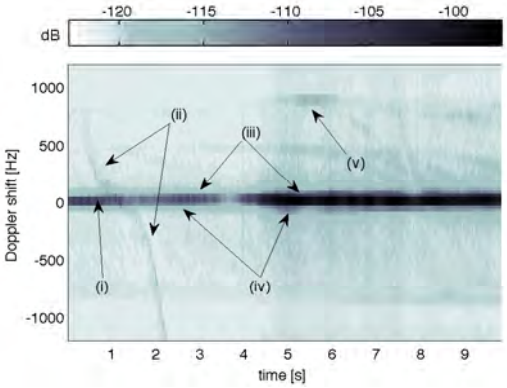

(b) time-varying DSD for a general LOS obstruction - highway measurement

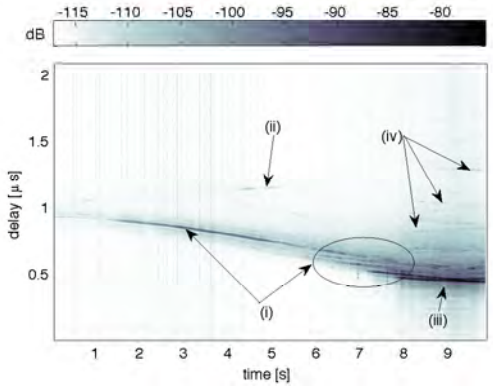

(c) time-varying PDP for a road crossing - urban single lane measurement

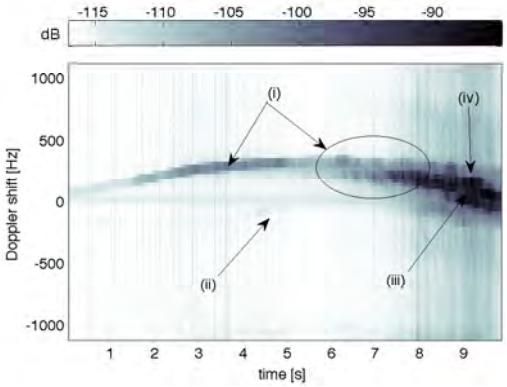

(d) time-varying DSD for a road crossing - urban single lane measurement

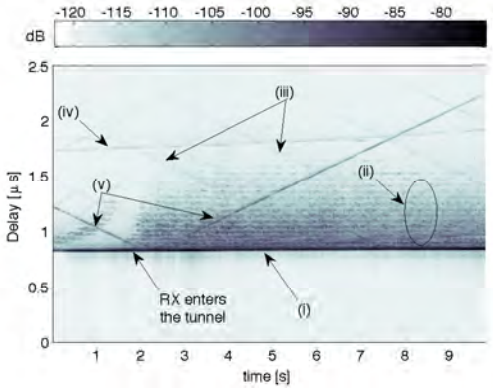

(e) time-varying PDP for an in-tunnel measurement

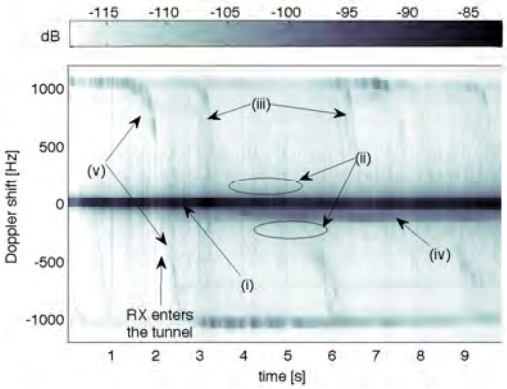

(f) time-varying DSD for an in-tunnel measurement

Figure 3.8: Time-varying PDP and DSD for a WSSUS region of dimensions $M = 128$ time samples, i.e. 40 ms, and $N = 769$ frequency samples, i.e. 240 MHz.

0 s until 0.8 s and the delay of the MPC decreases. The Doppler shift is positive with decreasing value as the truck gets closer. Then the truck is between the cars during almost 1 s. In the PDP we observe a component constant very close to the LOS delay. In the DSD, the Doppler shift stays around 0 Hz. Finally, around 4 s, the truck moves further away, the delay increases again until it fades out with the received power of the MPC, the Doppler shift becomes negative and increases as the truck leaves.

(iii) A truck driving at a constant speed in front of the RX originates the component *(iii)*. Here again, the strength of the received signal increases when TX and RX are obstacle free, from 4.2 s on. Since the relative speed between TX-RX and the truck is constant, the Doppler shift component is at 0 Hz and can not be easily differentiated in the DSD plot in Fig. 3.8 (d).

(iv) The fourth component is originated by an object behind the TX-RX, probably another truck driving behind. The Doppler component is not observable due to the same reason as in *(iii)*.

(v) As described for contribution *(ii)*, the last MPC is caused by another truck approaching the from the opposite direction. Even though the lifetime of this MPC can be defined between 4.5 and 10 s, the contribution has enough power to be identified in the DSD plot between 5 and 6 s, with a positive value of 1000 Hz. Observing the curvature of the lines described by contributions *(ii)* and *(v)*, one can easily conclude that the truck in *(ii)* drives faster than the one in *(v)*. This can be observed in the curvature of the delay component in the PDP and the value of the initial Doppler shift.

Road crossing - urban single lane (RC-usl)

Now, we look at the subfigures 3.8 (c) and (d) for the RC-usl scenario. In the PDP and the DSD figures we can identify the following effects:

(i) From 0 to 7 seconds the two cars approach the crossing from perpendicular streets without LOS, see Fig. 2.9 (c). Due to multipath reflections on the buildings in the street or other cars parked beside the road, signal can be still transmitted from the TX to the RX. This is why we observe a weak signal component during this time interval in both figures.

Furthermore, in the DSD we notice that the signal component is curved, starting from values of Doppler shift of 0 Hz and increasing to 300 Hz and then decreasing again. This is caused by the TX car, which was in a static position at the beginning of the measurement, accelerated at the start of the measurement, and braked when arriving at the crossing.

There is clearly one object which dominates as scatterer, nevertheless, as we are

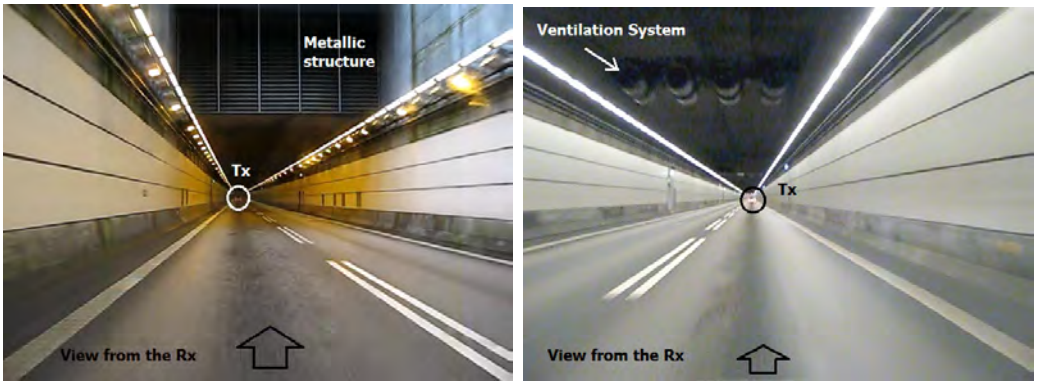

(a) View 1, Rx has not entered the tunnel yet.

(b) View 2, Tx and Rx are inside the tunnel.

Figure 3.9: Pictures taken during the in-tunnel measurement.

close to the crossing between 6 and 7 seconds, other closer objects become more relevant and we therefore observe more parallel MPCs, which are not distinguishable in the DSD plot in Fig. 3.8 (d).

(ii) We also observe some late components coming from reflections from other objects on the street, as at 4.5 s in Fig. 3.8 (c) and (d), even though it is very weak in the DSD.

(iii) There is a second region clearly distinguishable in figures 3.8 (c) and (d) between seconds 7 and 10. During this time interval both cars are at the crossing, the TX stops to give way to the RX, which passes by. Here a strong LOS component is present.

(iv) Furthermore, more MPCs can be identified parallel to the contribution *(iii)*. The TX and RX are placed in a more open area and both direct link and reflections with other near-by objects are stronger.

In-tunnel (IT)

An interesting effect due to the tunnel geometry can be observed in the PDP and the DSD for the IT measurement in subfigures 3.8 (e) and (f). The TX is inside the tunnel and the RX enters it at approximately 2 seconds. Then, several typical propagation phenomena for IT scenarios can be observed:

(i) There is a strong LOS between the TX and the RX. The Doppler shift of the LOS component in the DSD remains constant at around 0 Hz in Fig. 3.8 (e), since both cars drive in the same direction and more or less at the same speed. In the PDP the delay component of this contribution also remains constant in time.

(ii) Multiple signal components appear parallel to the LOS in the PDP and the DSD due to reflections from the tunnel walls and ceiling.

(iii) Equidistant MPCs are caused by reflections on the ventilation system in the tunnel.

(iv) In the PDP we can also observe other MPCs caused by cars driving inside the tunnel, the strongest one is indicated by *(iv)*. The object causing the reflection drives faster than the TX and the RX in the same direction, and therefore it has a negative Doppler shift close to 0 Hz, and presents an increasing delay.

(v) A strong reflection is caused by a big metallic structure at the entrance of the tunnel.

Concluding Remarks

We summarize the effects on the PDP and DSD observed in all scenarios (whose PDP and DSD can be found in the App. A). Each group of MPCs can be associated to one scatterer. We list the objects originating the most relevant contributions as:

- *The LOS component* between TX and RX. It might be obstructed in some occasions, such as in the general LOS obstruction - highway scenario.
- *Other cars acting as scatterers*. The cars can be in a static position or be mobile. These kind of scatterers are more relevant in non-LOS conditions, given that the total received power is more equally distributed among the MPCs. This is mainly observed in rich scattering scenarios and it is not so present in rural and suburban environments.
- *Trucks or vans*, which can also move or be static. They contribute with stronger MPCs than the reflections stemming from other cars, because they are bigger objects, and usually with metallic surfaces, which make them good reflectors.
- *Big metallic structures* such as traffic signs, street lamps, bridges, and in-tunnel ventilation systems.
- *The ceiling and the walls* in an in-tunnel scenario, where multiple reflections stemming from the same object arrive at different delays.

4 The (in-)Validity of the WSSUS Assumption in Vehicular Radio Channels

The wide sense stationary (WSS) and the uncorrelated scattering (US) assumptions for wireless propagation channels imply that channel *statistics* (but not the channel realizations) are independent of time and center frequency. They allow a greatly simplified statistical description of channels, and - even more importantly - form the basis of many designs and analysis of wireless transceivers. However, the WSSUS assumption is not always fulfilled in practice.

The WSS and the US assumption are introduced in [1] for propagation channels. Later work has shown that they are WSS only for a limited time-span, and US for a limited bandwidths in cellular scenarios [2]. These limitations are particularly pronounced in vehicular, and more precisely, V2V propagation channels.

When considering a non-stationary channel, the fading statistics have to be estimated as they change, both in time and in frequency. Therefore it is important to assess for how long they can be considered to remain more or less constant, i.e. they are stationary.

4.1 Stationarity Assesment

The basis of our assessment is the time-varying frequency response $H(t, f)$ of the "effective" propagation channel, introduced in Chap. 3. It includes the effects of the physical channel, the transmit, and the receive filter of the channel sounder used for the measurements.

We make use of the LSF for representing time-frequency variations of the fading process in the power spectral domain, namely in the delay-Doppler plane. We apply the LSF estimator described in Chap. 3 to the measured discrete channel frequency responses $H[m, q]$.

Since we do not know for how long in time and in frequency the WSS and the US properties can be assumed to hold, we first define a *minimum stationarity region* of

dimensions $M \times N$, used for obtaining the LSF, $\hat{\mathcal{C}}[k_t, k_f; n, p]$ from the $H[m, q]$ (see Eq. (3.4) and Fig. 3.2).

We recall here the range and the resolutions of the different variables: $k_t \in \{1, \ldots, \lfloor \frac{S-M}{\Delta_t} \rfloor\}$ and $k_f \in \{1, \ldots, \lfloor \frac{Q-N}{\Delta_f} \rfloor\}$ are the time and the frequency index of each stationarity region, and correspond to its center; $n \in \{0, \ldots, N-1\}$ denotes the delay index; and $p \in \{-M/2, , \ldots, M/2-1\}$ the Doppler index, respectively. The variables k_t and k_f have a resolution of $k_{ts} = \Delta_t t_s$ and $k_{fs} = \Delta_f f_s$, respectively. The delay resolution is defined by $\tau_s = 1/(N f_s)$, and the Doppler resolution by $\nu_s = 1/(M t_s)$.

The relative time index within each stationarity region is denoted by the variable $m' \in \{-M/2, \ldots, M/2-1\}$, and the relative frequency index by $q' \in \{-N/2, \ldots, N/2-1\}$. The relationship between the relative and absolute time index is given by $m = [(k_t - 1)\Delta_t + m'] + M$, where Δ_t denotes the time shift between consecutive stationarity regions. In the frequency domain the relationship is $q = [(k_f - 1)\Delta_f + q'] + N$, where Δ_f denotes the frequency shift.

4.1.1 Definition of Stationarity

Stochastic processes whose statistical properties do not change with absolute time are considered to be stationary in time, i.e. WSS. Likewise, stationarity in frequency relates to the US property (refer to Chap. 3 for a more detailed explanation about the WSS and US properties).

Based on that, we refer to non-stationary processes as those whose first and second order statistical description changes over time, violating the WSS condition, and, over frequency, violating the US condition.

For testing stationarity, we first calculate the LSF for the *minimum stationarity region*. Afterwards, we are interested in investigating whether it can be enlarged. In order to do that, we need to test whether neighboring LSFs (shifted by Δk_t in time and Δk_f in frequency) are similar enough such that the fading process can be considered stationary.

To make precise the notion of *similar enough*, we use two spectral distance metrics:

1. The *spectral divergence (SD)*, which measures distances between strictly positive power spectra. It is an unbounded metric.

2. The *collinearity*, which is a bounded metric based on the angle between vectorized channel correlation matrices.

We are interested in testing the stationarity of the channel regardless of the direction. Therefore, we do not consider the LSF of each link individually, but we

calculate the combined LSF for the $L = 16$ links in order to resemble an omnidirectional antenna radiation pattern as

$$\hat{\mathcal{C}}[k_t, k_f; n, p] = \frac{1}{L} \sum_{l=1}^{L} \hat{\mathcal{C}}^{(l)}[k_t, k_f; n, p], \tag{4.1}$$

where $\hat{\mathcal{C}}^{(l)}[k_t, k_f; n, p]$ is the LSF estimated for each individual link l as in Eq. (3.4).

We choose the *minimum stationarity region* to have dimensions $M = 64$ samples in time corresponding to 19.66 ms and $N = 64$ samples in frequency corresponding to 19.97 Hz. We select the sliding shift to be half of the *minimum stationarity region* dimension, i.e. $\Delta_t = 32$ samples in the time domain and $\Delta_f = 32$ samples in the frequency domain.

4.2 An Unbounded Spectral Distance Metric: the Spectral Divergence

In [87] a spectral metric is introduced, which relates the power spectral density of a process and the degradation observed in the MSE obtained after Wiener filtering a noisy observation of the same process using wrong statistical knowledge about it.

The degradation is created by assuming a mismatched power spectral density when designing the filter coefficients. Since we want to test stationarity, the mismatch comes from using the statistical description (LSF) of the process in neighboring stationarity regions, shifted by Δk_t in time and Δk_f in frequency.

We base the analysis in this section on the 2D Wiener filter approach introduced in Chap. 3, see Fig. 3.4.

The Wiener filter is optimum in terms of minimum MSE. When we make a mistake by using the mismatched filter coefficients $A_m^{(k_t+\Delta k_t, k_f+\Delta k_f)}[n, p]$ instead of the exact ones $A_e^{(k_t,k_f)}[n, p]$, we observe an increase in the MSE.

We quantify this degradation with respect to the filter coefficients choice as

$$\rho^{(\mathrm{MSE})}(A_e^{(k_t,k_f)}[n, p], A_m^{(k_t+\Delta k_t, k_f+\Delta k_f)}[n, p]) = \frac{E\{|H[m, q] - \hat{H}_{A_m}[m, q]|^2\}}{E\{|H[m, q] - \hat{H}_{A_e}[m, q]|^2\}}, \tag{4.2}$$

where $\hat{H}_{A_m}[m, q]$ and $\hat{H}_{A_e}[m, q]$ are the estimated channel transfer functions using the mismatched or the exact filter respectively.

In [87] the error variance $\rho^{(\mathrm{MSE})}$ is expressed in terms of power spectral densities. This reformulation leads to a definition of a distance $\delta(t_1, t_2)$ for the filtering problem. The distance measure depends on the ratio of two power spectral densities. We use the discretized version of this measure called spectral divergence SD.

We define the SD in time as

$$\delta_t[k_t, k_t+\Delta_{k_t}] = \log(\rho_t^{(C)}[k_t, k_t+\Delta_{k_t}]) = \tag{4.3}$$
$$\log\left(\frac{1}{(K_f NM)^2}\sum_{k_f}\sum_{n}\sum_{p}\frac{\hat{\mathcal{C}}[k_t,k_f;n,p]}{\hat{\mathcal{C}}[k_t+\Delta_{k_t},k_f;n,p]}\sum_{k_f}\sum_{n}\sum_{p}\frac{\hat{\mathcal{C}}[k_t+\Delta_{k_t},k_f;n,p]}{\hat{\mathcal{C}}[k_t,k_f;n,p]}\right)$$

between two time instances k_t and $k_t+\Delta_{k_t}$ separated by Δ_{k_t}.

Similarly, the SD between two frequency regions k_f and $k_f+\Delta_{k_f}$ separated by Δ_{k_f} reads

$$\delta_f[k_f, k_f+\Delta_{k_f}] = \log(\rho_f^{(C)}[k_f, k_f+\Delta_{k_f}]) = \tag{4.4}$$
$$\log\left(\frac{1}{(K_t NM)^2}\sum_{k_t}\sum_{n}\sum_{p}\frac{\hat{\mathcal{C}}[k_t,k_f;n,p]}{\hat{\mathcal{C}}[k_t,k_f+\Delta_{k_f};n,p]}\sum_{k_t}\sum_{n}\sum_{p}\frac{\hat{\mathcal{C}}[k_t,k_f+\Delta_{k_f};n,p]}{\hat{\mathcal{C}}[k_t,k_f;n,p]}\right).$$

The sums in Eq. (4.3) and (4.4), run over the variables k_t, k_f, n, and p, with the following limits $k_t \in \{1,\ldots,\lfloor\frac{S-M}{\Delta_t}\rfloor\}$, $k_f \in \{1,\ldots,\lfloor\frac{Q-N}{\Delta_f}\rfloor\}$, $n \in \{1,\ldots,N-1\}$, and $p \in \{-M/2,\ldots,M/2-1\}$.

The SD is a (pseudo)metric because it does not detect changes due to scaling by multiplicative constants. Therefore, we use this metric to qualitatively test how "*far*" two power spectral densities are from each other. Precisely, the SD fulfills:

- $\delta[x,y] \geq 0$,
- $\delta[x,y] = 0$ iff $C[x] = \alpha C[y]$, with α being a constant, and
- $\delta[x,y] = \delta[y,x]$.

This quantity is a good indicator for detecting changes between two spectral densities, more precisely, it compares their shapes. The relation of δ_t and δ_f with ρ_{MSE} gives it its practical relevance. When the two compared power spectral densities are equal, their SD is zero and increases when they get more dis-similar.

Note that $\delta_t[k_t, k_f+\Delta k_t] \geq 0$ with equality iff $\hat{\mathcal{C}}[k_t,k_f;n,p] = \hat{\mathcal{C}}[k_t+\Delta k_t,k_f;n,p]$, which is fulfilled for a WSS fading process. And similarly, $\delta_f \geq 0$ with equality iff $\hat{\mathcal{C}}[k_t,k_f;n,p] = \hat{\mathcal{C}}[k_t,k_f+\Delta k_f;n,p]$, which is valid for US.

4.2.1 Stationarity Assessment using the SD

We have already mentioned that the SD is an unbounded metric. Nevertheless, we are interested in quantifying the stationarity, therefore, we need to set a threshold

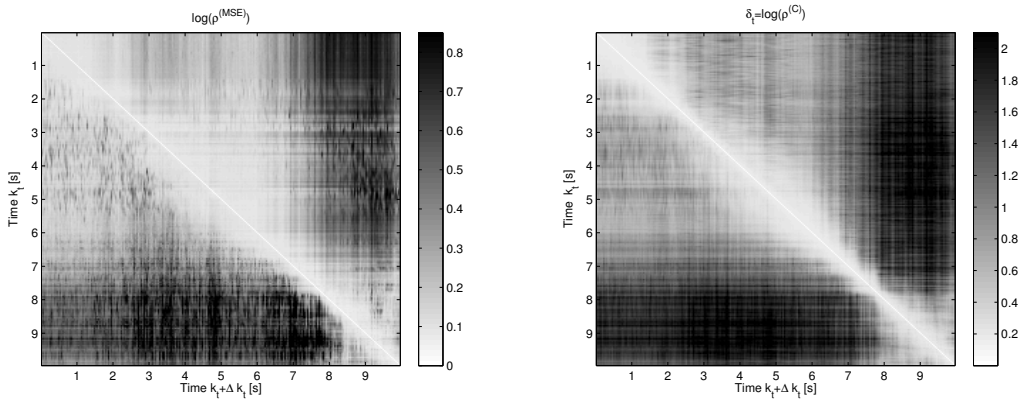

(a) MSE degradation

(b) SD in time

Figure 4.1: MSE degradation and SD in time for an opposite directions measurement in an urban road crossing with single lane streets. Used parameters: $M = 128$, $N = 512$, $Q = 512$.

upon which we can make a decision about stationarity. In an effort to determine the value of this threshold, we return back to the motivation of the SD in [87], where the metric $\rho^{(C)}$ is derived based on the degradation of the MSE, $\rho^{(\mathrm{MSE})}$, after Wiener filtering a process with wrong (mismatched) statistical knowledge. We are interested in finding, if there is any, the relationship between these two functions: the SD, $\delta = \log(\rho^{(\mathrm{C})})$, and the MSE degradation, $\rho^{(\mathrm{MSE})}$.

We follow the approach presented in [69], where we calculate the logarithm of $\rho^{(MSE)}$ and compare it to the SD. For the sake of simplicity, we assume here that M is chosen such that both WSS and US assumptions hold within the minimum stationarity region, as done previously for the taper investigation in Chap. 3.

We consider a road crossing measurement (opposite directions) in an urban environment (single lane streets). In order to draw conclusions such that they are valid for different propagation environments, we perform the same analysis also for a convoy measurement in a highway scenario.

First, we have a look at the MSE degradation and the SD for the road crossing measurement only. We plot them in Fig. 4.1 (a) and (b) respectively, and observe that they follow the same structure, having their respective minima in the diagonal. Remember that we are interested in finding out the correlation between the output of these two functions.

The elements in the diagonal in Fig. 4.1 (a) are the result of the degradation of the MSE with respect to the minimum MSE when using the $\Delta k_t = 0$ shifted

statistical information. This is 0 because we are using the current (exact) statistical information, and therefore there is no degradation. Similarly, the diagonal in Fig. 4.1 (b) contains the SD results from comparing one LSF with the $\Delta k_t = 0$ shifted LSF, i.e. with itself, and therefore $\delta_t = 0$.

The upper triangular elements show the results for $\Delta k_t > 0$, thus indicating values obtained when assuming longer stationarity lengths than the minimum, i.e. using the channel statistics over the next (future) Δk_t stationarity regions. Conversely, the lower triangular elements represent the error increase if in the previous Δk_t stationarity regions (past) the current statistical description of the channel was assumed. Considering $\Delta k_t < 0$ is unrealistic because it would imply the use of statistical information of "future" k_t regions. Therefore, we only consider the upper triangular part of $\rho^{(MSE)}$ and δ_t.

The scatter plots in Fig. 4.2 show the relationship between these two functions for the two chosen measurement scenarios (opposite directions in an urban road crossing (a), and convoy in a highway (b-c)), and for two different SNR values (SNR=10 dB (a-b), and 0 dB (c), see Fig. 3.5 for a graphical representation of the effect of adding noise to a measured CIR).

The plot on the right hand side of each figure is the zoomed-in section marked with dotted line. This area corresponds to values of $\rho^{(MSE)}$ between 1 and 2, and values of δ_t between 0 and 1. The range of $\rho^{(MSE)}$ equals a MSE degradation from 0% to 100%, i.e. from no degradation to doubling the minimum MSE.

In all three subfigures we plot the scatter points corresponding to using the same statistical information for filtering the noisy process for Δk_t regions in the future (i.e. we only correlate the upper triangular elements of $\rho^{(MSE)}$ and δ_t). In order to see how the relationship evolves with increasing Δk_t, we use different markers: the dot is used for mapping the MSE degradation onto the SD values for $\Delta k_t \leq 5$ stationarity regions, the cross is used for $\Delta k_t \leq 10$ stationarity regions, the asterisk for $\Delta k_t \leq 100$ stationarity regions, and finally the circle considers the whole time span $\Delta k_t \leq K_t$.

It is a general observation that the scatter plot grows in both directions with increasing Δk_t. The farther we are from the actual k_t (i.e. large Δk_t), the more outdated is the statistical information used for filtering the process, and therefore, the larger is the MSE degradation. Similarly, the spectral distance increases due to the time evolution between the two compared LSFs, separated by Δk_t.

Comparing the scatter plots for the same direction with the opposite directions measurements, the latter reach larger values of MSE degradation and also SD. This is somehow expected since the changes of the power spectral density in a on-coming scenario (subfigure 4.2 (a)) are more prominent than in a convoy measurement (sub-

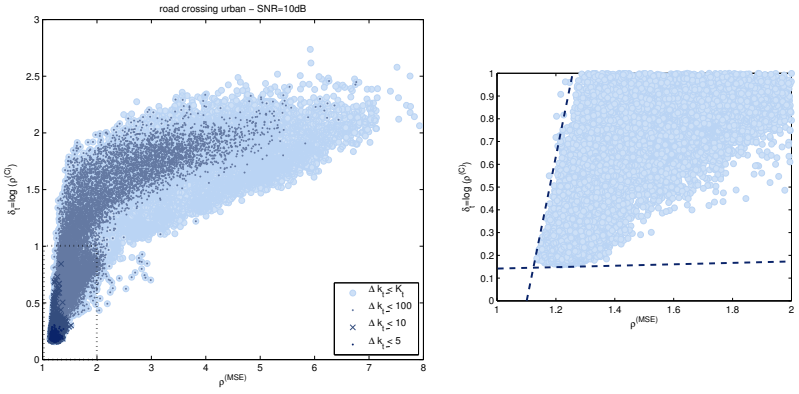

(a) Opposite directions in urban crossing measurement run

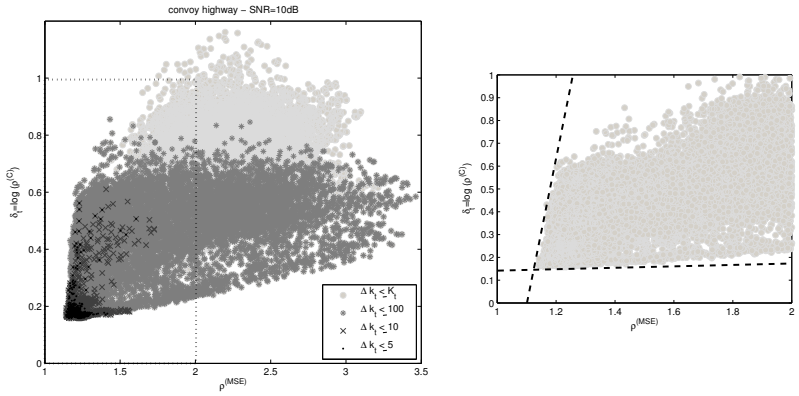

(b) Convoy in highway measurement run

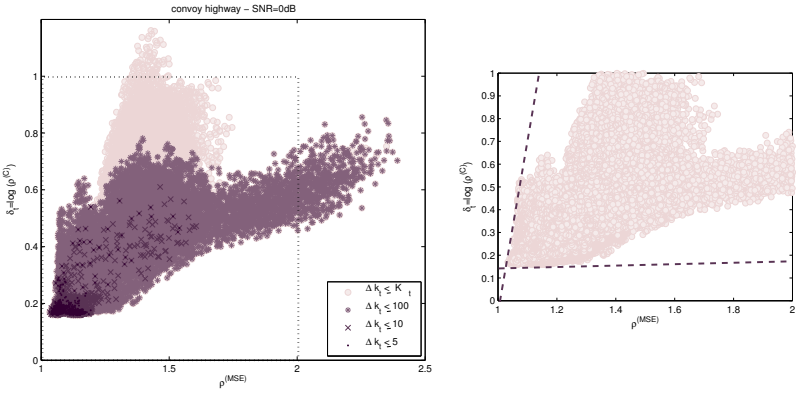

(c) Convoy in highway measurement run

Figure 4.2: Scatter plot showing the relationship between the MSE degradation and the SD outcome for two different scenarios and two different SNRs: Opposite directions in urban crossing measurement (a), convoy in highway measurement (b-c); SNR=10 dB (a-b), SNR=0 dB (c).

figures 4.2 (b-c)), the delay and the Doppler shift of the main component experience big changes within few seconds, in the opposite directions setting.

The MSE degradation $\rho^{(MSE)}$ is noise dependent, in contrast to the SD. By inspecting subfigures 4.2 (b) and (c), we observe the influence of the noise. When considering a system with less noise (SNR=10 dB), the MSE degradation is more sensitive to the use of outdated information. The filter coefficients can be estimated more accurately with less noise, and their validity becomes more restrictive too. Note that the MSE can be degraded up to 3.5 times the minimum reachable MSE for an SNR=10 dB, and up to 2 times for an SNR=0 dB. Moreover, if we consider, for instance, a $\rho^{(MSE)} = 2$ (i.e. a 2 times the minimum MSE), the SD needed under SNR=10 dB is 0.3, whereas for SNR=0 dB is 0.5. This points out the sensitivity of the SD to the noise, the SD values are larger in noisier conditions.

We try to devise a bound on the plots on the right hand side in Fig. 4.2. We indicate them with dashed lines. Whereas the lower horizontal bound, for minimum δ_t shows agreement among the three subplots, the left vertical bound, for minimum $\rho^{(MSE)}$ is strongly dependent on the amount of noise considered.

Even though it seems there is a bound, and therefore, a threshold for assessing stationarity could be found. We consider this approach too heuristic. Therefore, we suggest using the SD only for qualitatively assessing stationarity.

4.2.2 Empirical Results on the DRIVEWAY'09 Measurements

We select three representative measurements for discussion. We calculate the time-frequency varying LSF and apply the SD in time and in frequency as defined previously. The results are depicted in Fig. 4.3. The SD in time for all three measurements is shown in the left column, and the SD in frequency in the right column. Each one of the rows corresponds to one specific measurement: road crossing of two urban single lane streets (a-b), road crossing of two urban multiple lane streets (c-d), and an in-tunnel measurement (e-f). As discussed before, the elements in the diagonal correspond to a null shift, and as a result, the SD is zero. Moving away from the diagonal means increasing Δk_t or Δk_f.

We first have a look at the SD in time on the left column. We observe that the road crossing measurements reach higher values of divergence, in comparison to the in-tunnel measurement. The road crossing scenario can be seen as an opposite direction measurement. In that case, the main signal component in the delay-Doppler plane experiences an abrupt change within few seconds, when the TX and the RX pass each other (see Fig. 3.8 (c-d) in Chap. 3). In other words, the power spectra of the process changes rapidly and therefore, the Δk_t neighboring LSFs significantly differ

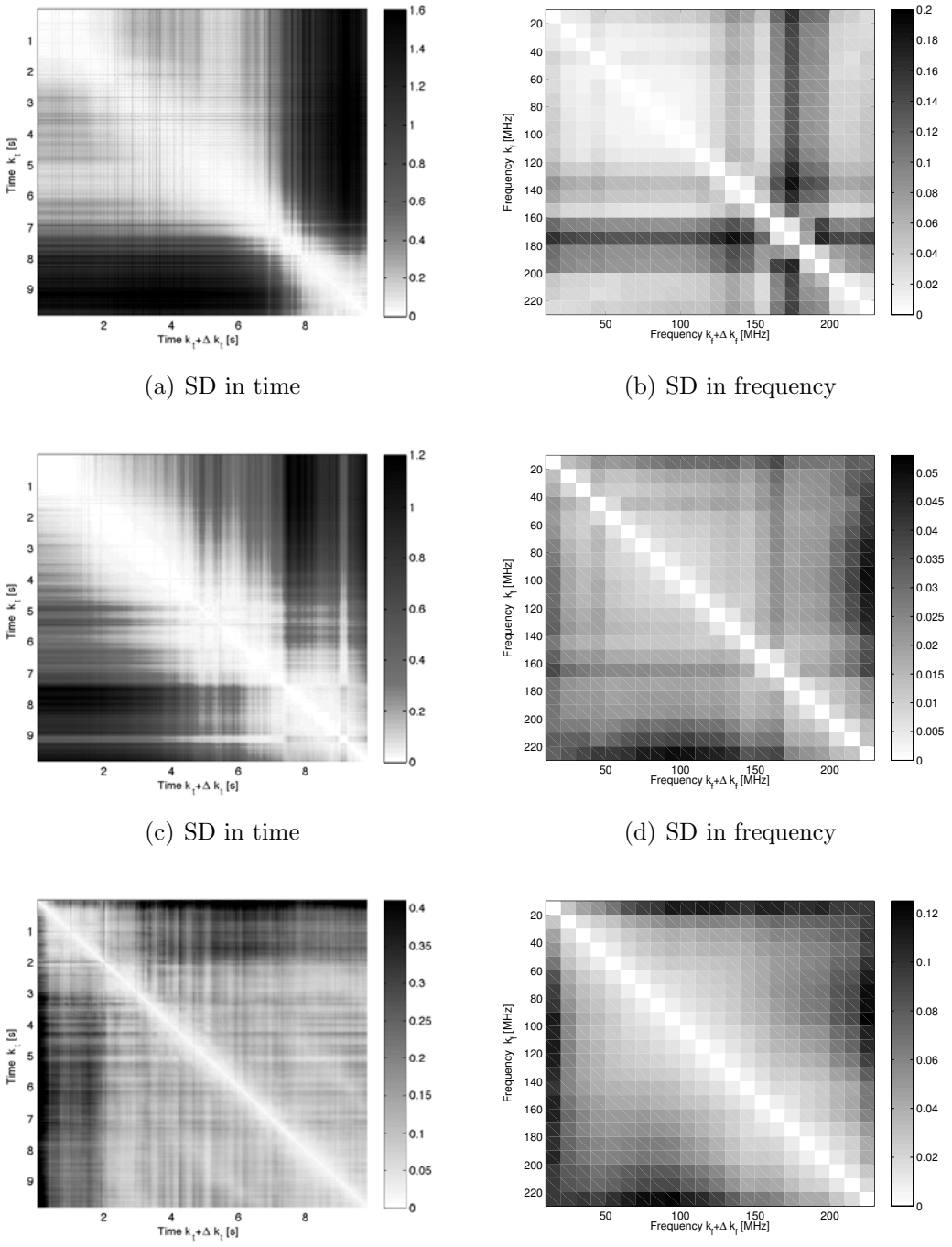

(a) SD in time

(b) SD in frequency

(c) SD in time

(d) SD in frequency

(e) SD in time

(f) SD in frequency

Figure 4.3: SD in time and frequency for two urban road crossings - single lane (a-b) and multiple lane (c-d) measurement, and in-tunnel (e-f) measurement, using $M = 64$, $N = 64$, $\Delta_t = 32$, and $\Delta_f = 32$.

from the LSF at k_t. For k_t corresponding to the drive-by period, the comparison of the current LSF with its neighboring LSFs leads to high divergence values. These values grow with increasing relative speed between the TX and the RX car. Hence, the maximum divergence in Fig. 4.3 (a) is higher than in (c), given that the cars in the single lane street crossing (a) were driving towards each other with higher speed than in the multiple lane crossing (c).

On the contrary, the divergence is low for measurements where the main component in the LSF remains more or less constant in delay and Doppler shift, as for the in-tunnel measurement in Fig. 4.3 (e).

Now, we concentrate on the right column in Fig. 4.3 showing the SD versus shifts in frequency. What first draws our attention is that the maximum divergences in frequency are always lower than in time. Besides that, they are more uniform, meaning that there are no abrupt changes as in the SD in time, except for the crossing of single lane streets (Fig. 4.3 (b)).

Summarizing, the SD in time relates to the WSS assumption, and the SD in frequency to the US assumption. Based on the results presented, we can say that the vehicular channel violates the WSS much stronger than the US assumption. However, we are not able to precisely assess the extent of the stationarity region in time and in frequency using the SD metric, because it is unbounded.

Therefore, we chose a bounded metric for further analysis.

4.3 A Bounded Spectral Distance Metric: the Collinearity

In [57], the correlation distance metric is used for characterizing stationarity and it is defined as 1 minus the cosine of the angle between two correlation matrices $\mathbf{R}_x$ and $\mathbf{R}_y$:

$$d_{corr} = 1 - \cos(\phi) = 1 - \frac{\mathrm{tr}\left\{\mathbf{R_x}\mathbf{R_y}\right\}}{\|\mathbf{R_x}\|_2 \|\mathbf{R_y}\|_2}, \tag{4.5}$$

where $\mathrm{tr}\{\cdot\}$ denotes the trace operator and $\|\cdot\|_2$ the L_2 norm.

The correlation distance metric can be interpreted as the measure of the overlap in the signal space between the two compared correlation matrices, i.e. it measures their orthogonality. The formulation as 1 minus $\cos(\phi)$ is meant as a correcting term such that the correlation matrix distance equals 0 when the correlation matrices are equal. On the other hand, when they are orthogonal, the distance equals 1.

In [59] the correlation distance metric is reformulated and applied to power spectral densities, directly related to the correlation function by means of the Fourier transform, see Fig. 3.1. The distance is renamed as *collinearity*, and consists of the cosine term in Eq.(4.5) only.

The collinearity is a bounded metric $\gamma \in [0, 1]$ that compares the LSF at different time instances and frequency regions. A collinearity close to 1 results from comparing very similar power spectra, whereas a collinearity close to 0 from comparing two very dis-similar spectral densities.

We differentiate between the collinearity in the time and in the frequency domain, in order to test the WSS and US assumptions separately. Hence, the collinearity in time is defined as

$$\gamma_t[k_t, k_t + \Delta k_t] = \frac{\sum_{n=0}^{N-1} \sum_{p=-M/2}^{M/2-1} \sum_{k_f=-N/2}^{N/2-1} \hat{\mathcal{C}}[k_t, k_f; n, p] \cdot \hat{\mathcal{C}}[k_t + \Delta k_t, k_f; n, p]}{\|\hat{\mathcal{C}}^{(k_t)}\|_2 \|\hat{\mathcal{C}}^{(k_t+\Delta k_t)}\|_2}. \tag{4.6}$$

The L_2 norm $\|\cdot\|_2$ operates on $\hat{\mathcal{C}}^{(k_t)}$, which is the vectorized LSF at a given time instant k_t, as

$$\|\hat{\mathcal{C}}^{(k_t)}\|_2 = \sqrt{\sum_{n=0}^{N-1} \sum_{p=-M/2}^{M/2-1} \sum_{k_f=-N/2}^{N/2-1} \hat{\mathcal{C}}[k_t, k_f; n, p] \cdot \hat{\mathcal{C}}^*[k_t, k_f; n, p]}, \tag{4.7}$$

with $(\cdot)^*$ denoting the complex conjugate operation. Analogously, the collinearity in frequency reads

$$\gamma_f[k_f, k_f + \Delta k_f] = \frac{\sum_{n=0}^{N-1} \sum_{p=-M/2}^{M/2-1} \sum_{k_t=-M/2}^{M/2-1} \hat{\mathcal{C}}[k_t, k_f; n, p] \cdot \hat{\mathcal{C}}[k_t, k_f + \Delta k_f; n, p]}{\|\hat{\mathcal{C}}^{(k_f)}\|_2 \|\hat{\mathcal{C}}^{(k_f+\Delta k_f)}\|_2}, \tag{4.8}$$

where now the L_2 norm operates on $\hat{\mathcal{C}}^{(k_f)}$, which is the vectorized LSF at a given center frequency k_f, as

$$\|\hat{\mathcal{C}}^{(k_f)}\|_2 = \sqrt{\sum_{n=0}^{N-1} \sum_{p=-M/2}^{M/2-1} \sum_{k_t=-M/2}^{M/2-1} \hat{\mathcal{C}}[k_t, k_f; n, p] \cdot \hat{\mathcal{C}}^*[k_t, k_f; n, p]}. \tag{4.9}$$

4.3.1 Stationarity Assessment using the Collinearity

Since the collinearity is a bounded metric, it allows us to set an indicative threshold, as a difference to the previous metric. This enables a WSS and a US test, and the definition of a time-frequency stationarity region.

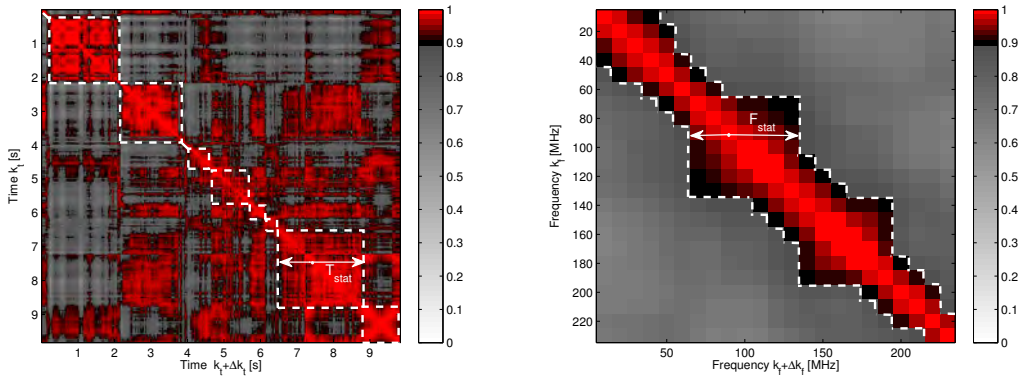

(a) Collinearity in time

(b) Collinearity in frequency

Figure 4.4: Collinearity in time and frequency for in-tunnel measurement, using $M = 64$, $N = 64$, $\Delta_t = 32$, and $\Delta_f = 32$.

We define the *stationarity time* T_{stat} and the *stationarity bandwidth* F_{stat}, as those time (or frequency) ranges where the collinearity exceeds a threshold α_{th}:

$$T_{\text{stat}}[k_t] = (M - \Delta_t)\, t_s + \Delta_t t_s \left(\sum_{\Delta k_t = 1 - k_t}^{\lfloor \frac{S-M}{\Delta_t} \rfloor - k_t} \alpha[k_t, k_t + \Delta k_t] \right), \tag{4.10}$$

and the stationarity bandwidth F_{stat} as

$$F_{\text{stat}}[k_f] = (N - \Delta_f)\, f_s + \Delta_f f_s \left(\sum_{\Delta k_f = 1 - k_f}^{\lfloor \frac{Q-N}{\Delta_f} \rfloor - k_f} \alpha[k_f, k_f + \Delta k_f] \right), \tag{4.11}$$

where $\alpha[k, k + \Delta k]$ is an indicator function defined as

$$\alpha[k, k + \Delta k] = \begin{cases} 1 & : \quad \gamma[k, k + \Delta k] > \alpha_{\text{th}} \\ 0 & : \quad \text{otherwise.} \end{cases} \tag{4.12}$$

In order to avoid overestimated T_{stat} values due to considering regions with only noise, only the time instances whose root mean square delay spread is greater than 0.5 ns are considered.

A graphical representation of how T_{stat} and F_{stat} are obtained from the collinearity can be seen in Fig. 4.4 for an in-tunnel measurement. We investigate values of $\alpha_{\text{th}} \in \{0.7, 0.8, 0.9\}$, the less restrictive the threshold is, the larger the stationarity time

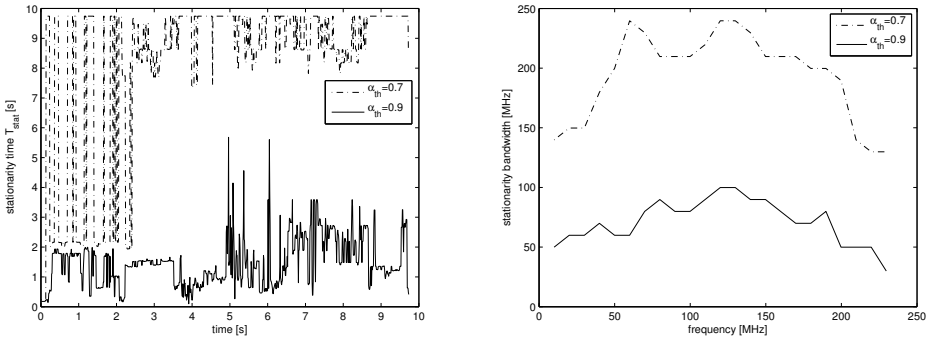

(a) Stationarity time (b) Stationarity bandwidth

Figure 4.5: Stationarity time and bandwidth for in-tunnel measurement for different α_{th}, using $M = 64$, $N = 64$, $\Delta_t = 32$, and $\Delta_f = 32$.

and the stationarity bandwidth are. We plot in Fig. 4.5 the time-varying stationarity time (a), and the frequency-varying stationarity bandwidth (b), for the in-tunnel measurement. We plot the results obtained with two different thresholds, $\alpha_{\text{th}} = 0.7$ and $\alpha_{\text{th}} = 0.9$. We found that reasonable values of T_{stat} are obtained for $\alpha_{\text{th}} = 0.9$, also used in [59]. We highlight the threshold $\alpha_{\text{th}} = 0.9$ using the color coding reported on the right hand side of each figure, and the resulting T_{stat} and F_{stat} with the dashed white line in Fig. 4.4.

4.3.2 Empirical Results on the DRIVEWAY'09 Measurements

We show in Fig. 4.6 the collinearity in time, subfigures (a), (c), and (e), and the collinearity in frequency, subfigures (b), (d), and (f). They are the results of the three representative measurement scenarios used in the previous section: road crossing of two urban single lane streets (a-b), road crossing of two urban multiple lane streets (c-d), and in-tunnel measurement (e-f). We highlight the threshold $\alpha_{\text{th}} = 0.9$ using the color coding reported on the right hand side of each figure.

By looking at these plots, one can already draw some conclusions regarding the stationarity time and bandwidths of these specific measurements. First, the red area (i.e. $\gamma \geq \alpha_{\text{th}}$) about the diagonal in the T_{stat} is smaller for the road crossing measurements (opposite directions), than for the in-tunnel (same direction). The region limiting the F_{stat} is large in the crossing of single lane streets (few scattering), and it decreases when considering the other two measurement scenarios (rich scattering).

The result of applying the aforementioned threshold to both collinearities is shown in Fig. 4.7. The stationarity time T_{stat} is plotted as a function of time in the subfigure

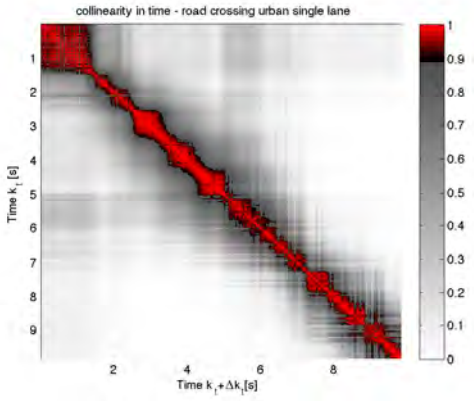

(a) Collinearity in time

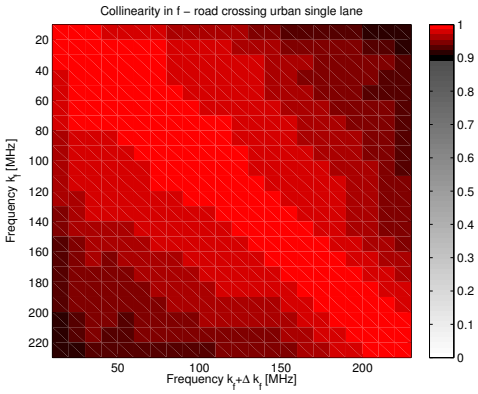

(b) Collinearity in frequency

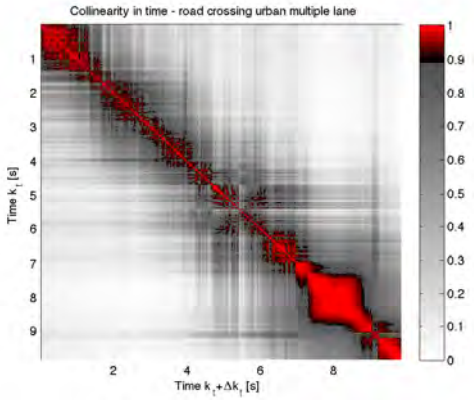

(c) Collinearity in time

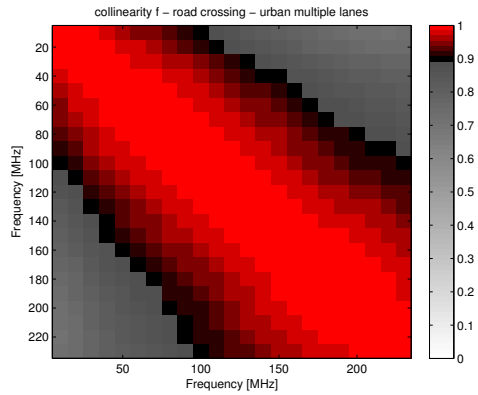

(d) Collinearity in frequency

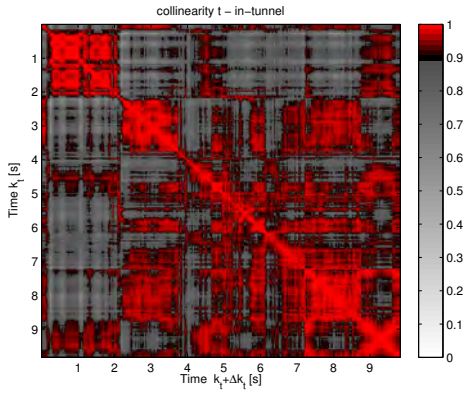

(e) Collinearity in time

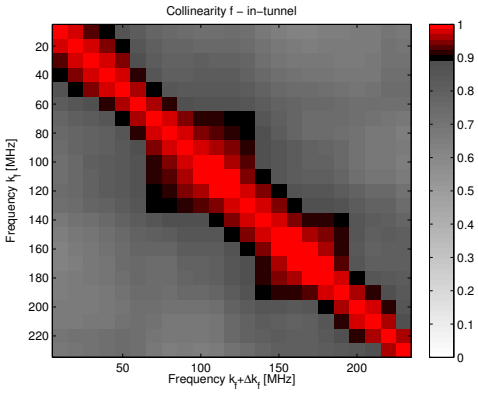

(f) Collinearity in frequency

Figure 4.6: Collinearity in time and frequency for two urban road crossings - single lane (a-b) and multiple lane (c-d) measurement, and in-tunnel (e-f) measurement,using $M = 64$, $N = 64$, $\Delta_t = 32$, and $\Delta_f = 32$.

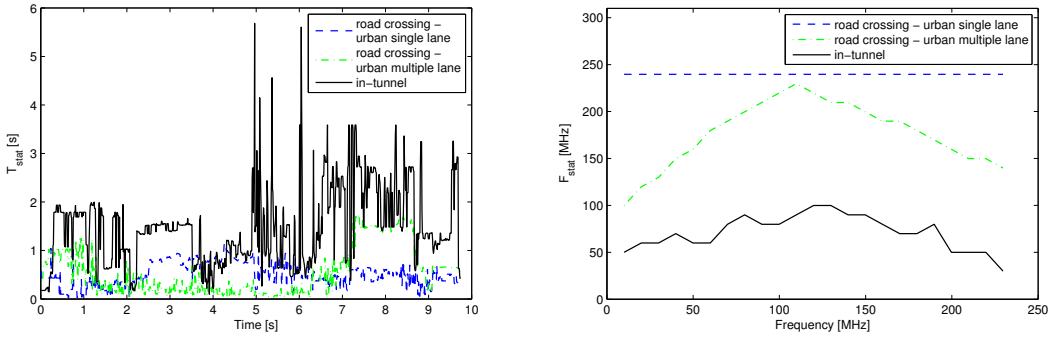

(a) Stationarity time

(b) Stationarity bandwidth

Figure 4.7: Collinearity in time and frequency for in-tunnel measurement.

4.4 (a). There, we observe a jittery T_{stat}. This is caused by the small number of samples in the time domain used for estimating the LSF in comparison to the total measurement time.

Nevertheless, we expect a smoother curve. The T_{stat} indicates for how long the fading process remains stationary in time, therefore we expect that the T_{stat} obtained for a given time instance is constant in time exactly for a T_{stat} period. For instance, in Fig. 4.7 (a), at 1 s for the in-tunnel measurement, the $T_{\text{stat}} = 1.8\,\text{s}$, which means that the process remains stationary for 1.8 s about the time 1 s. Based on that, we expect that all neighboring time instances within a period of length 1.8 s have a $T_{\text{stat}} = 1.8\,\text{s}$, i.e. we expect a flat line at 1.8 s. Noteworthy are the low values of T_{stat} observed in the crossing scenarios (dashed lines), below 1 s most of the time.

We plot the F_{stat} for the three illustrative measurements in Fig. 4.7 (b). They are smoother since the ratio between the stationarity region length in frequency and the total bandwidth is large enough. Here it is remarkable that the F_{stat} encompasses the whole measurement bandwidth for the *road crossing* in an urban single lane intersection measurement.

In the *road crossing* measurement, performed in an urban multiple lane intersection, and in the *in-tunnel* measurement, $F_{\text{stat}} < B$. It is noteworthy that in all the scenarios where the US property does not hold over the whole measurement bandwidth there is a rich scattering environment, as already noticed previously. Furthermore, we observe a decrease of F_{stat} at low and high frequencies. This is due to an edge effect, observed in the collinearity plot in Fig. 4.6 (d-f), due to the band limited measurements.

Moreover, we want to point out that there is no direct relationship between the

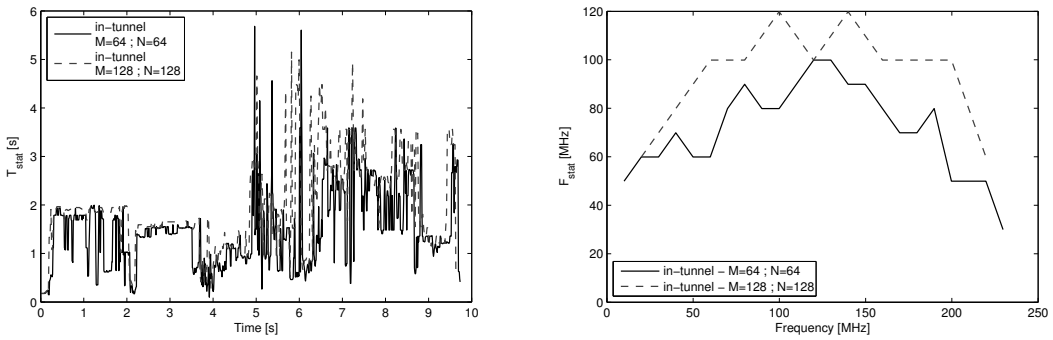

(a) Stationarity time

(b) Stationarity bandwidth

Figure 4.8: T_{stat} and F_{stat} for an *in-tunnel* measurement using two sizes for the *minimum stationarity region*.

violation of the stationarity in the time domain and in the frequency domain. For instance, a process can have a long stationarity time but small stationarity bandwidth, such as observed in the *road crossing* in an urban single lane intersection.

4.3.3 Definition of the Minimum Stationarity Region Dimensions

Until now, we have only shown results for single measurement runs in different scenarios. Nevertheless we have at our disposal the large set of DRIVEWAY'09 measurements. We next compute the minimum T_{stat} and F_{stat} for the overall measurement set, and how often these minima are obtained. These results can also be used to possibly enlarge the *minimum stationarity region*.

Table 4.1 lists, for each scenario (i) the minimum T_{stat} and F_{stat} (ii) the 5% outage probability, which indicates the dimension such that in 95% of all cases, the stationarity region is larger than this particular value, (iii) the mean, and (iv) the standard deviation of T_{stat} and F_{stat}.

We point out that the minimum T_{stat} in all scenarios is relatively low, confirming previous reports [60], [59], [66]. The smallest obtained stationarity bandwidth reaches the extension of the *minimum stationarity region*. From the values in Tab. 4.1, we find that the smallest stationarity bandwidth occurs in the *road crossing* in an urban intersection of multiple lane streets, *traffic congestion* with slow traffic, and *in-tunnel*. All of them with rich scattering environments, as mentioned before. For the *in-tunnel* measurements, the fact that the reflections on the walls and ceiling cause multiple components stemming from the same scatterer at different delays, offers a physical explanation of the violation of the US condition.

We note that the standard deviation of F_{stat} for the *merging lanes* scenario in rural environment is 0 MHz, in all 7 measurement runs. The apparently stable result, $F_{\text{stat}} = B$, is due to the limited measurement bandwidth B.

We observe that the mean stationarity bandwidths of all measurements except for the *in-tunnel* measurement are above 150 MHz. This is very much larger than the required communication bandwidth of an IEEE 802.11p system, standard dedicated to vehicular communications.

Based on the results above, the size of the minimum stationarity region (window used for analysis) can be doubled, yielding better resolution. We show the T_{stat} and the F_{stat} for the *in-tunnel* measurement in Fig. 4.8 (a) and (b) in gray dashed line using the doubled stationarity region dimension, and compare it to the initial choice in black solid line.

Table 4.1: Minimum observed stationarity time T_{stat} and stationarity bandwidth F_{stat} using $M = 64 = 19.66\,\text{ms}$ and $N = 64 = 19.97\,\text{Hz}$

Stationarity region dimensions		T_{stat}	F_{stat}
Road crossing - suburban with traffic (3 measurements)	min:	29.49 ms	189.76 MHz
	5% out:	69.69 ms	229.76 MHz
	mean:	1.38 s	237.69 MHz
	std:	0.91 s	8.71 MHz
Road crossing - suburban without traffic (11 measurements)	min:	49.15 ms	59.93 MHz
	5% out:	266.04 ms	199.69 MHz
	mean:	1.75 s	232.94 MHz
	std:	0.92 s	25.55 MHz
Road crossing - urban single lane (5 measurements)	min:	19.66 ms	159.80 MHz
	5% out:	98.67 ms	219.76 MHz
	mean:	0.49 s	236.91 MHz
	std:	0.25 s	10.46 MHz
Road crossing - urban multiple lane (5 measurements)	min:	29.49 ms	29.96 MHz
	5% out:	77.77 ms	50.00 MHz
	mean:	0.61 s	159.01 MHz
	std:	0.47 s	62.69 MHz
General LOS obstruction - Highway (12 measurements)	min:	19.66 ms	39.95 MHz
	5% out:	196.99 ms	69.81 MHz
	mean:	2.16 s	199.96 MHz
	std:	1.12 s	62.73 MHz
Merging lanes - rural (7 measurements)	min:	19.66 ms	$\geq$ 239.69 MHz
	5% out:	509.93 ms	$\geq$ 239.69 MHz
	mean:	2.59 s	$\geq$ 239.69 MHz
	std:	0.81 s	$\geq$ 0 MHz
Traffic congestion - slow traffic (11 measurements)	min:	39.32 ms	29.96 MHz
	5% out:	245.09 ms	79.98 MHz
	mean:	1.71 s	174.80 MHz
	std:	0.99 s	65.52 MHz
Traffic congestion - approaching traffic jam (7 measurements)	min:	68.81 ms	59.93 MHz
	5% out:	225.63 ms	109.81 MHz
	mean:	1.79 s	215.00 MHz
	std:	10.7 s	46.60 MHz
In-tunnel (7 measurements)	min:	29.49 ms	19.97 MHz
	5% out:	167.62 ms	39.92 MHz
	mean:	1.06 s	80.34 MHz
	std:	0.93 s	39.53 MHz
On-bridge (4 measurements)	min:	19.66 ms	109.86 MHz
	5% out:	924.19 ms	129.79 MHz
	mean:	2.64 s	221.67 MHz
	std:	0.68 s	35.48 MHz

5 Time-varying Stochastic Characterization of the Vehicular Channel

In order to describe the radio channel in a deterministic manner, detailed information about the propagation environment is needed. Radio channels of practical interest aim at describing the wave propagation behavior in complex environments. The number of required detailed information about the environment is large, and therefore, it is not feasible to describe the CIR deterministically for complex channels. Therefore, the statistical representation of the channel is widely used (see Chap. 3). In this chapter we characterize the vehicular radio channel based on the data collected in the DRIVEWAY'09 measurement campaign (described in Chap. 2).

In the previous chapter we showed that the fading process in the vehicular radio channel is neither WSS nor US, which determines a time and frequency dependence of the statistical description that we aim to perform. Nevertheless, the violation of the stationarity is much stronger in the time domain than in frequency, we recall here that non-US is not observable within the 10 MHz bandwidth (of an IEEE 802.11p system). However, violations of the WSS assumption are relevant because the frame duration may exceed the stationarity time, or each frame is affected by different statistical properties of the channel.

Therefore, in this chapter we focus on the characterization of the non-WSS description of the channel parameters, and we assume the US property to hold for the whole measurement bandwidth. With that, we gain in resolution in the delay domain for our investigations, for which we use $M = 128$, $N = 769$, $\Delta_t = 0$, $\Delta_f = 0$.

We investigate the time-varying stochastic characterization of the radio channel. This chapter is divided into three sections covering the first order moment description of the fading process (the K-factor), the second order moment description (RMS delay and Doppler spreads), and finally a time-varying geometry-based stochastic power spectral characterization (relevant scattering objects).

In this chapter the concepts of *path*, *multipath component* (MPC), and *cluster* are used often. In order to make a clear differentiation among them, we define them

here. The propagation *path* is defined by each individual ray transmitted from the TX to the RX, either directly or through reflections. Waves arriving at the same delay superimpose giving raise to a *multipath component* (MPC). MPCs stemming from the same scatterer can be grouped in *clusters*, and they present correlated large-scale fading [88].

5.1 Time-, Frequency-, Space-varying K-factor

In wireless communication systems, small-scale fading statistics have a large impact on the performance of a communication link, such as bit error rate (BER), capacity, and RX design among others. It is a common approach in wireless communication systems to describe the distribution of the amplitude of the channel coefficient with a single parameter. The received signal consists of the sum of specular components and diffuse components. Often, the specular component consists only of the LOS component, but they also stem from flat good reflecting surfaces (e.g. a traffic sign), where the impinging wave is reflected into a single direction. A Ricean distribution can be defined in terms of a parameter called K-factor [89]. The K-factor is defined as the ratio of the energy of the specular and the diffuse part of the signal as $K[dB] = 10\log_{10}(r^2/2\sigma^2)$, and it is an indicator of the severity of the fading. A K-factor value close to 0 in linear scale indicates strong fading (Rayleigh distribution), and a large K-factor value in linear scale is related to less variations (Ricean distribution).

For testing and simulation purposes, the assumption of a constant K-factor is widely used. However, in mobile communications there are several factors that could introduce variability to the K-factor. Therefore, we propose to extend the small-scale fading model by a time-/frequency-/space-varying K-factor to make the model comply with large-scale statistics.

5.1.1 K-factor Estimation

The IEEE 802.11p standard dedicated to vehicular communications defines a carrier frequency of 5.9 GHz in a 10 MHz bandwidth for an OFDM modulation scheme. In order to be able to perform a meaningful small-scale fading analysis using the DRIVEWAY'09 data, we have to split the measurements. If the whole 240 MHz bandwidth we would be able to resolve many paths, thus eliminating their superposition needed for the statistical analysis of the small-scale fading. Therefore, we split the 240 MHz measured bandwidth into $Q = 24$ frequency sub-bands with 10 MHz each. This allows for a frequency-dependent investigation too. Furthermore, we consider the 4×4 MIMO measurements as $L = 16$ SISO directional channels, in order to

Table 5.1: Parameters for measurement and for K-factor analysis

Parameters	Measurement	K-factor Analysis
Channels:	4×4 MIMO	16 SISO
Carrier frequency:	5.6 GHz	5.6 GHz
Measurement bandwidth:	240 MHz	24×10 MHz
Snapshot repetition time:	307.2 μs	307.2 μs
Recording time:	10 s	10 s

add the directional analysis. Table 5.1 summarizes the DRIVEWAY'09 measurement parameters and the chosen parameters for the small-scale fading investigation.

The selected parameters provide K-factor results for 16 different directional channels, each channel contains 24 different 10 MHz frequency sub-bands. Each sub-band is measured for a time duration of 10 s (or 20 s, depending on the measurement run). With these available data we can conduct a multi-dimensional space-frequency-time K-factor analysis.

Data preprocessing

In order to perform the small-scale fading analysis of the measured data on a per delay bin basis, we need to carry out some preprocessing, which consists of two steps:

1. Search for the delay bins corresponding to the first strong MPC in the CIR, and shift them to the origin. This is done on a per link, per frequency sub-band, and per time instance basis.

2. Remove the large-scale fading from the measured data by applying a moving average filter of length S_{LS} samples in the time domain. We assume the large-scale fading to be stationary during $S_{LS} samples$ [90], [91]. The large-scale fading changes slower than the small-scale fading effects, as a result, the averaging window S_{LS} has to be considered at least as large as the number of samples used later for the K-factor estimation. This is why we set $S_{LS} = S_K + 100$, where S_K denotes the length of the observation window used for K-factor estimation.

   The CIR without large-scale fading is calculated as

$$h_{noLS}[m, n; q, l] = \frac{h[m, n; q, l]}{\sqrt{\varepsilon_h[m, n; q, l]}}, \tag{5.1}$$

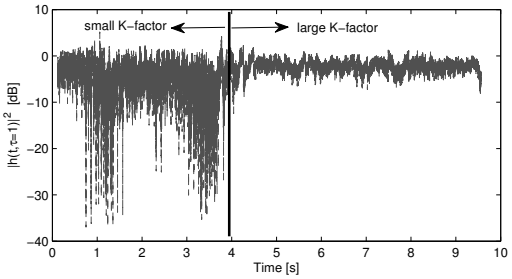

Figure 5.1: Magnitude square of the envelope of the CIR of the first delay bin without large-scale fading.

where $\varepsilon[m, n; q, l]$ is the average power calculated as

$$\varepsilon_h[m, n; q, l] = \frac{1}{S_{LS}} \sum_{m'=m-S_{LS}/2}^{m+S_{LS}/2-1} \sum_{n'=1}^{N-1} |h[m', n'; q, l]|^2 . \tag{5.2}$$

The initially measured CIR per link $l \in \{1 \dots L-1\}$, and frequency sub-band $q \in \{1 \dots Q-1\}$ is denoted in Eq. (5.1) and Eq. (5.2) as $h[m, n; q, l]$. The variable representing the global time is $m \in \{1 \dots S-1\}$, the local time used to calculate the average power is $m' \in \{m \dots m + S_{LS} - 1\}$, and the delay bin index is given by $n \in \{1 \dots N-1\}$, with $N = 33$.

By selecting the right filter length we center the envelope of a strong and single delay component to $\mid h_{noLS}[m, n; q, l] \mid = 1$ with a certain variance. Figure 5.1 shows the envelope of the CIR without large-scale fading over time for the first delay bin for link $l = 10$ and sub-band $q = 1$, which corresponds to $f = 5480\,\text{MHz}$. From this picture we can visually predict at which time instances the K-factor will be low and high, corresponding to periods where the variance of the envelope is large or small, respectively.

For conducting a first analysis of the K-factor, we use the *GLO-h* scenario as an illustrative measurement, see Fig. 5.2. The TX and RX are driving in the same direction on the highway at around 120 km/h (33.33 m/s) each, with big trucks driving in both directions beside them, and sometimes obstructing the LOS between the TX and the RX cars.

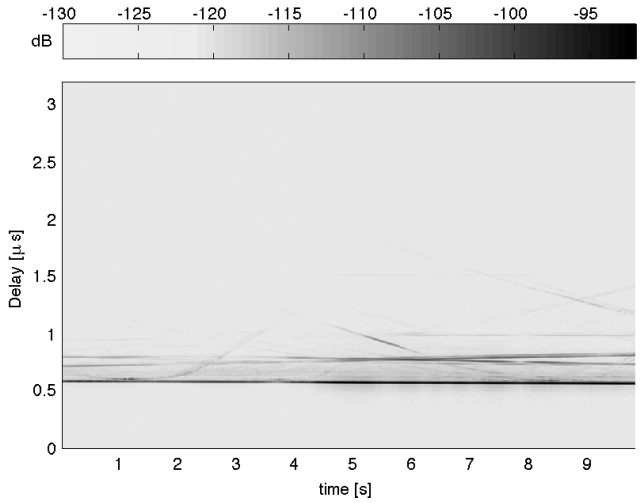

Figure 5.2: Time-varying PDP for a *GLO-h* scenario: convoy measurement with temporally obstructed LOS, constant velocities of 120 km/h (33.33 m/s).

K-factor estimation

We first have a look at the per-delay-bin small-scale fading distribution of the data without large-scale fading effects. To do that, we select a link l, a frequency sub-band q, and a time instance m.

We estimate the K-factor by using the method of moments (MoM) [92] that provides us with a first guess of the K-factor. Then we apply a least-squares fit of the Rice distribution curve to the data histogram so that the MSE between the empirical and the analytical CDF is minimized.

We have tried out several sample lengths and corroborated that the MoM and MSE fit estimators deliver very similar results when considering an assemble larger than 1000 samples. However, these results only hold when the underlying distribution of the data is truly Ricean, which is the assumption of the MoM method. Nevertheless, this assumption might not always hold true. If the underlying distribution is indeed Ricean, the MoM estimator outperforms the MSE fit estimator for a small number of samples. In contrast, for a large number of samples, the MSE fit estimator provides a good fit of a Ricean distribution of the underlying data [93]. Furthermore, the MoM estimator fits the first and second order moments of the data in order to derive the K-factor, with the MSE fit estimator, the shape of the Ricean distribution is fitted to the actual data. A detailed analysis on the choice of S_K is done in the next paragraph.

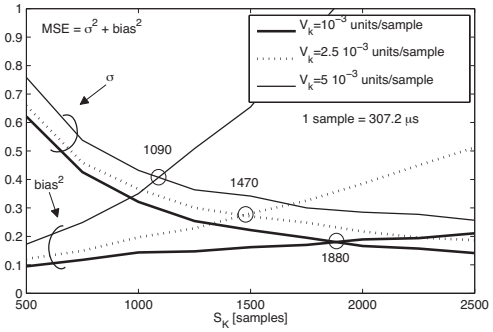

Figure 5.3: Bias^2 and variance of the K-factor estimator for three K-factor variation velocities.

$\mathbf{S_K}$ Sample size selection

In order to select the sample size S_K used for the estimation of the K-factor, we have to take several aspects into account. First, the observation period can not exceed the stationarity length of the process. Second, a large number of samples has to be used in order to obtain meaningful statistical results. And finally, S_K has to be smaller than S_{LS}, i.e. the number of samples used for removing large-scale fading effects.

We analyzed the performance of the MSE fit estimator for different sample sizes S_K in terms of variance and bias through Monte-Carlo simulations with 5000 realizations. We generate Ricean distributed channels analytically with a K-factor of 10, and add white Gaussian noise such that the resulting SNR is 25 dB. We assume that the K-factor changes linearly in time as $K(t) = K_0 + \Delta_K t$, with an initial K-factor $K_0 = 10$ and a variation Δ_K. Therefore, we test the estimator for three different Δ_K: 10^{-3}, $2.5 \cdot 10^{-3}$, and $5 \cdot 10^{-3}$ units/sample. The samples are defined in the time domain and have a duration of $t_s = 307.2\,\mu$s.

Figure 5.3 shows the

$$\text{bias}^2 = \left(\frac{1}{S} \sum_{t=1}^{S-1} E\{\hat{K}(t) - K(t)\} \right)^2, \tag{5.3}$$

and the variance

$$\sigma^2 = \frac{1}{S-1} \sum_{t=1}^{S-1} E\{(\hat{K}(t) - E\{K(t)\})^2\} \tag{5.4}$$

of the estimator for the different Δ_K. In Eqs. (5.3) and (5.4), $E\{\cdot\}$ denotes the statistical expectation over the 5000 realizations, after which we perform a temporal mean

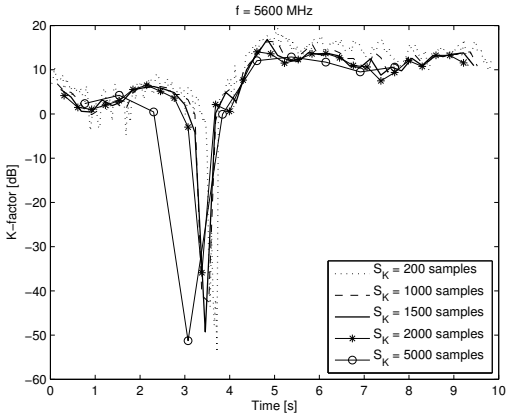

Figure 5.4: Time-varying K-factor for the first delay bin estimated with different sample size lengths S_K at $f = 5600$ MHz using a *GLO-h* measurement.

calculation, in order to get rid of the time-dependency. The intersection between the bias^2 and the variance curves sets the point at which the MSE is minimum, which is highlighted with a circle for the three cases.

In Fig. 5.3 we can observe the effects of the two important aspects we mentioned before. The sample length S_K achieving the minimum MSE decreases as the K-factor rate of change increases. This also corroborates that the stationarity time is dependent on the K-factor changes. Further, we observe that the minimum MSE increases when short window lengths S_K are considered, i.e. the number of used samples for estimation is not sufficient to obtain a trustful estimate.

Based on these conclusions, we select a sample size of 1500 snapshots. With that, we assume that the process remains stationary within 0.46 s. We cross-check this result by estimating the K-factor on measurements using different S_K, namely 200, 500, 1000, 1500, 2000, and 5000 samples. We show the results in Fig. 5.4. The estimated K-factor for $S_K < 2000$ show similar results. However, the smaller S_K is, the more variance it has. On the other hand, for $S_K = 5000$, the results are not accurate anymore, and moreover we can not firmly assure that we are not violating the WSS assumption. With that, we corroborate that setting $S_K = 1500$ is reasonable. For the chosen example, *GLO-h*, this corresponds to a travelled distance of $240\,\lambda$. Using $S_K = 1500$ for all scenarios we cover traveled distances from $50\,\lambda$ (for urban environments) to $250\,\lambda$ (for *highway* measurements).

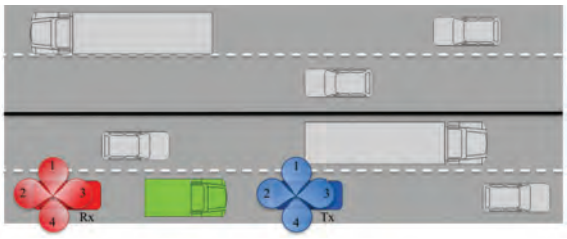

Figure 5.5: Scenario layout - *GLO-h*. In blue the TX car, in red the RX car. The green truck is the element intermittently obstructing the LOS during the measurement. Refer to Tab. 5.2 to see the link to antenna mapping.

Envelope distribution per tap investigation

Figure 5.6 (a), (b), and (c) show the CDF of the first five delay bins of $\mid h_{noLS}[m, n; q, l] \mid$. The measured data is represented by a solid line and the fitted CDF using a dashed line. Results are shown for link $l = 10$, frequency sub-band $q = 12$, corresponding to a frequency of 5600 MHz, at time instances 0.2 s, 4.8 s, and 9.5 s respectively. At 0.2 s the LOS between TX and RX is obstructed, therefore the distribution of the first tap is closer to being Rayleigh (note the shift towards the left hand side of the plot). At 4.8 s, the truck blocking the LOS has moved to another lane allowing a LOS communication. As a result, the K-factor of the first delay bin increases and its CDF is shifted to the right in Fig. 5.6 (b). The same effect can be noticed at 9.5 s.

Furthermore, we observe that delay bins 2-5 follow a Rayleigh distribution throughout all time instances. On the other hand, the first delay bin appears to be clearly Ricean distributed with a varying K-factor for the three different time instances, $K_{t=0.2\,s} = 5.59\,\text{dB}$, $K_{t=4.8\,s} = 13.46\,\text{dB}$, and $K_{t=9.5\,s} = 10.92\,\text{dB}$.

5.1.2 Empirical Results

We want to investigate the temporal, spatial (link-wise), and frequency dependency of the K-factor. For that we focus on the first delay bin. The time and frequency analysis is focused on link $l = 10$, TX element 3 to RX element 3. The radiation

Table 5.2: Links and corresponding TX -RX antenna pairs

Link	1	2	3	4	5	6	7	8	9	10	11	12	13	14	15	16
TX ant.	1	1	1	1	2	2	2	2	3	3	3	3	4	4	4	4
RX ant.	4	3	2	1	4	3	2	1	4	3	2	1	4	3	2	1

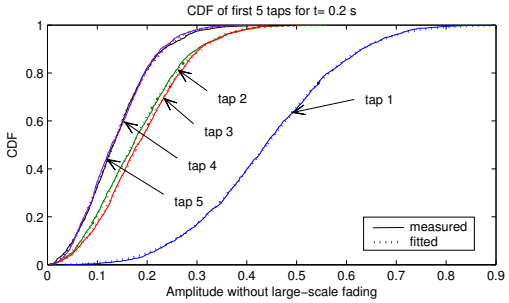

(a) CDF for 1-5 delay bins for link 10 and sub-band 12 (5600 MHz) at $t = 0.2$ s.

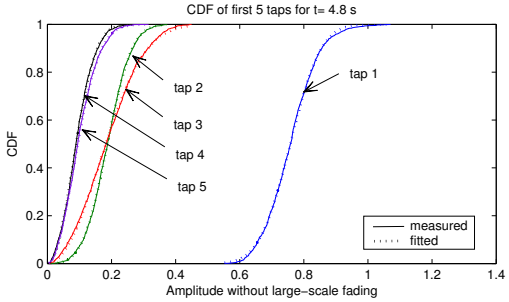

(b) CDF for 1-5 delay bins for link 10 and sub-band 12 (5600 MHz) at $t = 4.8$ s.

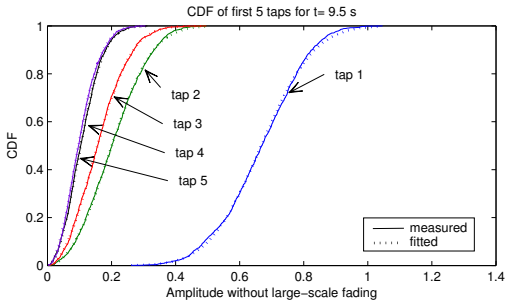

(c) CDF for 1-5 delay bins for link 10 and sub-band 12 (5600 MHz) at $t = 9.5$ s.

Figure 5.6: Empirical and fitted CDF for 1-5 delay bins for link 10 and sub-band 12 (5600 MHz), using a sample size of 1500 samples. *GLO-h*.

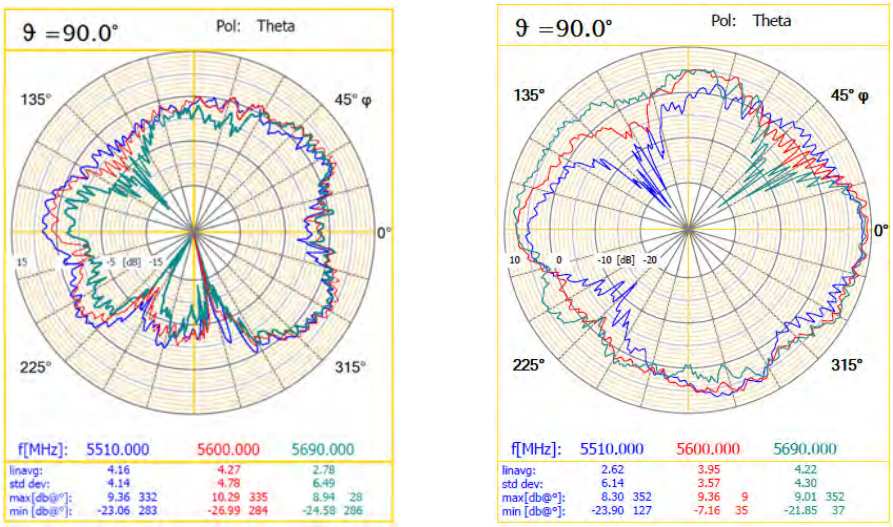

(a) TX antenna 3. (b) RX antenna 3.

Figure 5.7: Radiation pattern of antenna element 3, $\varphi = 0°$ shows the driving direction [3].

pattern of the corresponding antenna elements 3 are shown in Fig. 5.7. Figure 5.5 shows an schematic view of the orientation of the radiation patterns for the TX and the RX, and Tab. 5.2 shows the mapping between the links and the antenna elements.

Figure 5.8 shows a 3D representation of the K-factor for the first delay bin of link $l = 10$ next to its corresponding time-frequency power. We observe an evolution of

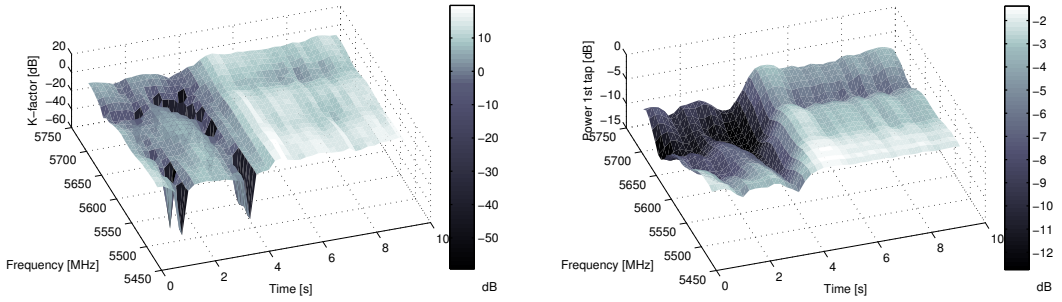

(a) Time-frequency dependent K-factor. (b) Time-frequency dependent power.

Figure 5.8: Time-frequency dependent K-factor and power for tap 1 of link 10. *GLOh.*

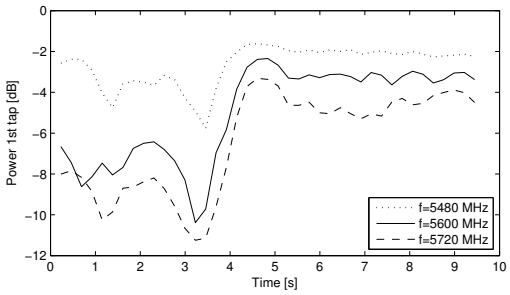

(a) Time-varying power of the first tap

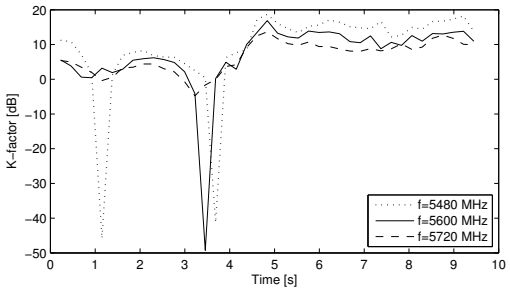

(b) Time-varying K-factor of the first tap

Figure 5.9: Time-varying K-factor and power of the first delay tap without large-scale fading for link 10 and three different frequency sub-bands for a sample size of 1500. *GLO-h*.

the K-factor and the normalized power in both domains, frequency and time.

On what follows, we discuss the time, the frequency, and the space variability of the K-factor of the first delay bin independently. We remind here that the chosen illustrative measurement corresponds to a *GLO-h* scenario. During the studied measurement run, the TX and the RX cars experience obstructed LOS until approximately 5 s, afterwards, the truck blocking the LOS moves away.

5.1.2.1 Time-Varying K-factor

We show the time evolution of the K-factor and received power for three different frequency sub-bands in Fig. 5.9. Although the K-factors do not present the same value, they exhibit the same tendency.

There is not necessarily a correspondence between received power and K-factor (look at the scale in the figures). Large K-factors up to 20 dB are observed between 5 and 10 s. However, the estimated K-factor is around 10 dB smaller from 0 to 5 s, although the received power is not negligible. In that case, there are more significant

diffuse components in the received signal and thus it is better described by a lower K-factor. Noteworthy is that the estimated K-factors for the obstructed LOS region are relatively high, most of the time above 5 dB.

5.1.2.2 Frequency-Varying K-factor

We analyze now the frequency-varying behavior of the K-factor. For that, we select three different time instances for link $l = 10$. We plot their K-factor as a function of the 24 frequency sub-bands in Fig. 5.10 (a), together with the power for the first tap, in Fig. 5.10 (b). One should not necessarily assume the same small-scale fading statistics characteristics throughout a range of 240 MHz.

We observe different small-scale fading statistics in the 24 different frequency sub-bands, with variations up to 14 dB. One reason for this frequency variation on the K-factor is the frequency dependent antenna pattern gains within the 240 MHz measurement bandwidth. As it can be observed in Fig. 5.7, the radiation pattern of elements TX3 and RX3 changes significantly at the lower, central, and upper band. This effect is mainly observed for TX element 3, where the gain experiences

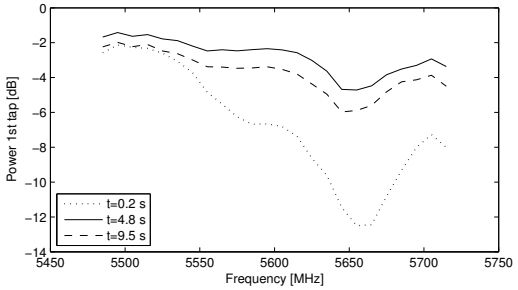

(a) Frequency-varying power of the first tap

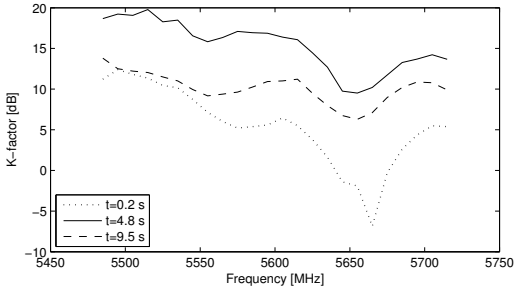

(b) Frequency-varying K-factor of the first tap

Figure 5.10: Frequency-varying per sub-band K-factor and power of the first delay tap without large-scale fading for link 10 and three different time instances. *GLO-h.*

a variation of 10 dB at the bandwidth edges with respect to the carrier frequency. Even though they do not lose the directionality, there are certain regions where deep dips appear, such as at 50°, and 280° for the TX3. For the RX3, the variations in frequency of the radiation pattern are not as severe as for the TX3.

The large-scale behavior of the K-factor does not normally change within a narrow-band frequency bandwidth. In our case, the relative bandwidth of two consecutive frequency sub-bands, i.e. 20 MHz, is less than 10%. Therefore it is remarkable the strong frequency variation of the K-factor already from sub-band to sub-band.

5.1.2.3 Narrow-band K-factor

We observed a frequency dependability of the K-factor in the analysis performed in the latter subsection. This is why we investigate here the K-factor in the frequency domain in a per frequency bin basis. Since the IEEE 802.11p standard is OFDM based, this frequency variability will have an influence on the communication system performance per sub-carrier. Therefore, we look now into the time-frequency variation of the narrow-band K-factor.

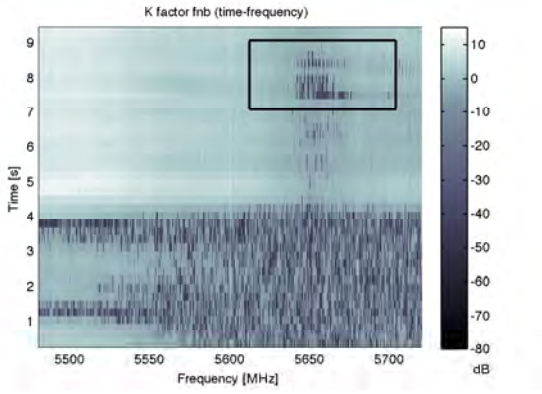

(a) Narrowband K-factor for link 10.

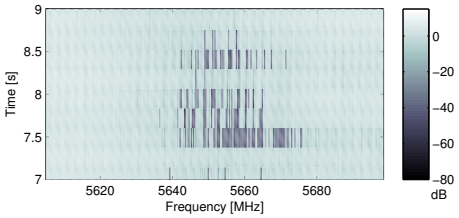

(b) Narrowband K-factor for link 10.

Figure 5.11: Narrowband K-factor for link 10. *GLO-h*.

We proceed with the estimation of the K-factor in the frequency domain instead of in the delay domain, done in the previous section. Now, we do not separate the frequencies in sub-bands. The K-factor is estimated per frequency bin for the whole bandwidth of 240 MHz with a frequency resolution of $\Delta f = 312$ kHz and using a sample size of $S_K = 1500$ snapshots, as well.

The upper plot in Fig. 5.11 shows a 2D representation of the time-frequency dependence of the K-factor for link $l = 10$. Here, the obstructed LOS region (until 5 s) is also noticeable, showing low K-factor values.

In the narrow-band analysis we can also appreciate the frequency variation of the K-factor, mainly due to the strong variations of the antenna gain throughout the measurement bandwidth.

On the bottom of Fig. 5.11 we see an enlarged portion of the upper plot, namely the one surrounded by the black square. As mentioned before, the IEEE 802.11p standard is OFDM based, thus it is important to look at the fading affecting the individual subcarriers. In Fig. 5.11 (b) we observe the narrow-band K-factor variation within 10 consecutive 10 MHz frequency sub-bands. Important is that the frequency variation is also observed already within one sub-band.

5.1.2.4 Space-Varying K-factor

The K-factor is also different depending on the selected link between TX and RX antennas because we used directional antennas. We consider 4 of the 16 measured SISO channels, namely links 4, 6, 10, 13, see Tab. 5.2 and Fig. 5.5. Link 4 corresponds to the link between the two antenna elements radiating towards the left side of the road with respect to the driving direction. They include contributions coming mainly from this direction. Similarly, link 13 collects contributions from the right side of the road, with respect to the driving direction. Link 10 is defined between the antennas of the TX and RX which are radiating to the front, to the driving direction. Finally, link 6 corresponds to the pair of antennas facing each other, i.e. front-back, see Fig. 5.5. Figure 5.12 shows the time-frequency dependent K-factor for the four described links.

Due to the orientation of the antenna radiation patterns and the position of scatterers on the road, the time-frequency variation of the K-factor is different depending on the considered link. It is reasonable that the K-factors obtained for link 6 are the highest, since the two antennas of the link are facing each other. The links facing the sides of the road show K-factors 10 dB lower than the others in LOS situation. Furthermore, the K-factors for these links are more often below 0 dB, which indicates they are experiencing non-LOS condition instead of just obstructed LOS.

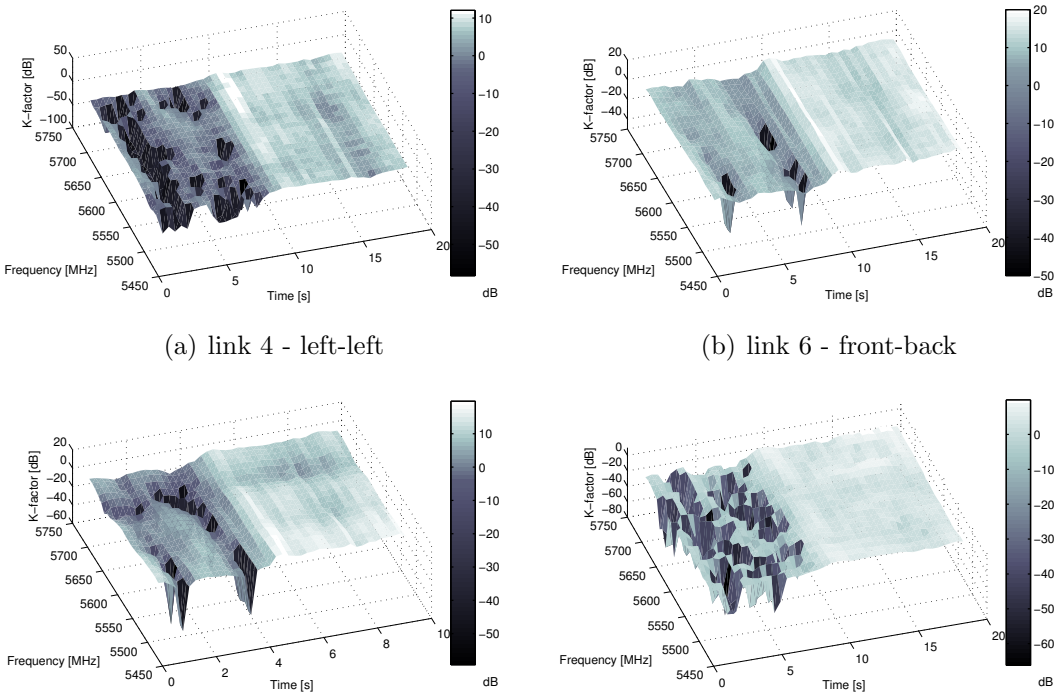

(a) link 4 - left-left

(b) link 6 - front-back

(c) link 10 - front-front

(d) link 13 - right-right

Figure 5.12: Time-frequency dependent K-factor for four different links. *GLO-h*.

Nevertheless, in all links, the regions with obstructed LOS and pure LOS are clearly identifiable.

Based on these results, one can conclude that a K-factor observed during an obstructed LOS situation depends mainly on the obstruction that the link is suffering.

5.1.2.5 Statistical Modeling

We are interested in characterizing the distribution of the K-factor. We need to account for the time variability of the parameter, for the frequency variation, and for the directional dependency.

For this characterization we chose a single link, namely link $l = 10$, where the antennas of the two cars are radiating towards its driving direction. In order to see whether we can use the whole data ensemble of the link for the statistical characterization, we first have a look at the CDFs of the 24 frequency sub-bands individually, plotted in Fig. 5.13 in blue thin line. On top of them, we add the mean CDF of all frequency sub-bands in red thick line. By looking at them, we conclude that they are described by the same distribution. Therefore we use the estimated K-factors in

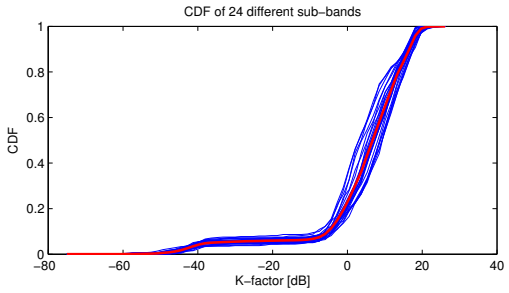

Figure 5.13: CDF per sub-band - frequency dependent K-factor for link 10 (front-front). *GLO-h*.

all sub-bands jointly for fitting purposes.

We use bi-modal Gaussian distribution for the fitting. One of the the Gaussian functions describes the LOS situation (large K-factors), the other one describes the non-LOS (small K-factors). The weighting factors of the two Gaussians indicate the probability of having LOS or non-LOS for a particular scenario. We plot in Fig. 5.14 the CDF of the estimated K-factor in solid line, and the fitted CDF in dashed line. We apply the Kolmogorov-Smirnov (KS) test as a goodness of fit (GoF) indicator. We consider we achieved a good fit if the outcome of a KS-test is below ϵ, which indicates that the maximum distance between empirical and fitted CDF is lower than ϵ. We obtain values of $\epsilon < 0.04$, thus showing a very good fit.

Looking at the results listed in Tab. 5.3, we see that in most of the cases there is no need for considering the second Gaussian component of the distribution. Actually, comparable weighting factors for the both components of the bi-modal Gaussian distribution are only obtained for *road crossing - urban* scenarios, for both *single lane* and *multiple lanes*. Exactly in these two scenarios is where the cars experience non-LOS conditions more often, remember here, there are buildings in the four quadrants of the crossing. Also in these two scenarios is where the K-factor is the lowest, with values not much greater than 0 dB. When the TX and the RX cars are in the crossing it is more likely to experience strong LOS conditions. However, there are other cars and objects between them, which results in lower K-factors.

Also low K-factors are obtained for the *in-tunnel* scenario. There, the numerous MPCs stemming from big metallic reflecting objects, such as the ventilation modules, add up causing a low K-factor.

On the other hand, the highest K-factor is observed in the *merging lanes* scenario, together with the smallest standard deviation σ. In this scenario we had a very well defined switch between purely LOS conditions or no link between TX and RX.

The highest value of σ is obtained for the *GLO-h* scenario. As commented before,

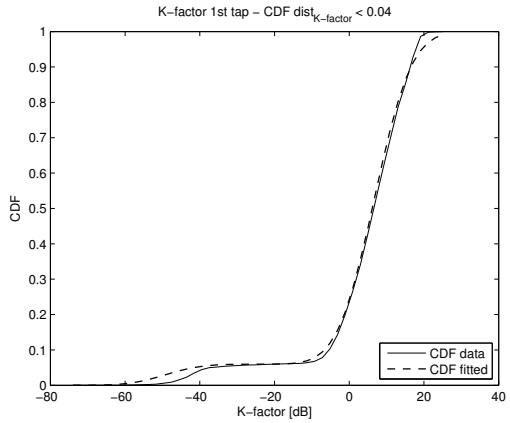

Figure 5.14: Joint CDF - frequency-time dependent K-factor for link 10 (front-front). *GLO-h.*

Table 5.3: Modeling the time-varying K-factor

road crossing - suburban with traffic (3 measurements)							
Parameter	w_1	w_2	μ_1	σ_1	μ_2	σ_2	**GoF**
K [dB]	0.80	0.20	5.06	5.31	−42.32	7.79	< 0.03
road crossing - suburban without traffic (11 measurements)							
Parameter	w_1	w_2	μ_1	σ_1	μ_2	σ_2	**GoF**
K [dB]	0.11	0.89	−42.80	7.92	5.76	5.48	< 0.02
road crossing - urban single lane (5 measurements)							
Parameter	w_1	w_2	μ_1	σ_1	μ_2	σ_2	**GoF**
K [dB]	0.35	0.65	−43.22	7.23	0.54	5.60	< 0.06
road crossing - urban multiple lane (5 measurements)							
Parameter	w_1	w_2	μ_1	σ_1	μ_2	σ_2	**GoF**
K [dB]	0.30	0.70	−43.31	7.59	0.63	4.84	< 0.04
general LOS obstruction - highway (12 measurements)							
Parameter	w_1	w_2	μ_1	σ_1	μ_2	σ_2	**GoF**
K [dB]	0.94	0.06	6.78	7.80	−49.16	7.61	< 0.04
merging lanes - rural (7 measurements)							
Parameter	w_1	w_2	μ_1	σ_1	μ_2	σ_2	**GoF**
K [dB]	0.95	0.05	14.03	4.30	−30.54	22.93	< 0.02
traffic congestion - slow traffic (11 measurements)							
Parameter	w_1	w_2	μ_1	σ_1	μ_2	σ_2	**GoF**
K [dB]	0.07	0.93	−44.78	7.86	5.87	6.85	< 0.02
traffic congestion - approaching traffic jam (7 measurements)							
Parameter	w_1	w_2	μ_1	σ_1	μ_2	σ_2	**GoF**
K [dB]	0.03	0.97	−48.78	7.98	6.94	6.98	< 0.03
in-tunnel (7 measurements)							
Parameter	w_1	w_2	μ_1	σ_1	μ_2	σ_2	**GoF**
K [dB]	0.86	0.14	3.43	5.43	−43.36	7.50	< 0.03
on-bridge (7 measurements)							
Parameter	w_1	w_2	μ_1	σ_1	μ_2	σ_2	**GoF**
K [dB]	0.01	0.99	−1.94	15.13	12.36	4.45	< 0.02

K-factors corresponding to obstructed LOS situations present values close to the ones obtained in LOS conditions. Therefore, the Gaussian component appears widened, and this is modeled by a large value of σ.

Other scenarios where obstructed LOS occurs, and where values of σ are also relatively large are the *traffic congestion* scenarios.

5.2 Time-Varying RMS Delay and Doppler Spreads

A radio channel can be described by its RMS delay and RMS Doppler spreads [94], which have been commonly assumed to be constant in time. However, as seen previously, the fading process in vehicular channels is a non-WSSUS process with local stationarity within a finite stationarity region. As stated before, we concentrate on the non-WSS description of the fading process and therefore, we characterize the vehicular channel parameters as time-varying.

5.2.1 Definition

The second central moments of the PDP and the DSD are important for the description of the fading process. They are directly related to the coherence bandwidth and coherence time of the channel, which indicate the rate of change of the channel in frequency and time, respectively.

The RMS delay spread relates to the coherence bandwidth through an uncertainty relationship as $B_{\mathrm{coh,k}} \geq \arccos(k)/2\pi\sigma_\tau$, with k being a concrete level such that the channel autocorrelation function $\mid R_H(t, B_{\mathrm{coh,k}}) \mid < k$ [95]. The coherence bandwidth indicates the severity of the channels' frequency selectivity. The time selectivity is reflected in the RMS Doppler spread and relates to the coherence time as $T_{\mathrm{coh,k}} \geq \arccos(k)/2\pi\sigma_\nu$, with k such that $\mid R_H(T_{\mathrm{coh,k}}, f) \mid < k$. Usual values of k are 0.5 and 0.75 [94].

The time-varying RMS delay spread

$$\sigma_\tau[k_t] = \sqrt{\frac{\sum_{n=0}^{N-1} (n\tau_\mathrm{s})^2 \hat{P}_\tau[k_t; n]}{\sum_{n=0}^{N-1} \hat{P}_\tau[k_t; n]} - \left(\frac{\sum_{n=0}^{N-1} (n\tau_\mathrm{s}) \hat{P}_\tau[k_t; n]}{\sum_{n=0}^{N-1} \hat{P}_\tau[k_t; n]} \right)^2}, \tag{5.5}$$

and the time-varying RMS Doppler spread

$$\sigma_\nu[k_t] = \sqrt{\frac{\sum_{p=-M/2}^{M/2-1} (m\nu_\mathrm{s})^2 \hat{P}_\nu[k_t;p]}{\sum_{p=-M/2}^{M/2-1} \hat{P}_\nu[k_t;p]} - \left(\frac{\sum_{p=-M/2}^{M/2-1} (m\nu_\mathrm{s}) \hat{P}_\nu[k_t;p]}{\sum_{p=-M/2}^{M/2-1} \hat{P}_\nu[k_t;p]} \right)^2} \tag{5.6}$$

are calculated using the PDP P_τ and DSD P_ν, respectively. Both time-varying spectra are estimated from the LSF as described in Chap. 3.

Some preprocessing on the estimated LSFs is performed in order to eliminate spurious components that would lead to erroneous results. We apply two *power thresholds*: *(i) Noise-thresholding* is needed for eliminating noise components that could be mistaken as MPCs; and *(ii) RX-sensitivity-thresholding* eliminates non-relevant components at the RX due to the RX sensitivity. Here, we choose a *noise-threshold* of 3 dB above the noise floor. The *RX-sensitivity-threshold* is set to −25 dB below the maximum. The thresholding is done separately for each stationarity region.

5.2.2 Empirical Results

Analogously to the previous section, we choose now two single illustrative measurement runs for detailed analysis. At the end of the section we present an overview of the results from the investigation on the whole DRIVEWAY'09 measurement set classified by scenario. Here, we use a *GLO-h* convoy measurement, and a *RC-usl* oncoming measurement. This helps us to highlight the differences between their results.

When analyzing the time-varying channel parameters, it is helpful to look at the time-varying PDP and DSD shown in Fig. 5.15. The PDP is plotted in the upper row (Figs. (a) and (b)), in the lower row the time-varying DSD is shown (Figs. (c) and (d)). The plots on the left hand side of the figure correspond to the crossing scenario in an urban environment. The ones on the right hand side correspond to measurements taken on the highway with TX and RX driving in the same direction.

Looking at Fig. 5.15, we notice the presence of diffuse components, which is more significant in the *urban* scenario. Furthermore, we observe some late components resulting from reflections on other objects on the road. We also highlight that the strong time-variability of the channel is more pronounced in the road crossing measurement. For a more detailed description of the PDP and the DSD, please refer to Chap. 3.

Figure 5.16 depicts the time-varying RMS delay and Doppler spreads for two illustrative measurements. The results for the *highway* measurement are plotted in

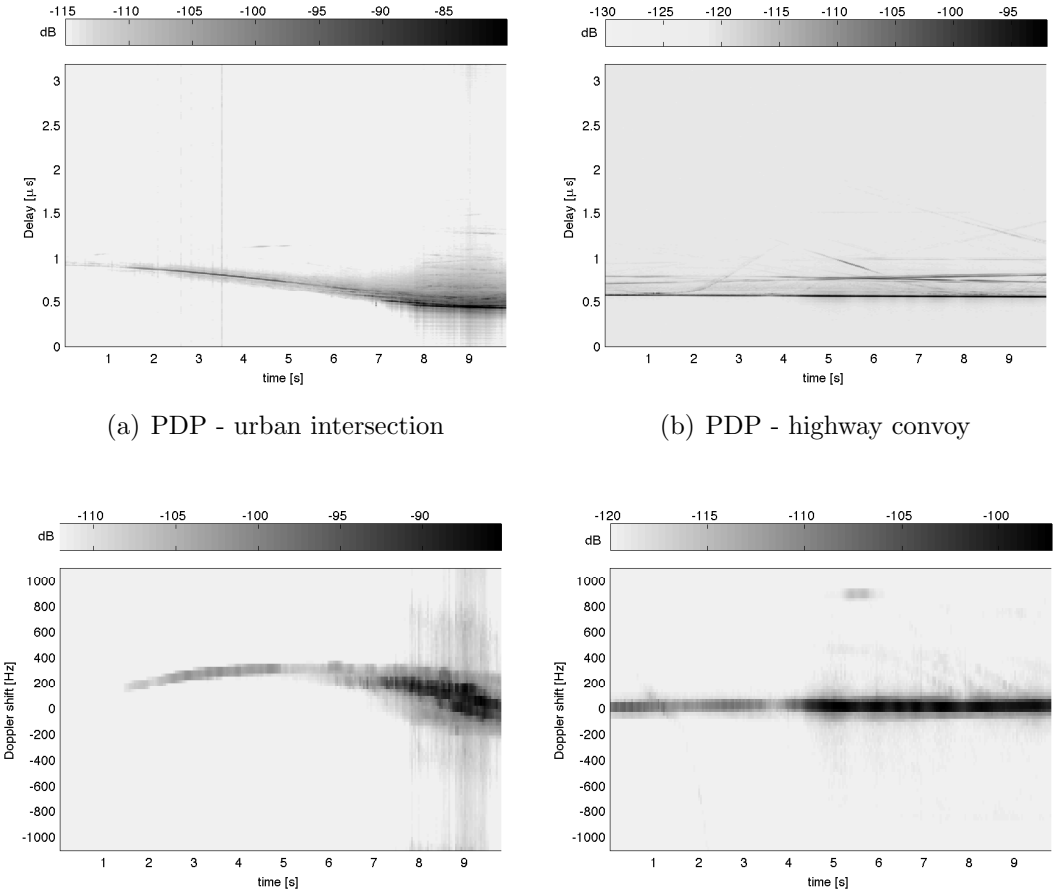

(a) PDP - urban intersection

(b) PDP - highway convoy

(c) DSD - urban intersection

(d) DSD - highway convoy

Figure 5.15: Time-varying power spectral densities from two different measurement scenarios: (a) and (c) *RC-usl* measurement, velocities of approximately 10 km/h (2.78 m/s); (b) and (d) *GLO-h*, convoy measurement with temporally obstructed LOS, constant velocities of 120 km/h (33.33 m/s).

solid line and markers, the results for the *urban* scenario are in mere solid black line.

RMS delay spread σ_τ

Looking at the RMS delay spread, in Fig. 5.16 (a), we observe that for the *GLO-h* scenario it oscillates around 50 ns and it decreases when the MPCs have no significant power, which happens between 2 and 4 s.

For the *RC-usl* scenario, the RMS delay spread $\sigma_\tau[k]$ is higher towards the end

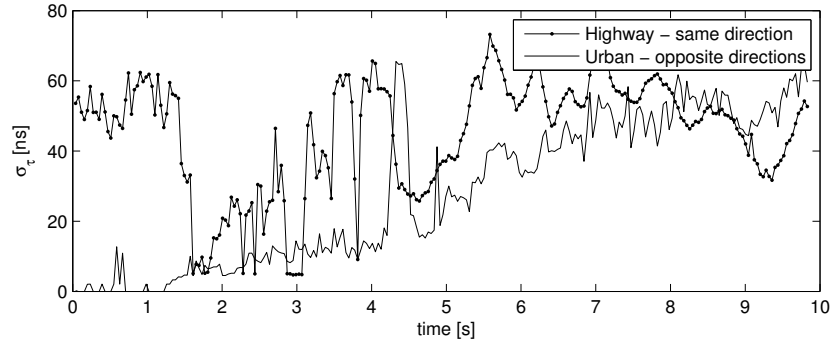

(a) time-varying RMS delay spread

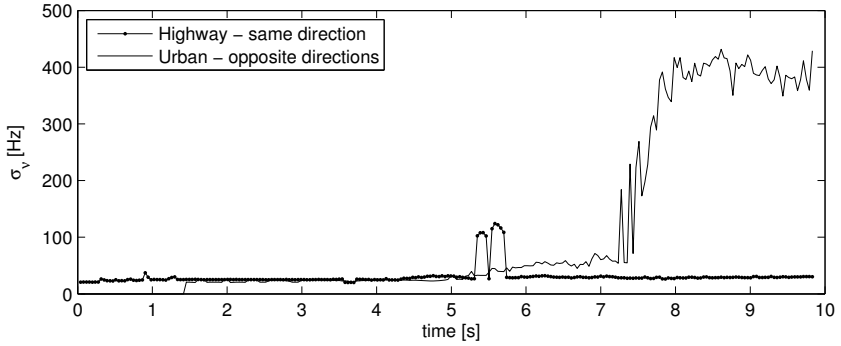

(b) time-varying RMS Doppler spread

Figure 5.16: Time-varying channel parameters for two different measurement scenarios. The solid line with markers corresponds to the *GLO-h* convoy measurement, with constant velocities of 120 km/h (33.33 m/s); the solid line without markers corresponds to the *RC-usl* oncoming measurement, with velocities of approximately 10 km/h (2.78 m/s).

of the measurement run due to the richness of MPCs present in the environment at this moment. Noteworthy is the peak at 4.5 s which occurs due to a strong late contribution, as observable in the PDP in Fig. 5.15 (a).

RMS Doppler spread σ_ν

There is a big difference in the RMS Doppler spread for the two selected measurements, as one can clearly see in Fig. 5.16 (b). The *GLO-h* scenario corresponds to a convoy measurement, i.e. the two cars drive in the same direction at more or less constant speed. This results in a constant Doppler component at 0 Hz, see Fig. 5.15 (d). Therefore, the RMS Doppler spread for this case remains also constant at

around 33 Hz. Nevertheless, it can happen that when new MPCs with strong power are present, it increases, as at 5 s (Fig. 5.15 (d)).

On the other hand, the *RC-usl* measurement consists of two cars approaching each other, i.e. an oncoming measurement. Here we observe a relatively constant RMS Doppler spread around 20 Hz from 1.4 to 5.2 s. As we can see in the DSD plot in Fig. 5.15 (b), we only have one strong Doppler component until 6 s. From this time on, more Doppler components start being present which originates an increase of the RMS Doppler spread. This is represented by the slope of the RMS Doppler spread until 7.3 s. At that point, it reaches a high and constant value oscillating around 370 Hz. The large amount of Doppler components relevant during this period remains also fairly constant, as can be observed in Fig. 5.15 (c).

5.2.2.1 Statistical Modeling

Until now we have been looking at the analysis of a single measurement run, but actually we want to characterize the entire measurement data set and derive a meaningful statistical parametrization for each scenario. Therefore, we perform the same analysis for each individual measurement run for all scenarios.

In order to smoothly proceed from the results presented previously, we remain by the selected example scenarios. We plot in Fig. 5.17 the CDF of the time-varying channel parameters for all measurement runs performed under the same conditions.

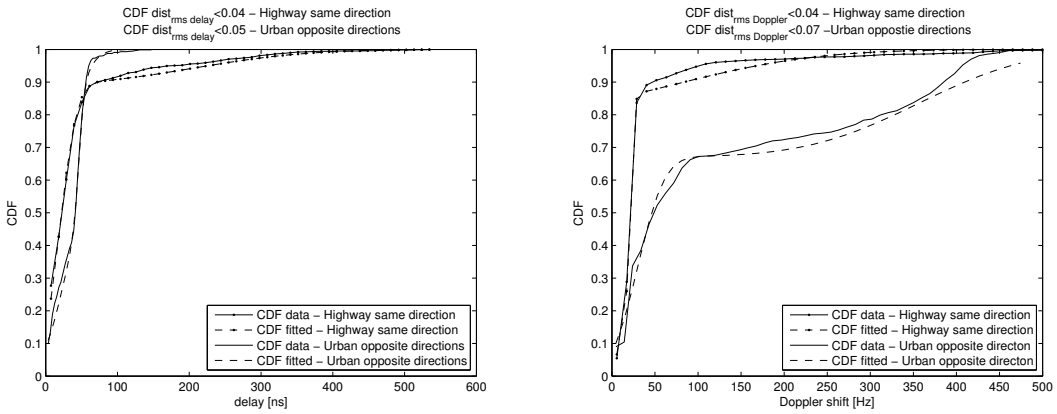

(a) CDF RMS delay spread

(b) CDF RMS Doppler spread

Figure 5.17: CDF of the time-varying channel parameters for the illustrative scenarios: *GLO-h* scenario in lines with markers (12 measurement runs); *RC-usl* scenario in lines without markers (5 measurement runs). The empirical CDF is plotted in solid line, and the fitted CDF in dashed lines.

The solid lines correspond to the empirical CDF obtained from the measurements, in dashed lines we plot the fitted CDF. The two different scenarios are distinguished by the marker symbols, lines with markers correspond to the *GLO-h* scenario, whereas lines without markers are employed for the *RC-usl* scenario.

Based on the shape of the histograms, we chose a bi-modal Gaussian mixture distribution for fitting purposes. We show the good agreement between the empirical and the analytical CDF in Fig. 5.17. Moreover we use here also the KS-test as a GoF indicator, listed on Tab. 5.4.

A bi-modal Gaussian mixture distribution happens to be adequate for modeling the time-varying parameters since the channel parameters are highly dependent on the presence or not of strong MPCs. One of the Gaussian functions encompasses the channel parameters values for a LOS situation when later MPCs have minor relevance. On the other hand, for LOS situations where the later MPCs are significant, the channel parameter values are described by the second Gaussian function.

We perform the same analysis for the whole set of data and show the fitting parameters in Tab. 5.3. Looking at Tab. 5.3 for parameter σ_τ, we see that the weighting factor for one of the Gaussian components is much greater than the other. This means that, most of the time, the propagation conditions remain more or less constant. Nevertheless, due to the LOS to non-LOS transitions, there is still need for a second Gaussian component to properly model the RMS delay and Doppler spreads behavior.

RMS delay spread

Low RMS delay spread values are observed in *suburban* scenarios, such as *road crossing* scenarios. Interestingly, low RMS delay spreads are also obtained in the *highway*, in the *traffic congestion* scenario. As it was already observed in [18], other cars driving beside the TX and the RX are scatterers not as relevant as one might expect. This is due to the fact that the roof-top antenna is placed at a higher position above the other cars. Relevant MPCs come from big scattering objects such as trucks or big metallic structures.

The highest RMS delay spread values are obtained for the *IT* and *OB* scenarios. Big metallic structures, e.g. the ventilation system in the tunnel and metallic holding wires on the bridge, placed relatively close to the vehicles, contribute to increasing the RMS delay spread.

The two merging roads in the *ML-r* scenario were in a *rural* environment, with very few scattering objects in the surroundings and not much traffic, therefore the RMS delay spread is small.

During the measurements taken for the *GLO-h* scenario, several trucks were

Table 5.4: Modeling time-varying channel parameters

road crossing - suburban with traffic (3 measurements)								
Parameter	w_1	w_2	μ_1	σ_1	μ_2	σ_2	**GoF**	**Max**
σ_τ [ns]	0.78	0.22	19.40	5.47	57.60	12.69	< 0.07	93.82
σ_ν [Hz]	0.59	0.41	161.57	97.00	37.50	18.92	< 0.07	342.57
road crossing - suburban without traffic (11 measurements)								
Parameter	w_1	w_2	μ_1	σ_1	μ_2	σ_2	**GoF**	**Max**
σ_τ [ns]	0.16	0.84	39.50	23.58	10.77	7.18	< 0.05	150.00
σ_ν [Hz]	0.59	0.41	28.65	8.74	157.45	108.21	< 0.03	379.10
road crossing - urban single lane (5 measurements)								
Parameter	w_1	w_2	μ_1	σ_1	μ_2	σ_2	**GoF**	**Max**
σ_τ [ns]	0.38	0.62	46.42	6.13	27.72	5.10	< 0.05	150.26
σ_ν [Hz]	0.33	0.67	356.04	10.18	30.10	24.36	< 0.07	479.12
road crossing - urban multiple lane (5 measurements)								
Parameter	w_1	w_2	μ_1	σ_1	μ_2	σ_2	**GoF**	**Max**
σ_τ [ns]	0	1	68.76	247.39	41.70	209.52	< 0.02	748.61
σ_ν [Hz]	0.08	0.92	178.32	137.26	28.02	25.48	< 0.07	636.80
general LOS obstruction - highway (12 measurements)								
Parameter	w_1	w_2	μ_1	σ_1	μ_2	σ_2	**GoF**	**Max**
σ_τ [ns]	0.11	0.89	19.50	125.30	20.70	18.81	< 0.04	293.06
σ_ν [Hz]	0.78	0.22	20.20	17.50	72.27	131.19	< 0.04	312.11
merging lanes - rural (7 measurements)								
Parameter	w_1	w_2	μ_1	σ_1	μ_2	σ_2	**GoF**	**Max**
σ_τ [ns]	0.88	0.12	9.74	5.03	60.94	45.17	< 0.04	170.97
σ_ν [Hz]	0.52	0.48	22.52	4.29	103.89	100.60	< 0.06	329.24
traffic congestion - slow traffic (11 measurements)								
Parameter	w_1	w_2	μ_1	σ_1	μ_2	σ_2	**GoF**	**Max**
σ_τ [ns]	0.62	0.38	8.44	17.96	36.76	6.51	< 0.06	132.91
σ_ν [Hz]	0.75	0.25	21.60	4.43	113.95	91.76	< 0.04	300.59
traffic congestion - approaching traffic jam (7 measurements)								
Parameter	w_1	w_2	μ_1	σ_1	μ_2	σ_2	**GoF**	**Max**
σ_τ [ns]	0.06	0.94	38.57	15.97	10.10	5.63	< 0.10	72.39
σ_ν [Hz]	0.75	0.25	22.29	4.08	67.58	67.68	< 0.04	281.08
in-tunnel (7 measurements)								
Parameter	w_1	w_2	μ_1	σ_1	μ_2	σ_2	**GoF**	**Max**
σ_τ [ns]	0.03	0.97	178.69	13.64	69.79	21.49	< 0.04	179.78
σ_ν [Hz]	0.22	0.78	151.83	82.04	89.82	52.44	< 0.05	385.14
on-bridge (4 measurements)								
Parameter	w_1	w_2	μ_1	σ_1	μ_2	σ_2	**GoF**	**Max**
σ_τ [ns]	0.21	0.79	196.76	104.88	40.79	24.70	< 0.03	926.37
σ_ν [Hz]	0.31	0.69	240.55	106.06	66.70	40.25	< 0.07	855.10

driving beside the TX and the RX and were blocking the LOS. The RMS delay spread in this scenario is mainly determined by the presence of these big objects placed at antenna height.

RMS Doppler spread

In the case of RMS Doppler spread, the weighting factors vary depending on the scenario. Significantly different weighting factors are observed in scenarios with fairly constant relative speeds between the TX and the RX. There, one

can represent the RMS Doppler spread behavior using most of the time a single Gaussian function. In scenarios involving acceleration or braking periods followed by a constant relative speed period, such as in *road crossing* and *merging lanes* scenarios, we need two Gaussian components in order to properly model the RMS Doppler spread.

The RMS Doppler spread is in general larger for the *road crossing* scenarios. A reason for that is the rapid change of the LOS Doppler component from positive to negative values (approaching and leaving). Also high RMS Doppler spreads are observed in the *IT* and *OB* scenarios. There, the later arriving MPCs are strong and therefore contribute to enlarging the RMS Doppler spread values.

The RMS Doppler spreads tend to remain constant at low levels in scenarios where the TX and RX cars are driving in the *same direction*, at the same speed, and where the MPCs are not strong. This is somehow expected since the most relevant component remains around 0 Hz throughout all the measurement run.

Some remarks

It is important to mention here, that the argumentation thread presented until now in this section is based on mean values. It can however happen that for a given time instant, values of RMS delay and Doppler spread do not follow the described trend. Critical values for the RMS spreads are going to be extreme maxima.We also display the extreme maxima in the last column of Tab. 5.4.

The maximum RMS delay spread has been observed in *OB* scenario, being 926.37 ns. The maximum RMS Doppler spread was obtained also for this scenario, with a value of 855.10 Hz. Nevertheless, the most frequently observed maximum values for RMS delay and Doppler spreads are $100 - 200$ ns, and $300 - 400$ Hz, respectively.

5.3 Time-Varying Relevant Scattering Objects

Vehicular antennas are normally mounted on the roof top of the car, this causes that the radio waves interact mostly with objects located at around 1.5 m above the ground. Due to the placement of the antennas, the LOS between the TX and the RX car might be blocked occasionally and intermittently due to bigger vehicles or other objects. When the LOS is not blocked, the channel is dominated by the LOS link. On the contrary, in the case of blocked LOS, the contribution of the MPCs due to reflections becomes more relevant, because the received power is more equally spread among them.

Multipath propagation increases the temporal and directional diversity at the RX. The RX can exploit it and by appropriate techniques decodes the message also

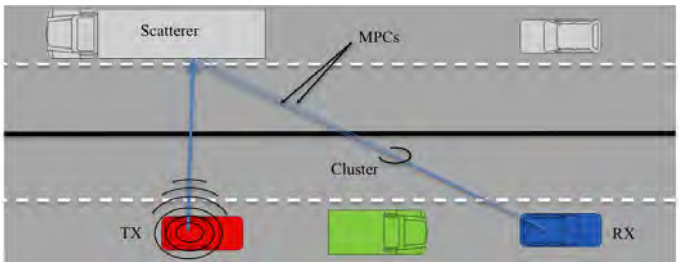

Figure 5.18: MPC and cluster definition.

under non-LOS conditions. In order to test such techniques, numerical simulations on the computer have to be performed. For that, a mathematical representation of the channel is necessary. A well suited approach for modeling the vehicular channel is the so called *geometry-based stochastic channel model* [33], described in Chap. 1. There, the scatterers causing the MPCs are randomly placed beside the TX -RX link according to a spatial distribution. In [33] an accurately parameterized model for LOS situations and its parameters for *highway* and *rural* scenarios is provided.

From a RX point of view, it is not possible to fully exploit all MPCs, since the weak contributions of the received signal are going to be masked by noise due to the RX dynamic range. Therefore, by only modeling the relevant MPCs reaching the RX we can use a simpler channel model for numeric simulations. For doing so, one has to identify all relevant MPCs first. Until now, very few studies have been carried out tackling this issue, also because there are not many vehicular radio channel measurements available.

5.3.1 Cluster-Based Time-Varying Scattering Characterization

As mentioned before, we are interested in describing only the significant MPCs in order to develop simpler mathematical channel models. As a first step towards a geometry-based stochastic channel modeling, it is of great importance to identify which MPCs are truly relevant from the RX point of view. Moreover, in order to reduce the complexity of a channel model even further, we aim at describing groups of MPCs instead of the individual paths. Therefore, as introduced before, we define a *cluster* as the sum of several MPCs stemming from the same scattering object, as symbolically represented in Fig. 5.18.

Previous work that analyzed the scatterer contributions in mobile communications is based on *visual inspection* of the PDP [18], [96], [97]. By using video material recorded during the measurements, the different MPCs observed in the PDP can

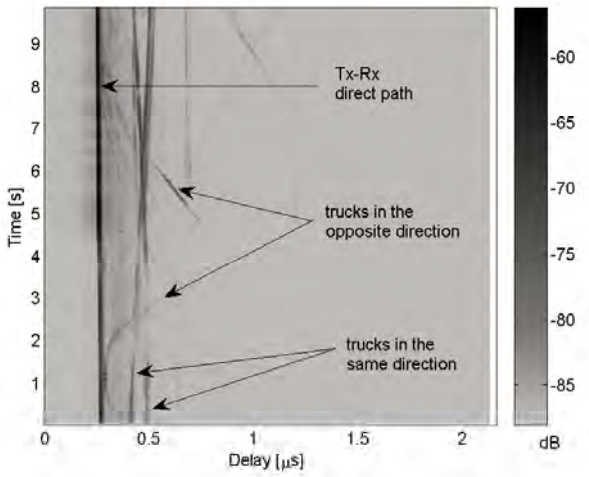

Figure 5.19: Scattering identification by *visual inspection* of the PDP for a *GLO-h* convoy measurement on the highway.

be *visually* identified and related to physical objects that interact with the radio waves. Figure 5.19 shows the MPCs identified with this approach for the *GLO-h* measurement used previously.

For discussing the results in this section, we select again the *GLO-h* scenario, where the TX and RX are driving in the same direction on the highway at around 120 km/h (33.33 m/s) each. There are big trucks driving in both directions beside them. During the measurement run, the LOS between the two cars is intermittently obstructed. The main MPC contributions stem from other trucks and cars driving beside the TX and the RX car.

There are scenarios where it is clear and easy to distinguish the different contributions and to identify the scatterers causing the MPCs. But in other cases, the task becomes too difficult to be done *visually*, such as in scenarios with rich scattering and strong presence of diffuse components. Furthermore, the *visual inspection* method is very time-demanding and the results can be considered to be too *subjective*. Therefore, we should rely on an empirical automated methodology delivering more accurate results.

In order to overcome the drawbacks of the *visual inspection* on the PDP, we add to the used t and τ (based on the PDP $P_\tau[m,n]$) another domain in the analysis, the Doppler shift ν, which gives additional accuracy in the scattering identification. We do that by analyzing the LSF ($C[m,n,p]$), described in Chap. 3.

Figure 5.20 (a) shows the 3D LSF for the same scenario represented in Fig. 5.19

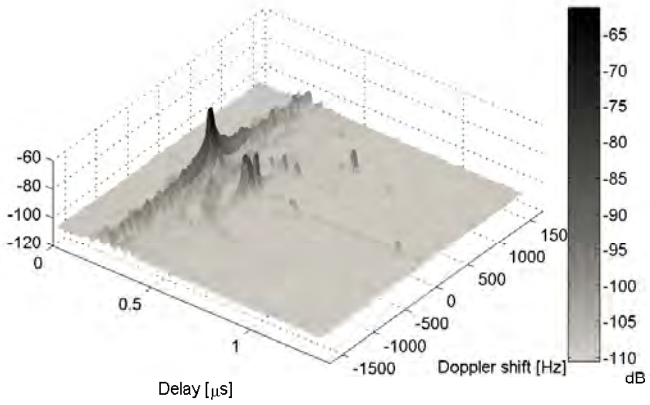

(a) LSF at t=5 s.

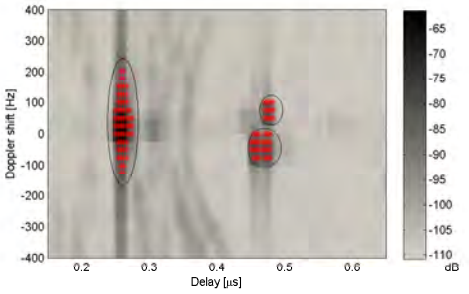

(b) Peak detection on LSF.

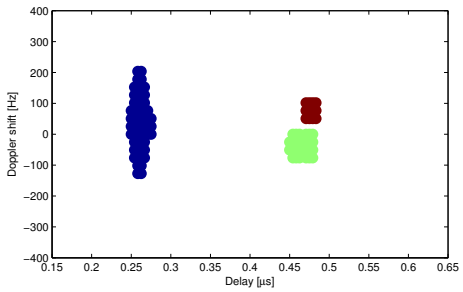

(c) Cluster identification.

Figure 5.20: Peak detection and clustering of MPCs on the LSF.

at $t = 5$ s. Each peak of this plot represents a different scatterer.

First of all, we have to identify the relevant MPCs from the received signal. There are several peaks with low power that are not relevant compared to the highest peak. In order to disregard them, we use a very simple concept, the *power threshold criterion* [73]: A MPC can only exist when it has more power than a certain threshold. We apply then the two *power thresholds* defined previously. We choose the *noise-threshold* to be 15 dB above the noise power, and the *RX-sensitivity-threshold* as 25 dB from the highest detected peak. The two defined thresholds are applied on the LSF individually to each k region, and only the most restrictive threshold is going to be effective. The two thresholds are depicted in Fig. 5.21. These thresholds have been crosschecked using the *visual inspection* approach.

In Fig. 5.20 (b) the detected MPCs are shown with crosses over the LSF at $t = 5$ s seen from the top. We identify three clusters, i.e. groups of MPCs produced by the same scattering object where one MPC is represented by a cross. Each cluster is

marked with an ellipse. Our aim is to identify these clusters in an automated manner. Therefore, we use a clustering algorithm for determining the clusters (scatterers) and characterizing their extension in the delay and Doppler domains.

In order to choose the most suitable clustering algorithm and decide on its input parameters (if needed), we split the DRIVEWAY'09 measurement data into 3 subsets:

1. Training data set: we choose here the *GLO-h* due to its easiness to cross-check results using the *visual inspection* method. The decision on the parameters of the algorithm is made here.

2. Validation data set: we apply the algorithm with the chosen parameters to the *ML-r* set of measurements and verify with *visual inspection* that they deliver the correct results.

3. Application data set: we use the method chosen in (1) and validated in (2) to the rest of measurements.

We decided on the density-based spatial clustering of applications with noise (DBSCAN) algorithm [74] with some modifications. We name the actually used clustering algorithm as *modified* density-based spatial clustering of applications with noise (mDBSCAN). We obtained good results with this algorithm for the training and the validation data sets, therefore we decided to carry out our time-varying cluster parameter analysis with the *mDBSCAN* algorithm. Next we describe the particularities of the algorithm.

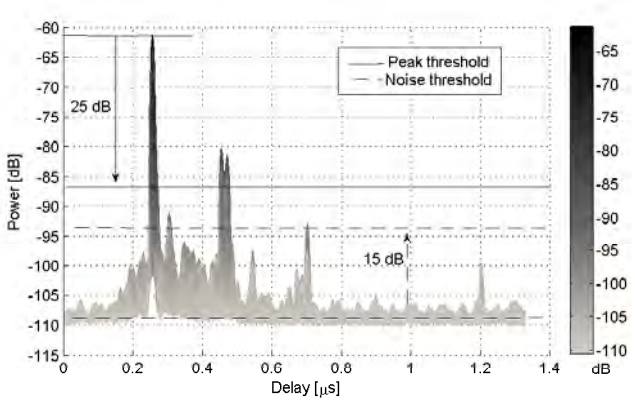

Figure 5.21: LSF for a given time instant with power and noise thresholds shown.

The *mDBSCAN* algorithm is designed to discover clusters of arbitrary shape. It requires only one input parameter. Moreover, *mDBSCAN* is efficient for a large spatial database [74] .

The key idea is that for each point of a cluster, the neighborhood of a given radius (*Eps*) has to contain at least a minimum number of points (*MinPts*), i.e., the density in the neighborhood has to exceed some threshold.

To find a cluster, *mDBSCAN*

1. starts with an arbitrary point p and retrieves all points density-reachable from p with respect to *Eps* and *MinPts*.

2. If p is a core point, this procedure yields a cluster with respect to *Eps* and *MinPts*.

3. If p is a border point, no points are density-reachable from p and DBSCAN visits the next points of the database.

We chose the algorithm parameters as $MinPts = 1$ and $Eps = 7$.

We use the MPC distance d_{MCD} initially defined in [73] for the *KPowerMeans algorithm*. The d_{MCD} allows to combine parameters that come in different units and reads

$$d_{MCD,ij} = \sqrt{d_{\tau,ij}^2 + d_{\nu,ij}^2}, \tag{5.7}$$

where $d_{\tau,ij} = \zeta_\tau \mid \tau_j - \tau_i \mid$, and $d_{\nu,ij} = \zeta_\nu \mid \nu_j - \nu_i \mid$, where τ_x and ν_x denote the coordinate position of the MPC x in the delay and the Doppler domains. The variables ζ_τ and ζ_ν are weighting factors in each dimension. Since we observed that the clusters are larger in the Doppler domain for the given resolution of the LSF, we give more importance to it by setting the weighting factors to $\zeta_\nu = 6$ and $\zeta_\tau = 5$.

Figure 5.20 (c) shows the result of applying *mDBSCAN* on the data displayed on the other two subfigures. Each one of the MPCs is colored according to the cluster assigned by the algorithm.

5.3.2 Time-Varying Cluster Parameters

Since the environment changes very rapidly due to the motion of the TX, the RX, and other moving objects, it is logical to expect that the number of clusters as well as their extension also change in time. Therefore, we describe the cluster parameters as time-varying:

- The *number of clusters* N_c identified in each measurement indicates the number of relevant scattering objects.

- Each cluster is determined by its central position and its *extension in the delay S_τ and Doppler S_ν domain*. The extension is defined as the largest minus the shortest point belonging to the cluster in both domains.

Furthermore, we make a very simple differentiation of the clusters between the first detected cluster (the one with the minimum delay), which we call *1st-cluster*, and the rest, we call them *later-clusters*. This is necessary due to the different characteristics observed between them, as one can already see in Figs. 5.20 (b)-(c). Normally, the *1st-cluster* corresponds to the LOS cluster.

5.3.3 Empirical Results

We have a total of 12 measurement runs available preformed in the *GLO-h* scenario, see Fig. 2.9 (e). In this section we present the detailed results for one of the measurement runs and calculate the temporal mean of the time-varying cluster parameters. At the end, we list the temporal means for all 12 measurement runs and the average value for the whole scenario in a summary table. Moreover, in order to fully describe the clustering parameters, we analyze their distribution. We present a table summarizing the results for the whole DRIVEWAY'09 data ensemble.

Furthermore, we also add the results of another measurement scenario to some of the next figures. We choose a *RC-usl* as a second illustrative measurement, since the scattering characteristics in *urban* environment strongly differ from the ones observed on the *highway*. We then can compare the results obtained for the *GLO-h* and the *RC-usl* measurements. In road crossing measurement, the TX and the RX cars approach an urban crossing driving slowly, at about 15 km/h (4.2 m/s), see Fig. 2.9 (c). There are buildings in all four quadrants of the intersection, which causes a non-LOS communication between TX and RX when the cars are far away from each other. At the end of the measurement run there is a transition from non-LOS to LOS conditions.

MPCs are affected by shadowing and it can happen that a cluster appears and disappears intermittently. In order to avoid too jittery results, we use a moving average window of a length corresponding to 5 stationarity regions. One stationarity region extends over $M = 128$ samples in the time domain, corresponding to 39 ms, and it is the length over which we estimate the LSF.

We calculate the LSFs from the data, detect the peaks, and apply the *mDBSCAN* clustering algorithm. In Fig. 5.22 the time-varying cluster parameters for the two example measurements are shown. The curves with markers plot the results for the *GLO-h* measurement, the solid lines without markers are for the *RC-usl* measurement.

Number of clusters $\mathbf{N_c}$

Figure 5.22 (a) plots the number of clusters. During the *GLO-h* measurement run there are 3 to 4 clusters, which correspond to the visually identified scatterers in Fig. 5.19. During the second half of the measurement, 5 clusters are more often detected. This is due to the fact that the LOS is not blocked anymore and new MPCs appear, or others become stronger.

On the other hand, in *urban* environments we identify more clusters. In the beginning of the *RC-usl* measurement in Fig. 5.22 (a), we observe an oscillation between 1 and 2. Apparently, there are two clusters all the time until 2 seconds, but the second cluster is very weak and sometimes falls below the significance threshold. From 3 to 5 seconds, the number of relevant MPCs increases and so it does the number of clusters. They continue increasing from 5 to 7 seconds, but they are so close to each other that the clustering algorithm is not able to separate them and it appears as if it was a single big cluster. Later on, the clusters move away from each other which allows to identify them individually.

Cluster extension $\mathbf{S}_\tau, \mathbf{S}_\nu$

Previously, we defined the extension of a cluster as the difference between the maximum and minimum delay and Doppler components contained in it. The extension in the delay and Doppler domains for the *1st-cluster* is depicted in Figs. 5.22 (b) and (c). The delay extension remains basically constant during the *GLO-h* measurement. However, there are three time intervals where it increases considerably, at around 1, 4, and 8 s. At these time instances one of the objects driving in the opposite direction is placed between TX and RX. The MPCs coming from this scatterer are very close to the ones of the LOS, and the clustering algorithm is not able to separate them. As a result, the cluster consists of two *merged* clusters and therefore its extension is larger. A similar phenomena happens for the extension in the Doppler domain, but not very pronounced.

A similar effect is appreciated also in the *RC-usl* measurement. There, between 5 and 7 s the clusters are very close to each other and they are seen as a single bigger cluster. Noteworthy is that the cluster extension in the delay and Doppler domains is bigger in *highway* environments, mainly because of the large time-variability of the scatterers in this environment. In *urban* environments we expect to have several clusters close to each other more often, which results in a bigger merged cluster of extension even larger than in the *highway* case. For modeling purposes one have to also account for such effect. If for a given scenario it happens that the clusters are close to each other we can reduce the model complexity by just simulating a single

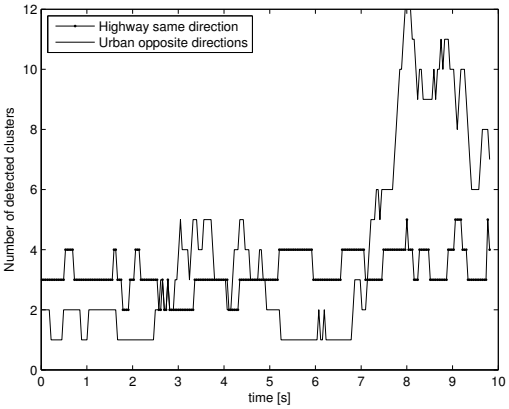

(a) Number of clusters

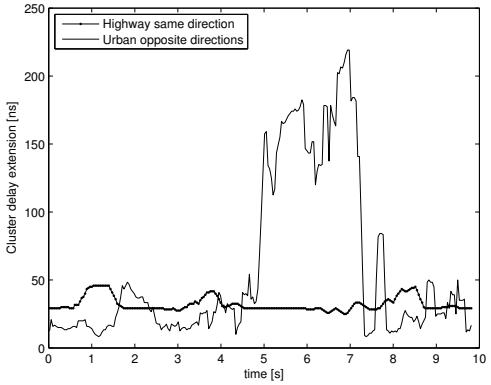

(b) Extension in delay of the *1st-cluster*

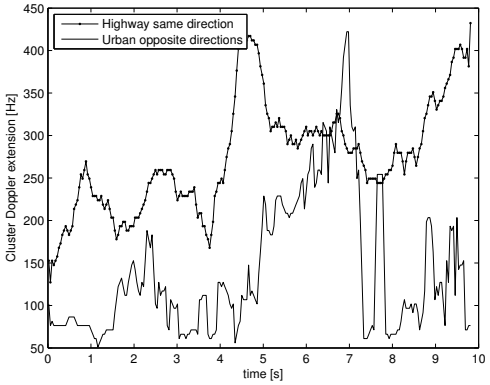

(c) Extension in Doppler of the *1st-cluster*

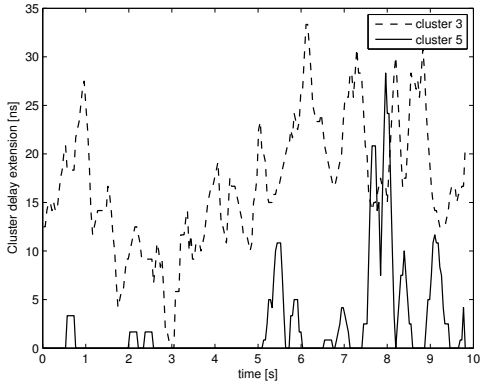

(d) Extension in delay of the *later-clusters* (cluster 3 and 5) only for *GLO-h* scenario

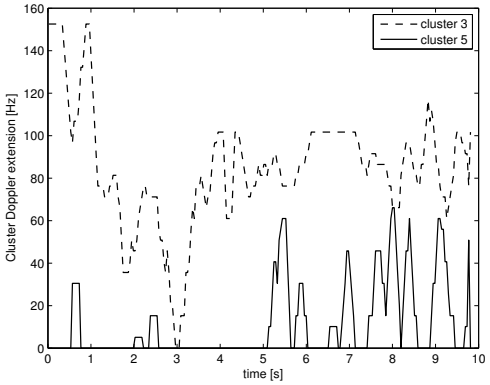

(e) Extension in Doppler of the *later-clusters* (cluster 3 and 5) only for *GLO-h* scenario

Figure 5.22: Time-varying cluster parameters for scenario *GLO-h* (solid line with markers), and *RC-usl* (solid line without markers).

Table 5.5: Mean values of the time-varying channel parameters for *GLO-h* measurement

Parameters	N_c	$S_{\tau,1st}$[ns]	$S_{\tau,later}$[ns]	$S_{\nu,1st}$[Hz]	$S_{\nu,later}$[Hz]
Mean	4	32.03	13.86	275.07	68.61
Std	0.83	5.81	8.01	70.66	40.51
Max	5	45.83	104.17	432.33	152.59
Min	2	25.00	8.34	127.16	50.86

bigger cluster.

We plot in Fig. 5.22 (d) and (e) the cluster extension in the delay and Doppler domains respectively for the *later-clusters*. We represent clusters 3 and 5 only for the *GLO-h* measurement with lines in different styles. One can follow the intermittently presence of a given cluster by observing its time-varying extension.

Table 5.5 lists the temporal mean, maximum, and minimum value for the cluster parameters, as well as the standard deviation for the *GLO-h* measurement throughout the 10 s run. The extension of the *1st-cluster* is larger than for the *later-clusters*, this has been also observed in Fig. 5.20 (b) and (c). Besides the mean, maximum and minimum values, we also provide the standard deviation of the parameters, which we consider can be useful for developing a channel model based on the cluster-based approach. It gives us an idea about how probable it is to observe clusters with either the maximum or the minimum extension.

We performed the same analysis for the 12 measurement runs in *GLO-h* and show the temporal mean values in Tab. 5.6. At the end of the table, there is the average among the whole set of measurements, and also the average of the standard deviation calculated for each measurement run. The number of clusters oscillates between 1 and 7. However, one cluster was detected in only one occasion, in measurement 6. During this measurement, there is only one strong component, which intermittently disappears, this is why there are no values for the extension for the *later-clusters*.

In general, clusters show different shapes for the *1st-cluster* and the *later-clusters*.

Furthermore, as already pointed out previously, the *1st-cluster* presents different characteristics than the *later-clusters*:

- Its extension in the delay and Doppler domain is larger than for the others, and with also larger standard deviation.
- It is present during the whole measurement run (as long as there is a detected signal).
- It has the highest power.

Table 5.6: Temporal mean value of the cluster parameters for the *GLO-h* scenario

Parameters	N_c	$S_{\tau,1st}$[ns]	$S_{\tau,later}$[ns]	$S_{\nu,1st}$[Hz]	$S_{\nu,later}$[Hz]
Measurement 1	7	38	10.77	230.33	64.4
Measurement 2	6	45.27	12.36	387.13	68.73
Measurement 3	7	49.39	12.25	366.78	67.05
Measurement 4	4	34.42	9.79	297.34	58.15
Measurement 5	2	38.38	6.51	202.43	41.36
Measurement 6	1	18.01	1.67	90.74	7.63
Measurement 7	5	50.85	9.98	389.53	63.06
Measurement 8	3	43.27	10.23	311.50	56.15
Measurement 9	3	33.16	9.65	297.47	52.53
Measurement 10	4	32.03	13.86	275.07	68.61
Measurement 11	2	28.87	8.98	334.03	50.84
Measurement 12	2	38.22	13.11	145.98	62.22
Total avg	4	37.49	9.93	277.36	55.06
Std avg	2.04	9.18	3.28	94.26	17.03

- When TX and RX drive in the same direction and at similar speed, it does not change its position in the delay-Doppler plane. Nevertheless, for opposite direction measurements, the *1st-cluster* varies its position too.

On the other hand, the *later-clusters* present a different behavior:

- There are clusters appearing and disappearing quickly, caused by objects which become relevant when they are close to the TX -RX link.
- There are clusters remaining longer active and moving, caused by objects (mainly big metallic objects such as trucks and bridges) which have a stronger influence on the radiowave propagation.

At this point, and thinking of the possible application of the clustering approach for channel modeling, let us make some considerations. Each group of MPCs, which we gather and call cluster, has a center point and a maximum power. The maximum power of each cluster decays exponentially in the delay domain. Moreover, the power within one cluster is Gaussian distributed in the delay and Doppler domain. Notice here that we observe the 2-dimensional Gaussian decay as an effect derived from using the multitaper estimator for obtaining the LSFs. When deriving a channel model, one can use an exponentially decay in the delay domain and Gaussian in the Doppler shift direction, in order to agree with physical explanation.

5.3.3.1 Statistical Modeling

For modeling purposes, one might be interested in knowing how the cluster parameters are distributed. Therefore, we perform an exhaustive analysis of the whole DRIVEWAY'09 set of data and fit the parameters for each scenario using statistical distributions. In the following, we only show the figures of the fitting results for the *GLO-h*.

We use a discrete exponential distribution for fitting the number of clusters, shown in Fig. 5.23 (a). For the cluster extension in delay and Doppler, we use a bi-modal Gaussian mixture distribution, plotted in Fig. 5.23 (b) and (c), respectively. In this case, the first component of the Gaussian distribution models the cluster extension in presence of rich scattering when clusters are undistinguishable and merge. Whereas the second component represents the instances with a poor scattering environment, where clusters are easy to separate. We use the KS test as a GoF indicator and obtain values smaller than $\epsilon = 0.10$ for these particular scenarios.

We fitted all time-varying cluster parameters extracted from DRIVEWAY'09 data, the results are listed in Tab. 5.7. The KS-test result is also listed on the last column of the same table under GoF. We now discuss the results of the different cluster parameters:

Number of clusters $\mathbf{N_c}$
The mean N_c depends on the scattering richness of the environment. Hence, mean values of N_c range from 1, observed in *ML-r* scenario, where there are very few scatterers, to 6 and 5 in *RC-uml* and in *IT* scenarios, where we have a rich scattering environment.

Cluster extension $\mathbf{S}_\tau$, $\mathbf{S}_\nu$
Regarding the cluster extension parameters, clusters with similar weighting factors, and significantly different mean μ and variance σ values, present a more time-varying behavior.

We remark here the observation made before that the *1st-cluster* is the strongest one and corresponds in most of the cases to the LOS contribution. During one measurement, other clusters come closer to the LOS and then leave again. During the time instances where the two clusters are very near, they merge and appear as a single bigger cluster. This, seen from the point of view of a cluster, is as if there was one single cluster that grows and shrinks.

Due to the strength of the MPCs close to the TX -RX link, this phenomena of time-varying merging clusters is mostly observed for the *1st-cluster*. This is why the

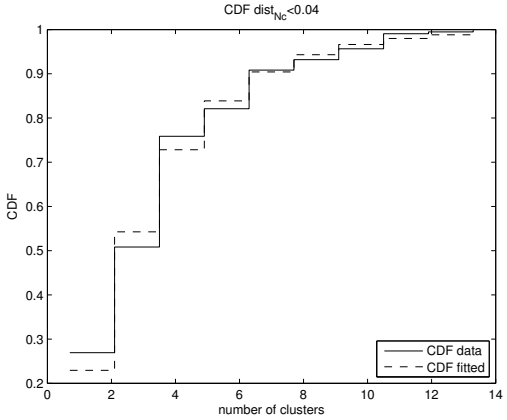

(a) CDF number of clusters

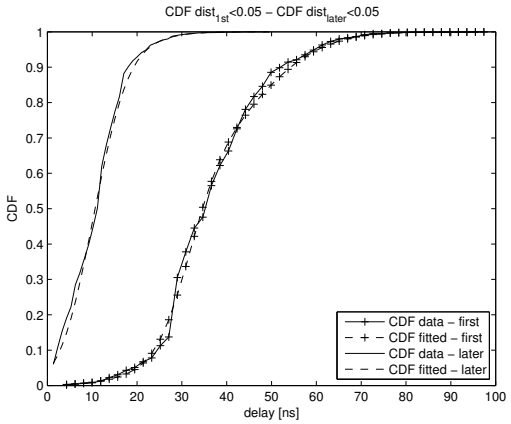

(b) CDF cluster extension in delay

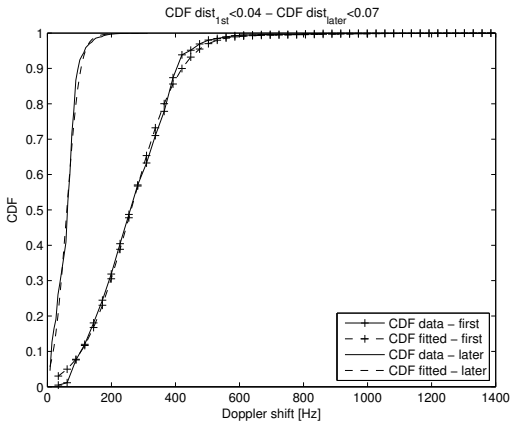

(c) CDF cluster extension in Doppler

Figure 5.23: CDF of the time-varying cluster parameters for scenario *GLO-h*. 12 measurement runs.

weighting factors are similar in the *1st-cluster*.

As observed before, the *1st-cluster* has bigger extension than the *later-clusters*. In order to explain that, let us remind here that the used algorithm for cluster detection consists of applying a threshold on the power in each individual LSF. The *1st-cluster* is the strongest and by thresholding we just take more cluster surface into account, and later and weaker clusters have smaller extension. Therefore it is not surprising that it has the highest cluster extension values.

The delay extension of the *1st-cluster* is smaller in environments with poor scattering, namely in *rural*, and *suburban* areas. On the other hand, in *urban* environments and *in-tunnel* scenarios, the rich scattering surroundings lead to large delay extensions. Noteworthy is the comparison of the delay extension of the *1st-cluster* for the *road crossing* scenario in different environments. The extension is around two times bigger in *urban* environment (around 100 ns) than in *suburban* (around 50 ns).

The Doppler extension of the *1st-cluster* depends on the driving velocities of the TX, the RX, and the surrounding objects. In general, high speeds manifest in larger Doppler cluster extensions, whereas low speeds result in smaller cluster Doppler extensions.

In *road crossing* scenarios, since they were measured in *urban* and *suburban* areas, the driving speeds never exceeded 50 km/h (13.89 m/s). There, we obtain Doppler extension values of around 220 Hz. Measurements taken on the *highway* deliver higher values, such as for the *GLO-h* scenario, with a Doppler extension of 300 Hz and driving speeds of around 120 km/h (33.33 m/s). The highest value is observed for *IT* scenario, where the presence of good reflecting objects plays an important role.

The *later-clusters*, meaning all the clusters except the *1st-cluster*, have bigger extension in *urban* and *suburban* environments. There, the later MPCs are strong and, as explained previously, the thresholding cuts a wider area.

Table 5.7: Modeling time-varying cluster parameters

road crossing - suburban with traffic (3 measurements)								
Parameter	w_1	w_2	μ_1	σ_1	μ_2	σ_2	μ	**GoF**
N_C	–	–	–	–	–	–	2	< 0.10
$S_{\tau,1st}$ [ns]	0.75	0.25	45.05	15.13	10.38	5.65	–	< 0.06
$S_{\nu,1st}$ [Hz]	0.31	0.69	58.75	37.68	304.91	76.55	–	< 0.03
$S_{\tau,later}$ [ns]	0.79	0.21	12.05	6.26	2.82	1.24	–	< 0.03
$S_{\nu,later}$ [Hz]	0.60	0.40	40.53	25.82	93.97	44.72	–	< 0.06
road crossing - suburban without traffic (11 measurements)								
Parameter	w_1	w_2	μ_1	σ_1	μ_2	σ_2	μ	**GoF**
N_C	–	–	–	–	–	–	2	< 0.05
$S_{\tau,1st}$ [ns]	0.44	0.56	67.98	47.32	21.11	11.65	–	< 0.04
$S_{\nu,1st}$ [Hz]	0.28	0.72	71.68	34.35	284.24	99.20	–	< 0.05
$S_{\tau,later}$ [ns]	0.85	0.15	7.70	7.00	56.43	$1.06 \cdot 10^{-3}$	–	< 0.04
$S_{\nu,later}$ [Hz]	0.18	0.82	157.90	66.18	42.56	32.86	–	< 0.06
road crossing - urban single lane (5 measurements)								
Parameter	w_1	w_2	μ_1	σ_1	μ_2	σ_2	μ	**GoF**
N_C	–	–	–	–	–	–	3	< 0.14
$S_{\tau,1st}$ [ns]	0.45	0.55	157.93	57.79	19.75	14.48	–	< 0.03
$S_{\nu,1st}$ [Hz]	0.51	0.49	341.00	154.27	80.04	37.95	–	< 0.03
$S_{\tau,later}$ [ns]	0.85	0.15	7.70	6.70	56.43	33.61	–	< 0.02
$S_{\nu,later}$ [Hz]	0.83	0.17	40.92	29.58	186.86	100.50	–	< 0.04
road crossing - urban multiple lane (5 measurements)								
Parameter	w_1	w_2	μ_1	σ_1	μ_2	σ_2	μ	**GoF**
N_C	–	–	–	–	–	–	6	< 0.13
$S_{\tau,1st}$ [ns]	0.54	0.46	26.20	17.67	129.77	46.69	–	< 0.05
$S_{\nu,1st}$ [Hz]	0.60	0.40	278.15	111.35	86.12	22.35	–	< 0.04
$S_{\tau,later}$ [ns]	0.25	0.75	35.84	21.87	11.63	8.34	–	< 0.02
$S_{\nu,later}$ [Hz]	0.79	0.21	52.76	34.49	128.30	178.32	–	< 0.04
general LOS obstruction - highway (12 measurements)								
Parameter	w_1	w_2	μ_1	σ_1	μ_2	σ_2	μ	**GoF**
N_C	–	–	–	–	–	–	3	< 0.04
$S_{\tau,1st}$ [ns]	0.45	0.55	31.60	5.30	40.88	14.89	–	< 0.05
$S_{\nu,1st}$ [Hz]	0.99	0.01	260.12	120.83	766.36	283.19	–	< 0.04
$S_{\tau,later}$ [s]	0.12	0.88	16.83	8.98	10.15	5.86	–	< 0.05
$S_{\nu,later}$ [Hz]	0.96	0.04	59.98	31.93	116.41	52.06	–	< 0.07
merging lanes - rural (7 measurements)								
N_C	–	–	–	–	–	–	1	< 0.08
$S_{\tau,1st}$ [ns]	0.18	0.82	14.05	13.26	28.05	3.54	–	< 0.10
$S_{\nu,1st}$ [Hz]	0.21	0.79	393.25	26.32	218.24	88.54	–	< 0.07
$S_{\tau,later}$ [ns]	0.63	0.37	12.28	7.11	2.20	1.24	–	< 0.05
$S_{\nu,later}$ [Hz]	0.69	0.31	63.45	37.15	16.42	6.30	–	< 0.03
traffic congestion - slow traffic (11 measurements)								
Parameter	w_1	w_2	μ_1	σ_1	μ_2	σ_2	μ	**GoF**
N_C	–	–	–	–	–	–	3	< 0.04
$S_{\tau,1st}$ [ns]	0.72	0.28	29.36	4.08	83.67	46.37	–	< 0.04
$S_{\nu,1st}$ [Hz]	0.14	0.86	398.45	23.66	245.50	83.96	–	< 0.04
$S_{\tau,later}$ [ns]	0.91	0.09	9.03	6.92	27.83	21.12	–	< 0.02
$S_{\nu,later}$ [Hz]	0.10	0.90	145.25	53.38	47.30	32.09	–	< 0.05
traffic congestion - approaching traffic jam (7 measurements)								
Parameter	w_1	w_2	μ_1	σ_1	μ_2	σ_2	μ	**GoF**
N_C	–	–	–	–	–	–	3	< 0.11
$S_{\tau,1st}$ [ns]	0.35	0.65	59.07	24.38	36.28	7.80	–	< 0.03
$S_{\nu,1st}$ [Hz]	0.68	0.32	216.30	60.66	369.01	33.61	–	< 0.04
$S_{\tau,later}$ [ns]	0.06	0.94	22.86	13.71	8.32	6.30	–	< 0.05
$S_{\nu,later}$ [Hz]	0.83	0.17	59.62	28.34	15.61	4.27	–	< 0.06
in-tunnel (7 measurements)								
Parameter	w_1	w_2	μ_1	σ_1	μ_2	σ_2	μ	**GoF**
N_C	–	–	–	–	–	–	5	< 0.16
$S_{\tau,1st}$ [ns]	0.59	0.41	176.04	84.56	74.17	30.52	–	< 0.03
$S_{\nu,1st}$ [Hz]	0.68	0.32	295.73	71.27	339.02	93.28	–	< 0.06
$S_{\tau,later}$ [ns]	0.01	0.99	119.62	99.00	11.05	11.85	–	< 0.07
$S_{\nu,later}$ [Hz]	0.50	0.50	47.98	38.47	59.98	38.47	–	< 0.08
on-bridge (4 measurements)								
Parameter	w_1	w_2	μ_1	σ_1	μ_2	σ_2	μ	**GoF**
N_C	–	–	–	–	–	–	3	< 0.04
$S_{\tau,1st}$ [ns]	0.18	0.82	37.49	15.36	27.76	2.69	–	< 0.08
$S_{\nu,1st}$ [Hz]	0.30	0.70	394.21	29.12	256.97	72.87	–	< 0.06
$S_{\tau,later}$ [ns]	0.84	0.16	11.30	5.43	3.04	1.22	–	< 0.04
$S_{\nu,later}$ [Hz]	0.24	0.76	19.88	8.27	69.60	16.51	–	< 0.06

6 Conclusions

6.1 Summary

In this thesis I analyzed the *non-stationarity* of the vehicular radio channel. I started by briefly describing the measurement data used throughout the thesis, collected in a vehicular radio channel measurement campaign for different scenarios. The scenarios are based on safety-relevant applications for intelligent transportation systems (ITS).

I briefly revisited the well-known wide sense stationary (WSS) and uncorrelated scattering (US) assumptions. Since the vehicular wireless channel is characterized by a *non-stationary* fading process, I defined a *minimum stationarity region*, over which I assumed the observed process to be WSSUS. Then, I applied the multitaper-based local scattering function (LSF) estimator in its discrete form for characterizting the time-, frequency-varying scattering function.

I proposed to use a two-dimensional (2D) Wiener filter for choosing the number of tapers of the estimator, where the filter coefficients are calculated from the LSF. I assessed the performance of the LSF by means of the mean square error (MSE) at the output of the 2D Wiener filter.

I also derived the time- and frequency-varying projections of the LSF on the delay and the Doppler domains. I visually inspected the main contributions on the time- and frequency-varying power delay profile (PDP) and the time- and frequency-varying Doppler power spectral density (DSD).

In order to check whether the *minimum stationarity region* can be enlarged, I proposed to use two different spectral metrics to test stationarity in time and in frequency domain: the spectral divergence (SD), and the collinearity. I applied them on the LSF for testing the validity of the WSS and the US assumption.

I proceeded with the stochastic characterization of the radio channel considering the whole bandwidth for better resolution in the delay domain. I extracted and stochastically modeled the following time-varying channel parameters: the first order moment of the fading process by means of its K-factor, and the second order moment by means of the root mean square (RMS) delay and Doppler spreads. All these parameters are derived from the LSF.

I also presented a scattering identification method based on the clustering of

MPCs observed in the delay-Doppler domain. Each cluster consists of contributions coming from the same scatterer.

6.2 Key Findings

In this section I will list the main results of the thesis topic-wise.

Locally Defined Power Spectral Densities

I used the multi-taper based LSF estimator for describing the *non-stationary* vehicular channel fading process. I showed that there is an optimal number of tapers combination which results in a low MSE without large computational complexity. I concluded that a good choice for the number of tapers is $I = 3$ in time and $J = 3$ in frequency.

I analyzed in detail the time-varying PDP and DSD for three illustrative measurement runs. I observed that a group of multipath components (MPCs) can be associated to one scatterer, and concluded that the objects originating the main contributions can be classified into: *(i)* the LOS link between transmitter (TX) and receiver (RX), *(ii)* other cars acting as scatterers, *(iii)* trucks or vans, which create, in general, stronger contributions than conventional cars, *(iv)* big metallic surfaces such as traffic signs, street lamps, bridges, or ventilation systems, and *(v)* ceiling and walls in an in-tunnel scenario.

The (in-)Validity of the WSSUS Assumption in Vehicular Radio Channels

Using the SD in time and frequency I showed that the V2V channels violate the WSS assumption much stronger than the US assumption. This conclusion is qualitative since the SD is an unbounded metric and a meaningful threshold could not be derived.

I set an indicative threshold on the collinearity, which is a bounded metric, $\alpha_{\text{th}} = 0.9$, over which I consider the observed process to be stationary either in time or in frequency, and based on it defined the stationarity time T_{stat} and the stationarity bandwidth F_{stat}.

I conclude that the *minimum stationarity region* length used for estimating the LSF is approximately 40 ms in time and 40 MHz in frequency. It is therefore safe to conclude that violations of the US assumption are not observable within the 10 MHz bandwidth of an IEEE 802.11p system, meant to be used for vehicular communications. However, violations of the WSS assumption are relevant to IEEE 802.11p

systems because the frame duration may exceed the stationarity time. Furthermore, consecutive frames will experience different fading statistics.

The obtained results indicate that violations of the WSS assumption do not necessarily imply violations of the US assumption.

Time-Varying Stochastic Characterization of the Vehicular Channel

I used a bi-modal Gaussian distribution for fitting the distribution of the parameters because it is adequate for modeling the two main situations in V2V channels. One of the Gaussian functions characterizes the parameters under LOS situation, and the other Gaussian function characterizes them in non-LOS situation. The weighting factor of these functions is an indicator of the probability of having or not LOS in a particular scenario. I used an exponential distribution for fitting the number of scatterers.

Time-, Frequency-, Space-varying K-factor

I found that the first delay bin is Ricean distributed with a varying K-factor, and the following delay bins are mostly Rayleigh distributed. I showed that the K-factor varies in the time, frequency, and spatial domain. These variations should not be ignored.

I observed that the K-factor varies depending on several factors: *(i)* Number of illuminated scatterers due to the antenna radiation pattern and objects in between TX and RX, *(ii)* the antenna radiation pattern changes over frequency, and *(iii)* presence of good reflecting objects near the cars (e.g. traffic signs).

The largest K-factor is observed in the *rural* environment for the *merging lanes* scenario with very few scatterers. The lowest K-factor is observed in rich scenarios with rich scattering and with non-LOS situations, such as in *road crossing* scenarios. The K-factors obtained for obstructed LOS situations are close to those for LOS situations.

Time-Varying RMS Delay and Doppler Spreads

I formulated the RMS delay and RMS Doppler spread as time-varying channel parameters. By looking at the mean values of the time-varying parameters for all measured scenarios, I conclude that high RMS delay spreads are mostly observed: *(i)* in *urban* environments with rich scattering, *(ii)* situations with obstruction of the line of sight with big reflecting objects driving beside the TX and RX direct link, and *(iii)* in environments where big metallic structures are placed close to the TX-RX. High RMS Doppler spreads occur in: *(i)* drive-by

scenarios, and *(ii)* situations where late Doppler components are significant, mainly caused by good reflecting objects.

Time-Varying Relevant Scattering Objects

I characterized the number of clusters, i.e. scatterers, as well as their extension in the delay and Doppler domain. The number of clusters is strongly correlated with the scattering richness of the environment. Hence, in *rural* environments, very few scatterers are expected, and therefore, the number of clusters is also low, opposite to the case for *urban* environment.

The cluster with the shortest time delay is the strongest one and its properties are different from the clusters with larger delay. The later clusters tend to be smaller and their extension becomes wider the closer they are to the TX-RX link, i.e. to the first cluster.

Poor scattering surroundings, as in *rural* and *sub-urban* environments, will result in smaller cluster delay extension. On the other hand, *urban* and in-tunnel scenarios show the highest delay extensions. Similarly, the Doppler extension depends on the velocities of the TX, the RX, and the other scatterers, being small for low-speed, as in *road crossing* scenarios, and high for high-speed, as in *highway* scenarios.

6.3 Outlook

Until now, researchers dealing with wireless communications always assumed that the fading process underlying them was stationary in time and in frequency. Most of the algorithms for properly receiving/transmitting a signal are designed under this assumption. In this thesis, I showed that in fast-time varying and strong frequency selective channels, these assumptions only hold for a limited time-frequency region. Hence, there is room for improvement on transciever algorithms, that use channel parameters as an input, by including their *non-stationary* description. Furthermore, I showed the usefulness of a new tool for scatterer identification, which can help researchers in developing simpler but yet accurate geometry-based stochastic vehicular channel models.

A Appendix

This appendix provides the results for all measurement data. During the thesis we always chose one illustrative measurement for detailed explanation.

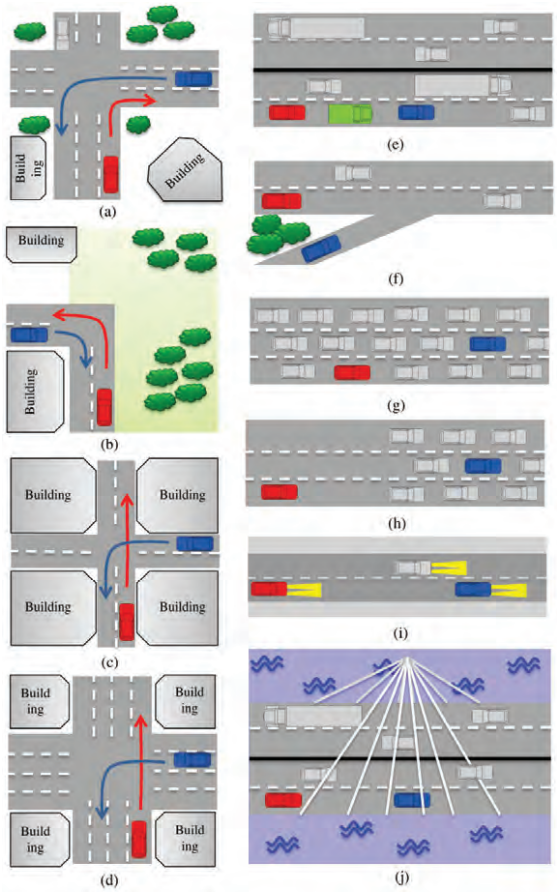

Figure A.1: DRIVEWAY'09 scenarios: (a) *road crossing - suburban with traffic*, (b) *road crossing - suburban without traffic*, (c) *road crossing - urban single lane*, (d) *road crossing - urban multiple lane*, (e) *general LOS obstruction - highway*, (f) *merging lanes - rural*, (g) *traffic congestion - slow traffic*, (h) *traffic congestion - approaching traffic jam*, (i) *in-tunnel*, (j) *on-bridge*.

A.1 Road Crossing

A.1.1 Road Crossing - Suburban with Traffic

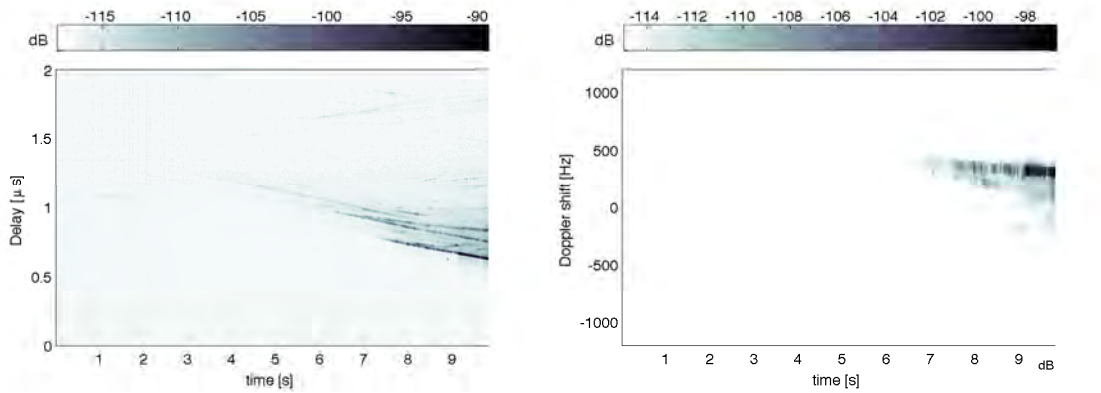

(a) PDP (b) DSD

Figure A.2: Time-varying PDP and DSD for road crossing - suburban with traffic.

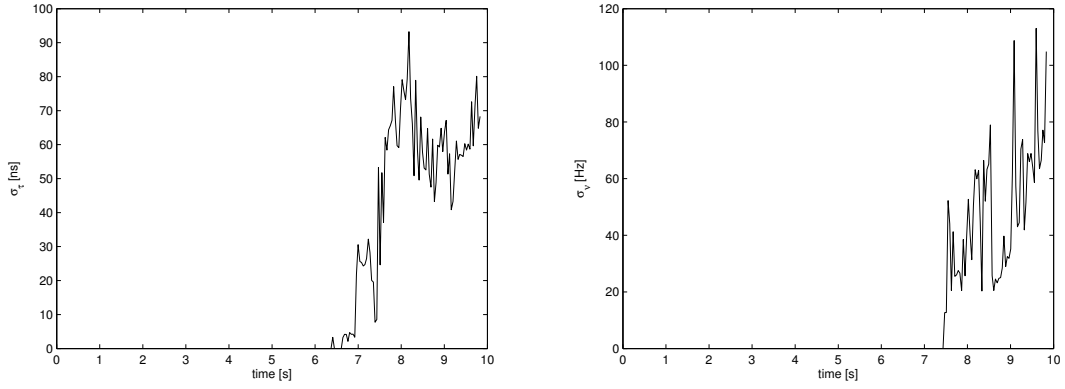

(a) RMS delay spread (b) RMS Doppler spread

Figure A.3: Time-varying channel parameters for road crossing - suburban with traffic.

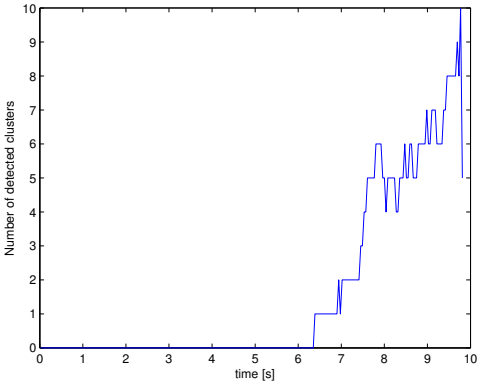

(a) Number of clusters

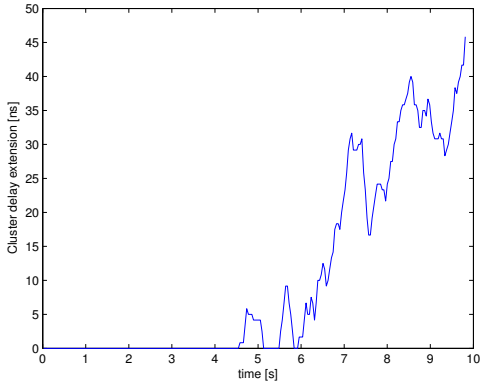

(b) Cluster delay extension - 1st-cluster

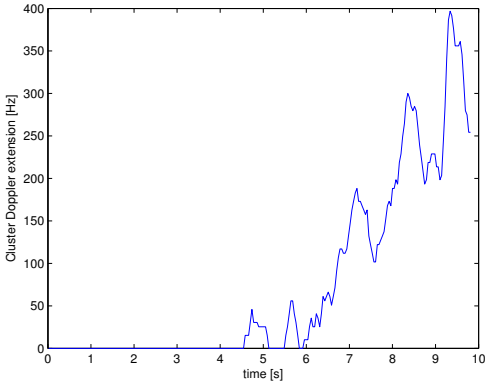

(c) Cluster Doppler extension - 1st-cluster

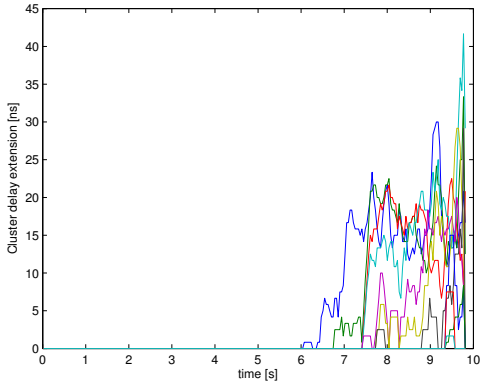

(d) Cluster delay extension - later-clusters

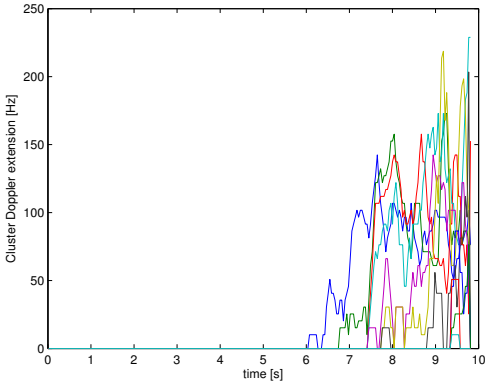

(e) Cluster Doppler extension - later-clusters

Figure A.4: Time-varying cluster parameters for road crossing - suburban with traffic.

A.1.2 Road Crossing - Suburban without Traffic

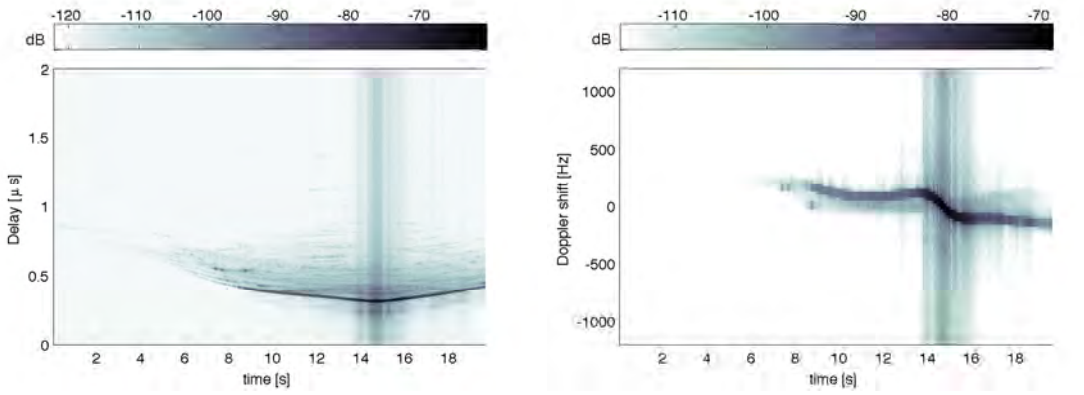

(a) PDP (b) DSD2

Figure A.5: Time-varying PDP and DSD for road crossing - suburban without traffic.

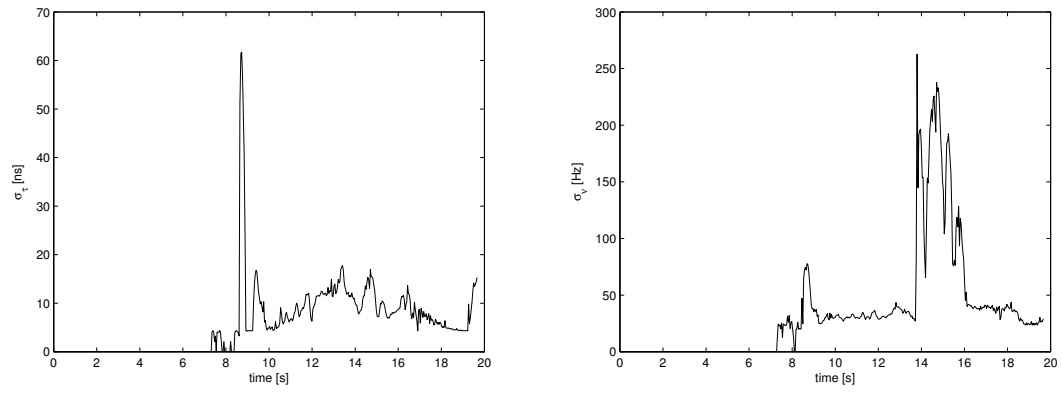

(a) RMS delay spread (b) RMS Doppler spread

Figure A.6: Time-varying channel parameters for road crossing - suburban without traffic.

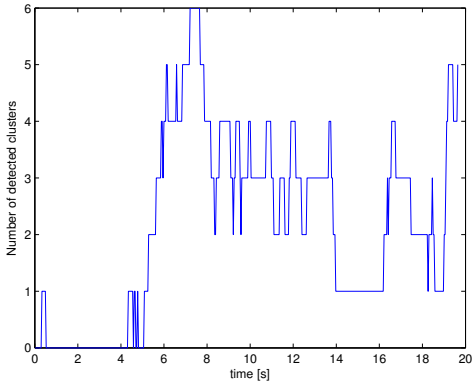

(a) Number of clusters

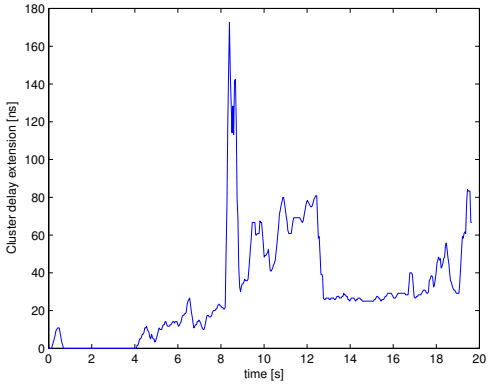

(b) Cluster delay extension - 1st-cluster

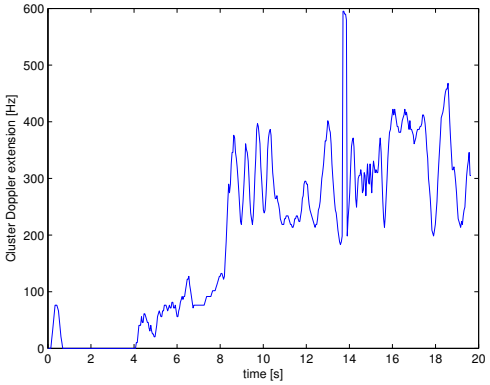

(c) Cluster Doppler extension - 1st-cluster

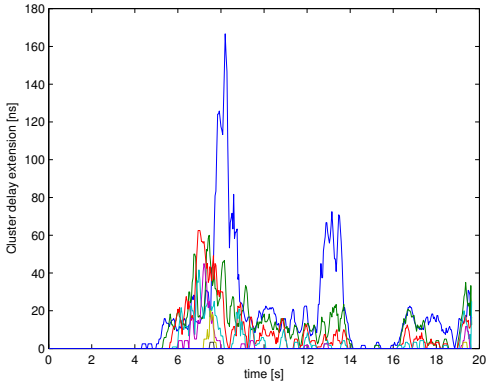

(d) Cluster delay extension - later-clusters

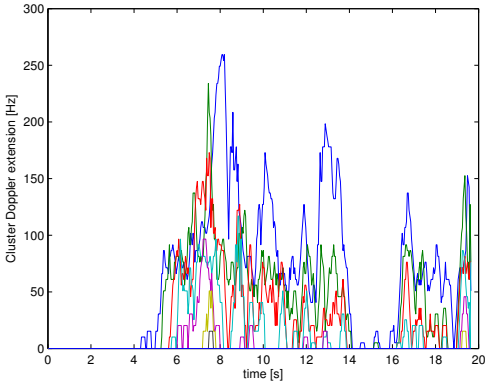

(e) Cluster Doppler extension - later-clusters

Figure A.7: Time-varying cluster parameters for road crossing - suburban without traffic.

A.1.3 Road Crossing - Urban Single Lane

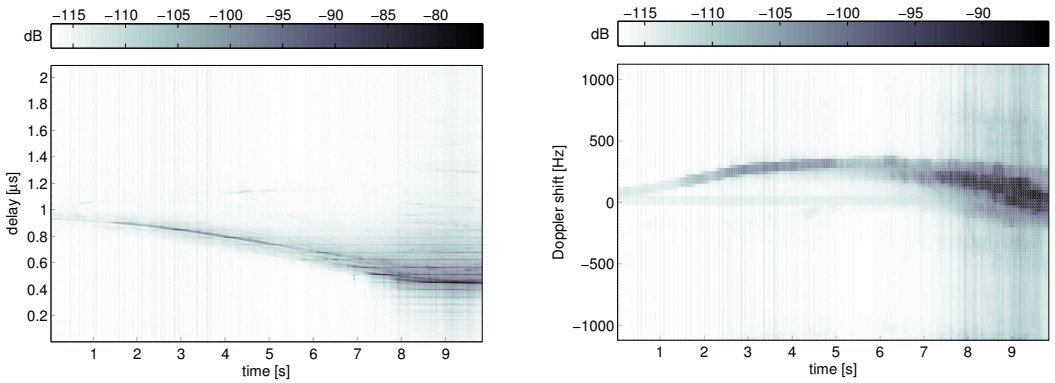

(a) PDP (b) DSD

Figure A.8: Time-varying PDP and DSD for road crossing - urban single lane.

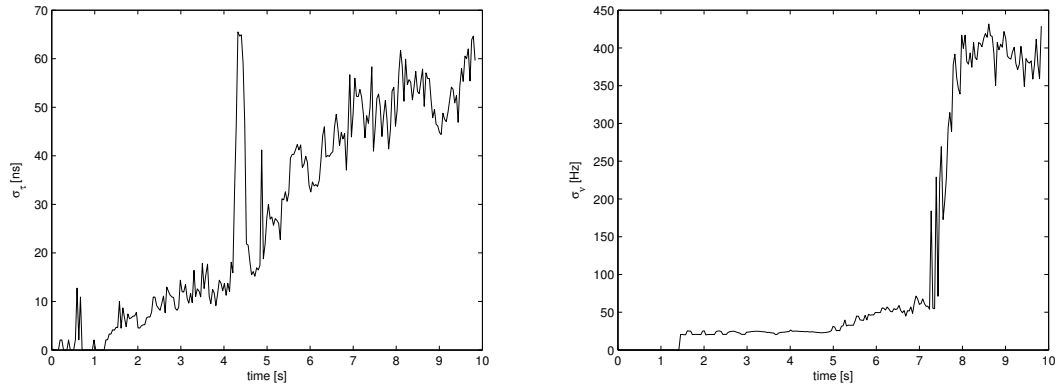

(a) RMS delay spread (b) RMS Doppler spread

Figure A.9: Time-varying channel parameters for road crossing - urban single lane.

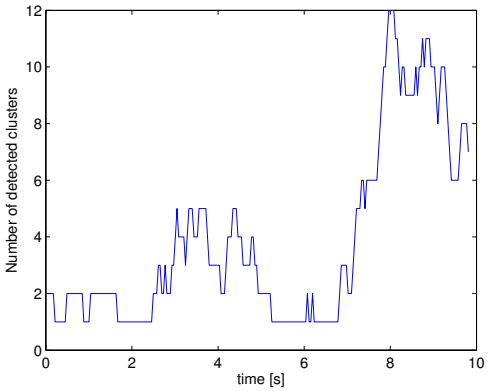

(a) Number of clusters

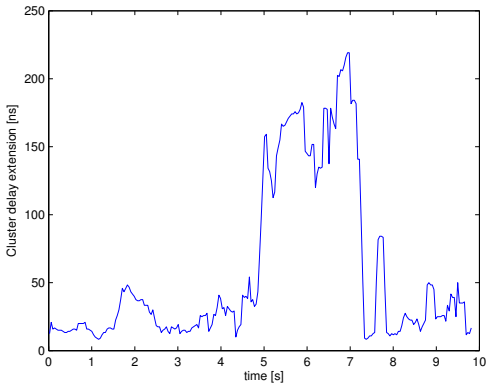

(b) Cluster delay extension - 1st-cluster

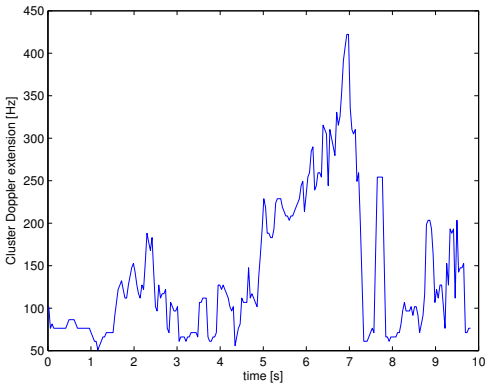

(c) Cluster Doppler extension - 1st-cluster

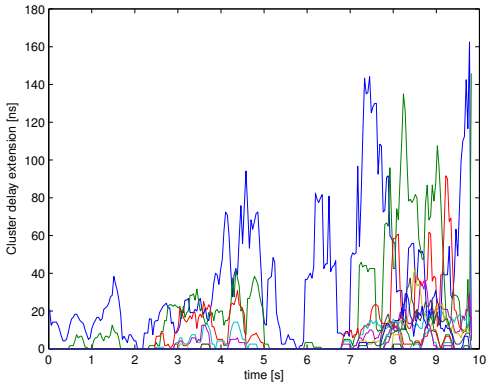

(d) Cluster delay extension - later-clusters

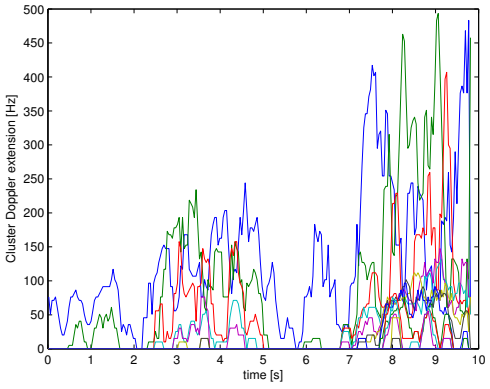

(e) Cluster Doppler extension - later-clusters

Figure A.10: Time-varying cluster parameters for road crossing - urban single lane.

A.1.4 Road Crossing - Urban Multiple Lanes

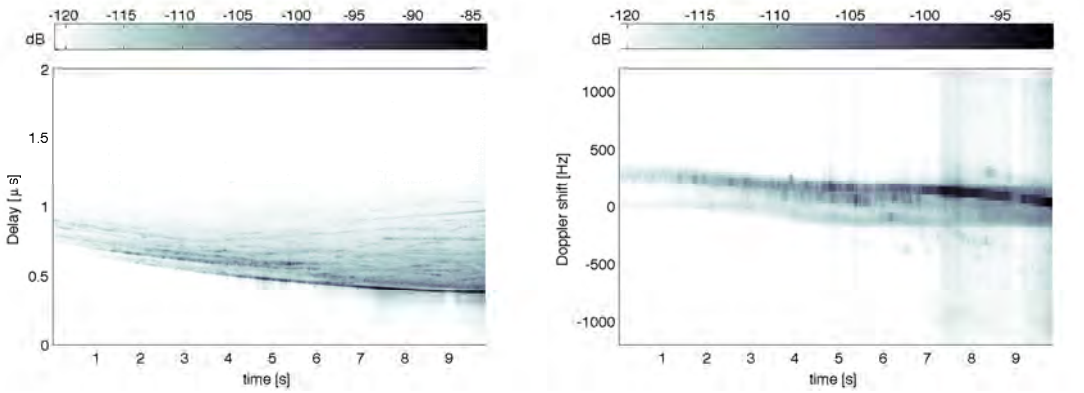

(a) PDP (b) DSD

Figure A.11: Time-varying PDP and DSD for road crossing - urban multiple lane.

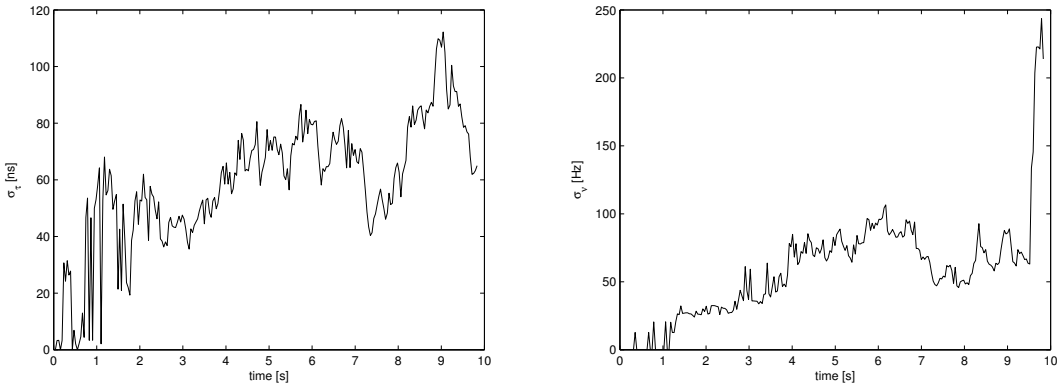

(a) RMS delay spread (b) RMS Doppler spread

Figure A.12: Time-varying channel parameters for road crossing - urban multiple lane.

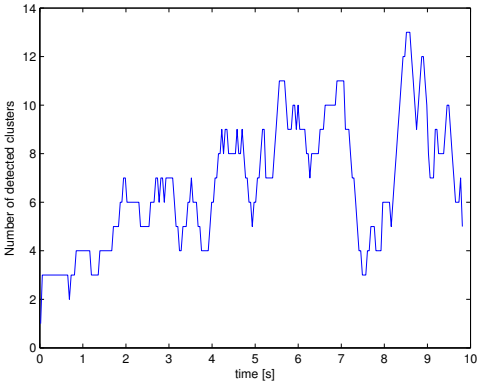

(a) Number of clusters

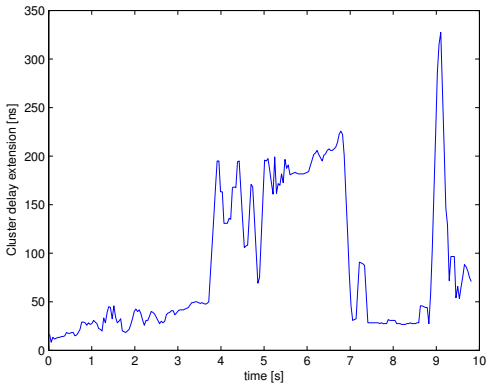

(b) Cluster delay extension - 1st-cluster

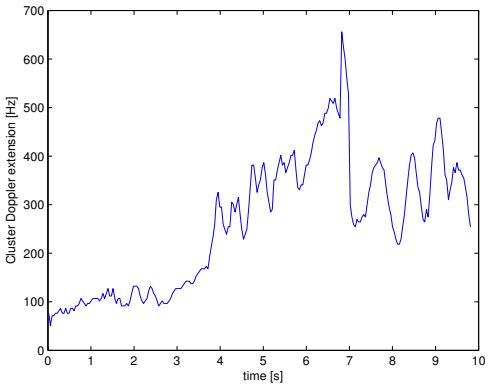

(c) Cluster Doppler extension - 1st-cluster

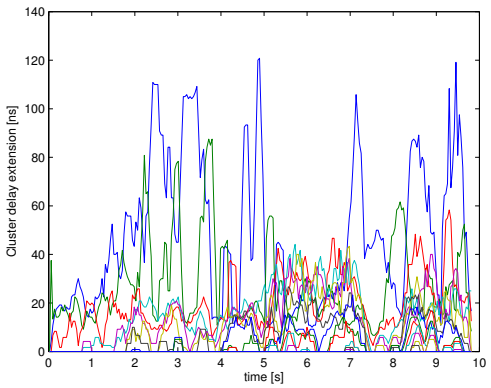

(d) Cluster delay extension - later-clusters

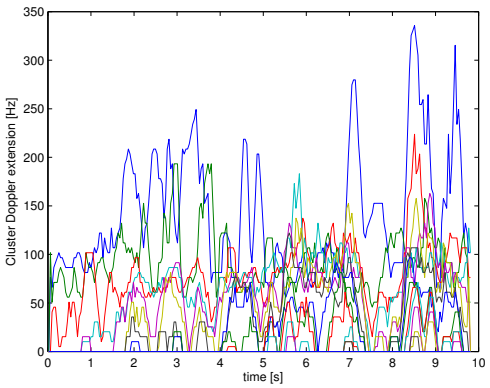

(e) Cluster Doppler extension - later-clusters

Figure A.13: Time-varying cluster parameters for road crossing - urban multiple lane.

A.2 General Line of Sight Obstruction - Highway

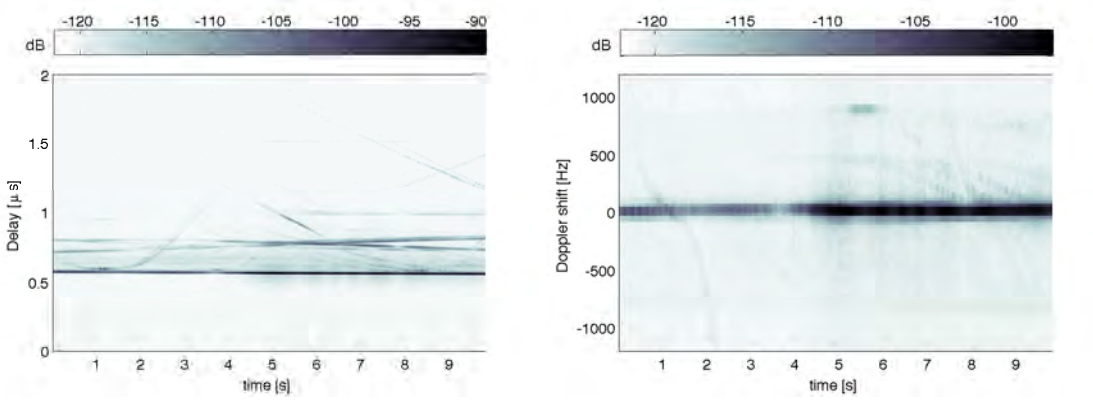

(a) PDP (b) DSD

Figure A.14: Time-varying PDP and DSD for general LOS obstruction - highway.

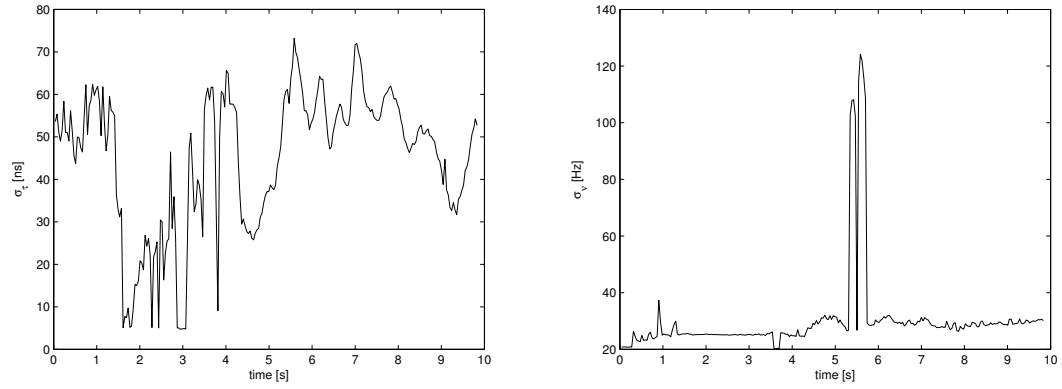

(a) RMS delay spread (b) RMS Doppler spread

Figure A.15: Time-varying channel parameters for general LOS obstruction - highway.

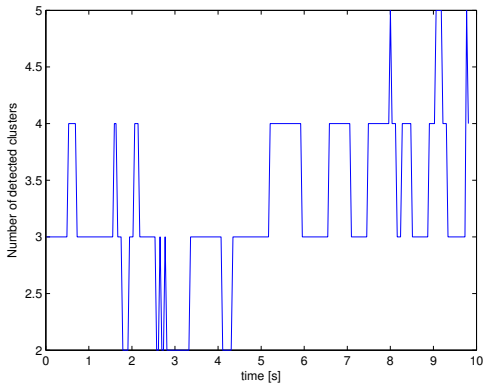

(a) Number of clusters

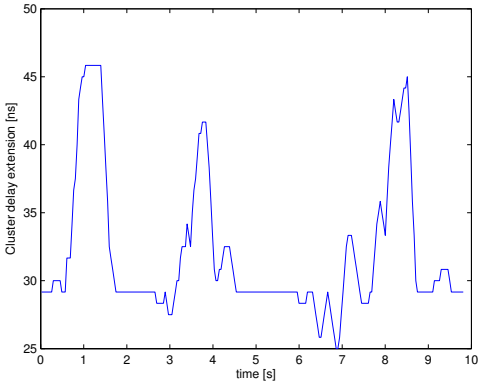

(b) Cluster delay extension - 1st-cluster

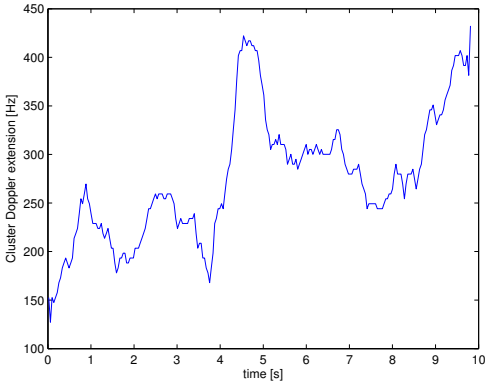

(c) Cluster Doppler extension - 1st-cluster

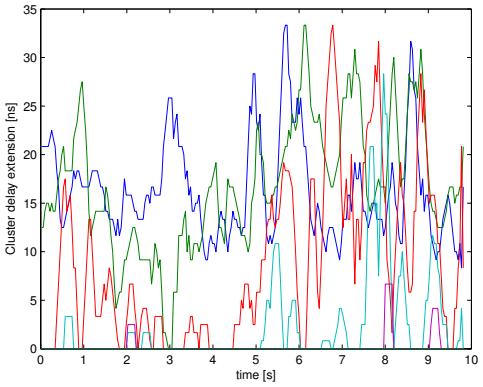

(d) Cluster delay extension - later-clusters

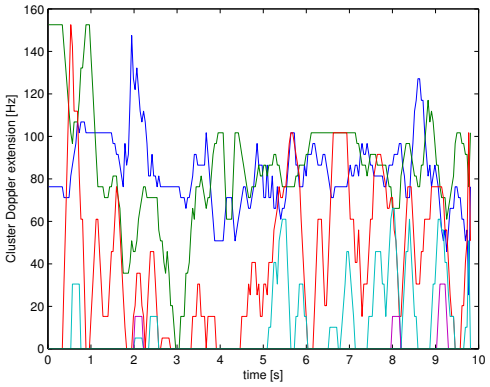

(e) Cluster Doppler extension - later-clusters

Figure A.16: Time-varying cluster parameters for general LOS obstruction - highway.

A.3 Mergin Lanes - Rural

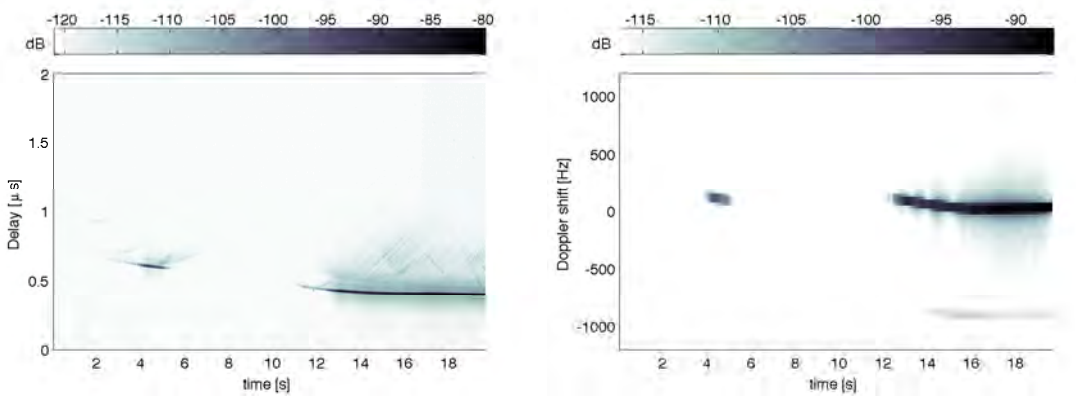

(a) PDP (b) DSD

Figure A.17: Time-varying PDP and DSD for merging lanes - rural.

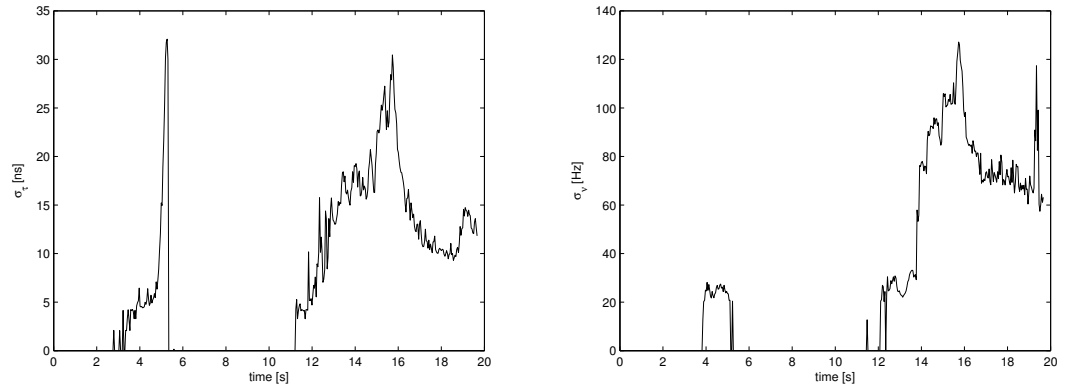

(a) RMS delay spread (b) RMS Doppler spread

Figure A.18: Time-varying channel parameters for merging lanes - rural.

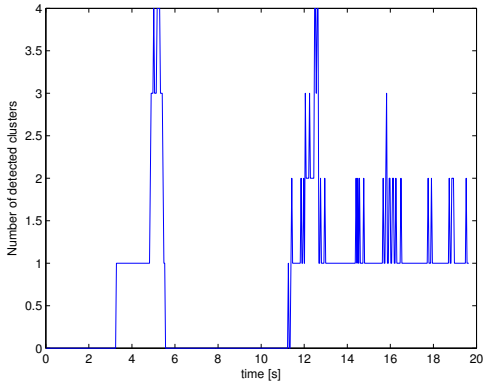

(a) Number of clusters

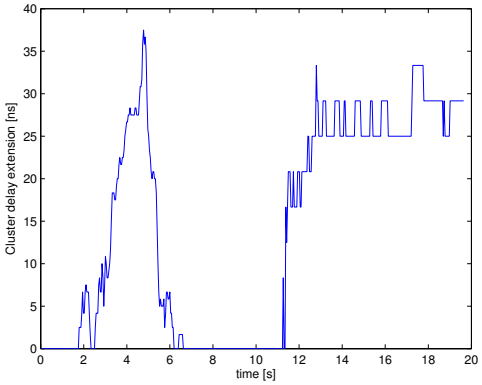

(b) Cluster delay extension - 1st-cluster

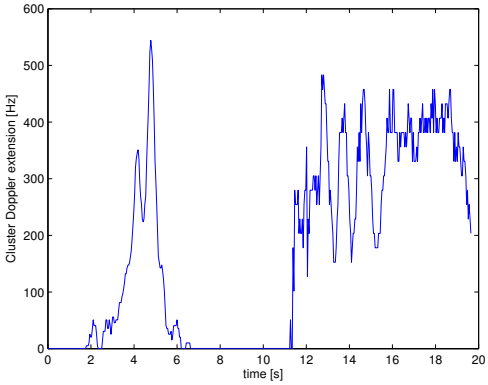

(c) Cluster Doppler extension - 1st-cluster

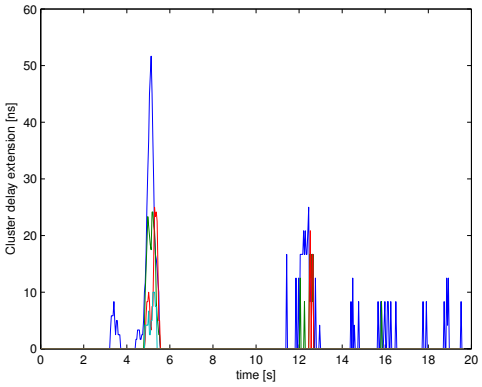

(d) Cluster delay extension - later-clusters

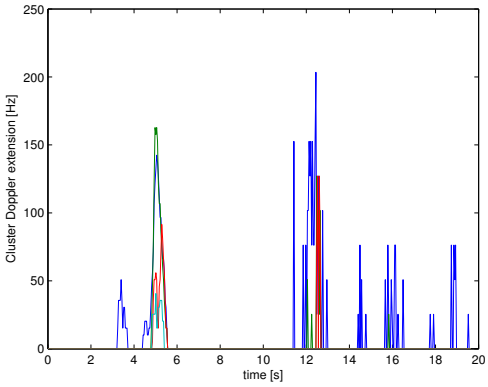

(e) Cluster Doppler extension - later-clusters

Figure A.19: Time-varying cluster parameters for merging lanes - rural.

A.4 Traffic Congestion

A.4.1 Traffic Congestion - Slow Traffic

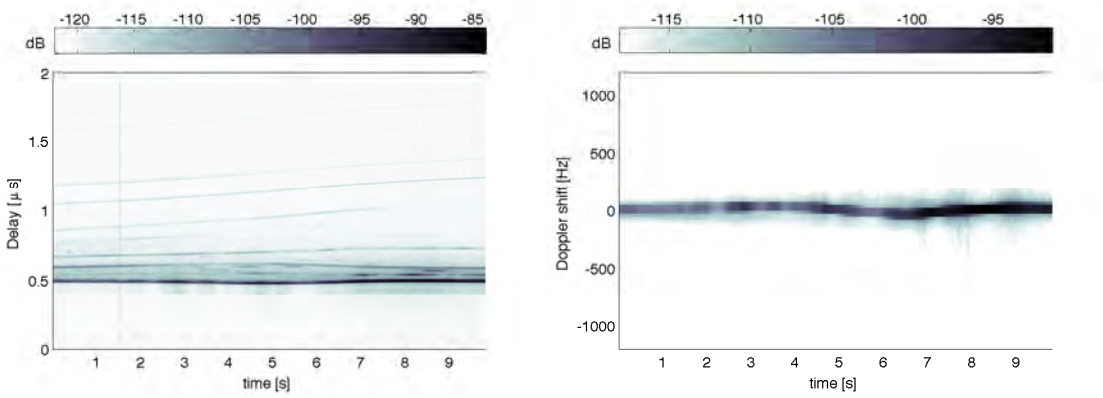

(a) PDP (b) DSD

Figure A.20: Time-varying PDP and DSD for traffic congestion - slow traffic.

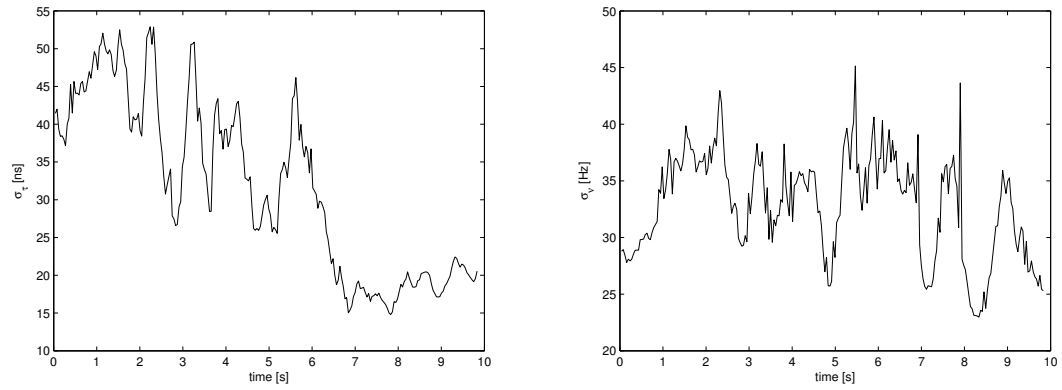

(a) RMS delay spread (b) RMS Doppler spread

Figure A.21: Time-varying channel parameters for traffic congestion - slow traffic.

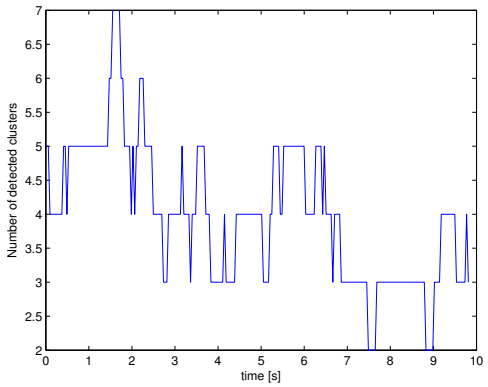

(a) Number of clusters

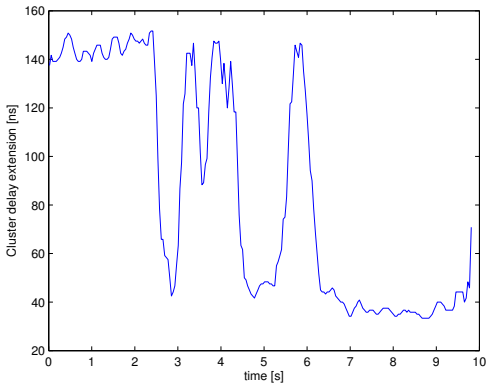

(b) Cluster delay extension - 1st-cluster

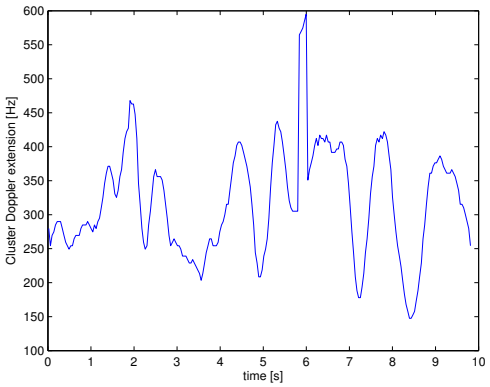

(c) Cluster Doppler extension - 1st-cluster

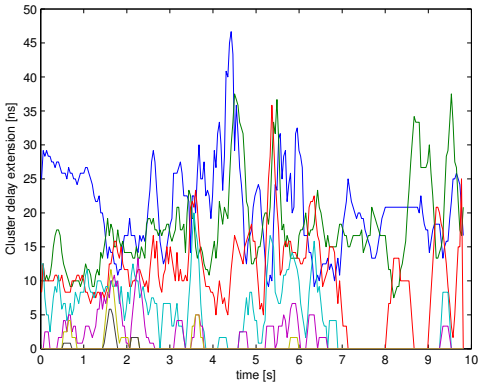

(d) Cluster delay extension - later-clusters

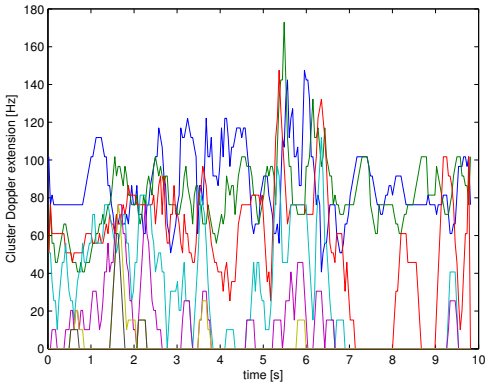

(e) Cluster Doppler extension - later-clusters

Figure A.22: Time-varying cluster parameters for traffic congestion - slow traffic.

A.4.2 Traffic Congestion - Approaching Traffic Jam

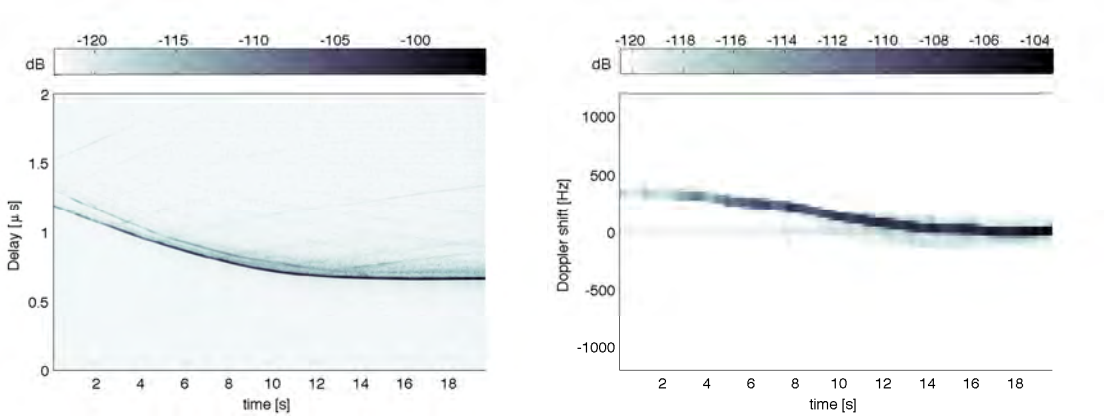

(a) PDP (b) DSD

Figure A.23: Time-varying PDP and DSD for traffic congestion - approaching traffic jam.

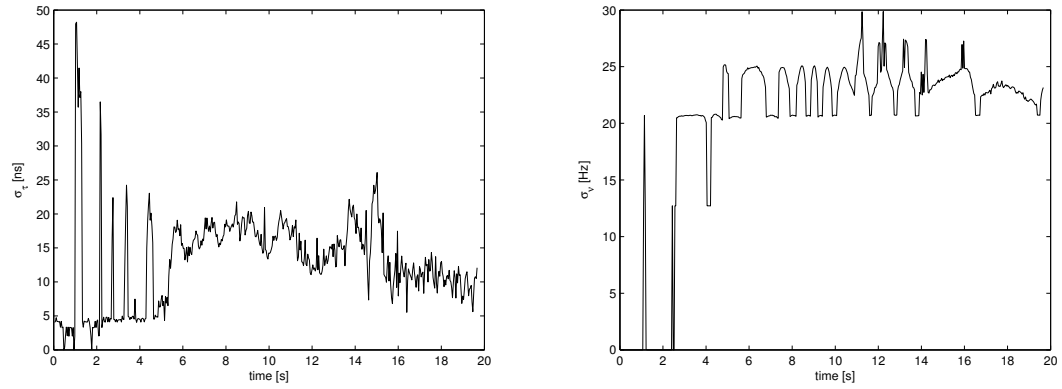

(a) RMS delay spread (b) RMS Doppler spread

Figure A.24: Time-varying channel parameters for traffic congestion - approaching traffic jam.

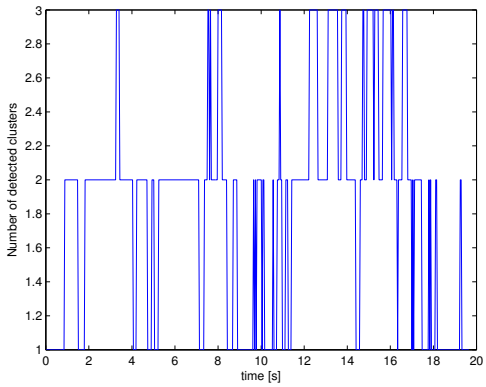

(a) Number of clusters

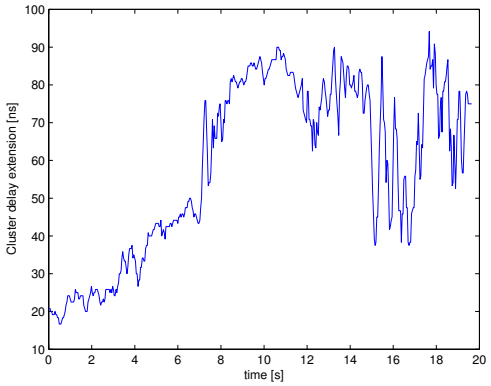

(b) Cluster delay extension - 1st-cluster

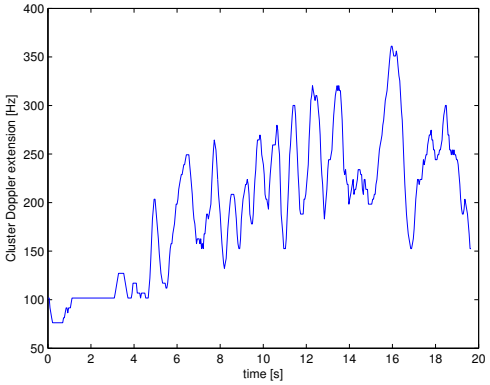

(c) Cluster Doppler extension - 1st-cluster

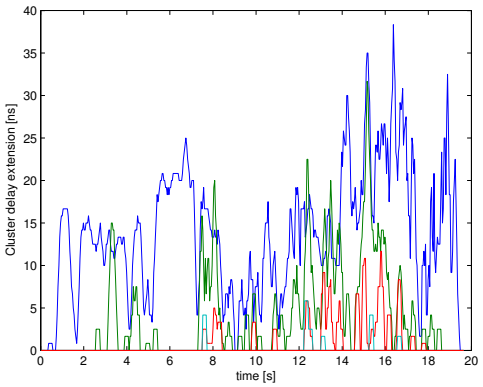

(d) Cluster delay extension - later-clusters

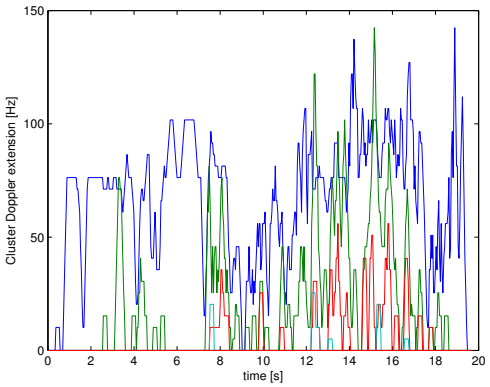

(e) Cluster Doppler extension - later-clusters

Figure A.25: Time-varying cluster parameters for traffic congestion - approaching traffic jam.

A.5 In-Tunnel

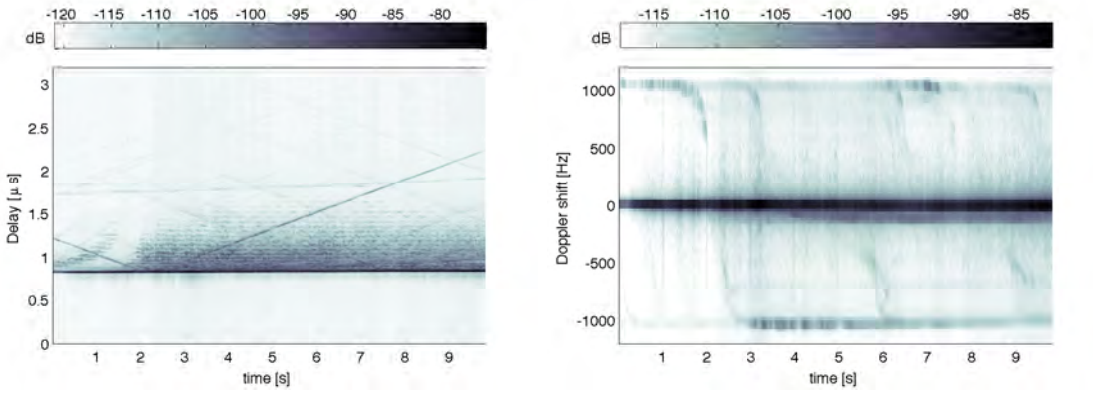

(a) PDP (b) DSD

Figure A.26: Time-varying PDP and DSD for in-tunnel.

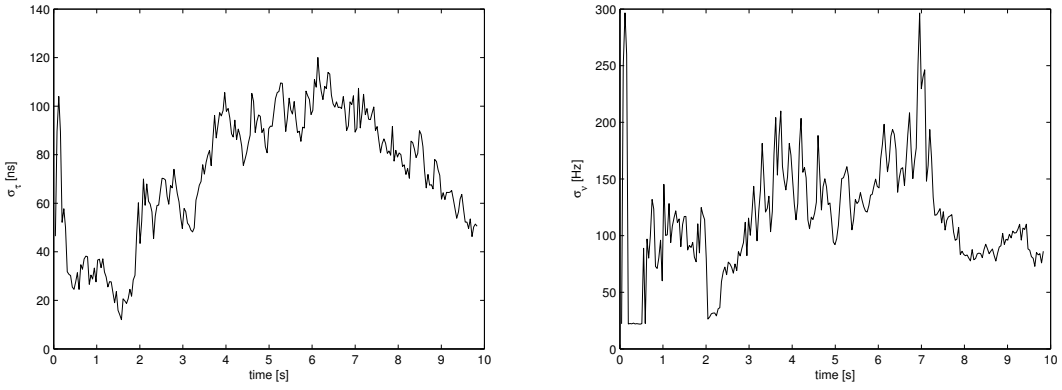

(a) RMS delay spread (b) RMS Doppler spread

Figure A.27: Time-varying channel parameters for in-tunnel.

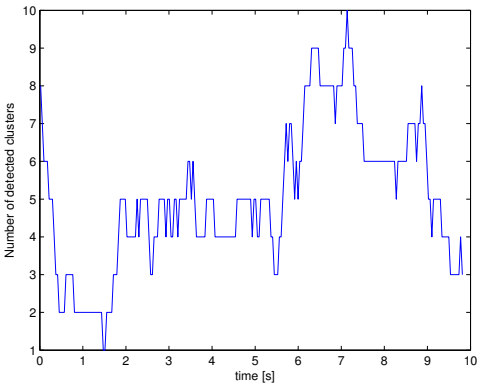

(a) Number of clusters

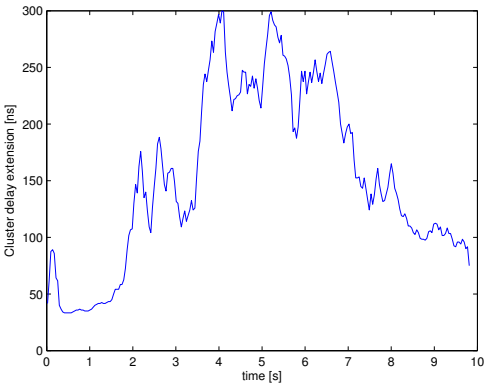

(b) Cluster delay extension - 1st-cluster

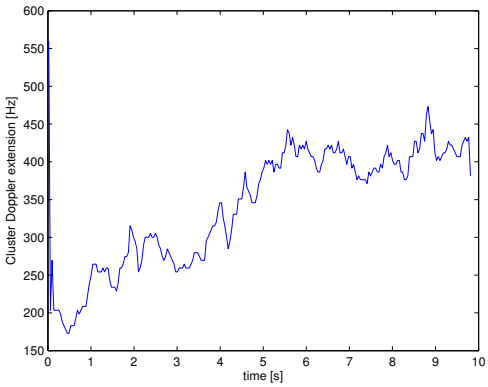

(c) Cluster Doppler extension - 1st-cluster

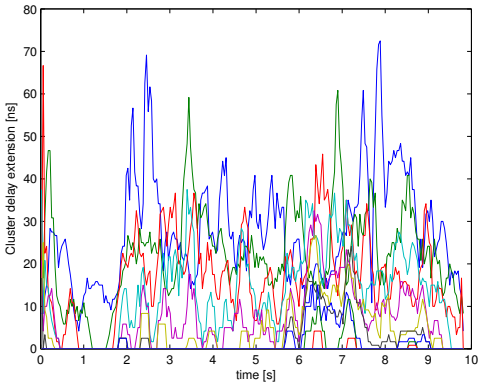

(d) Cluster delay extension - later-clusters

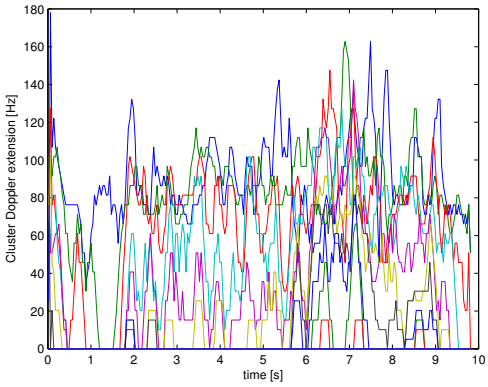

(e) Cluster Doppler extension - later-clusters

Figure A.28: Time-varying cluster parameters for in-tunnel.

A.6 On-Bridge

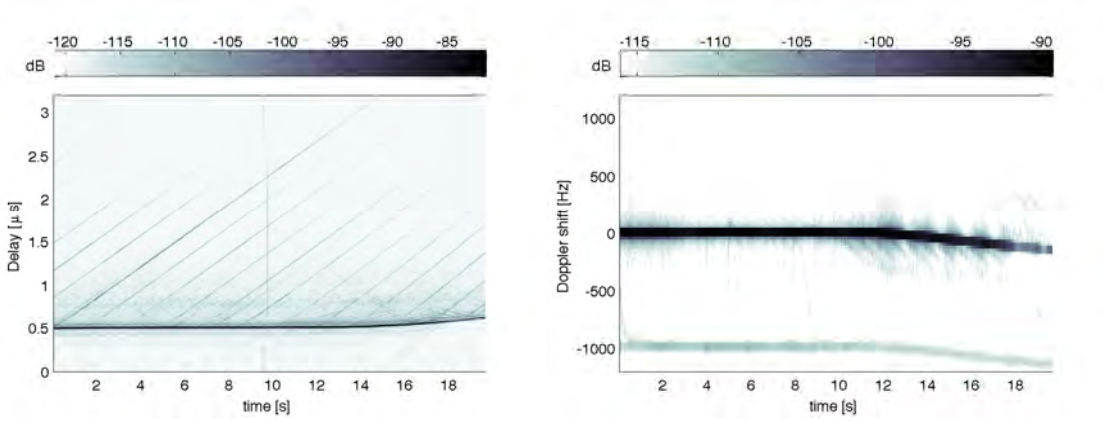

(a) PDP (b) DSD

Figure A.29: Time-varying PDP and DSD for on-bridge.

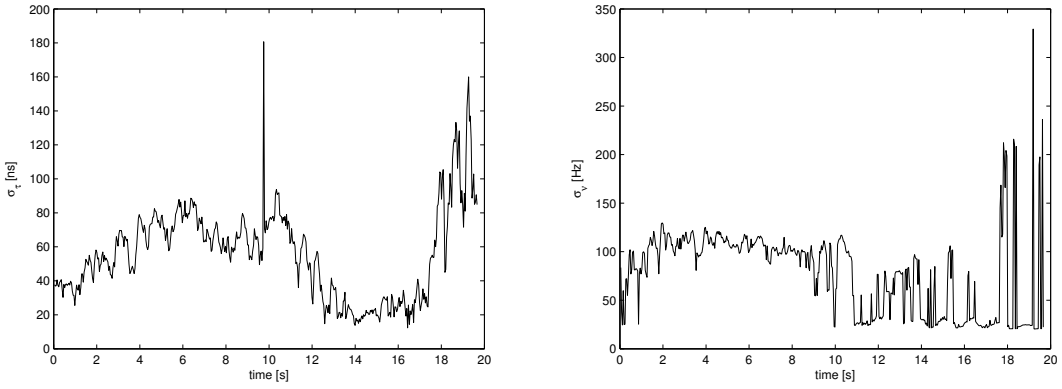

(a) RMS delay spread (b) RMS Doppler spread

Figure A.30: Time-varying channel parameters for on-bridge.

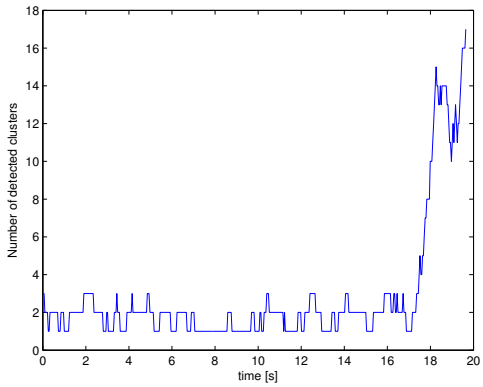

(a) Number of clusters

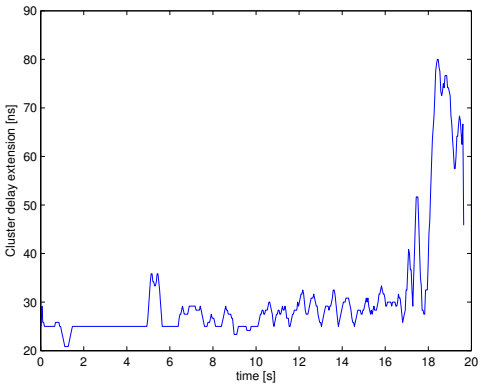

(b) Cluster delay extension - 1st-cluster

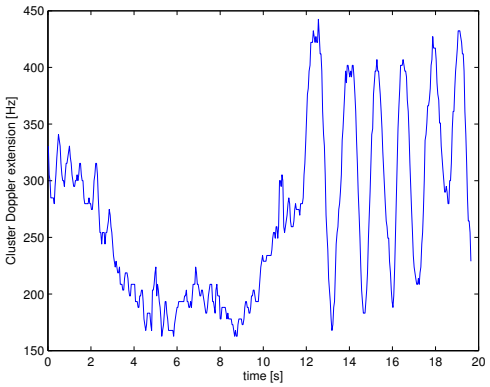

(c) Cluster Doppler extension - 1st-cluster

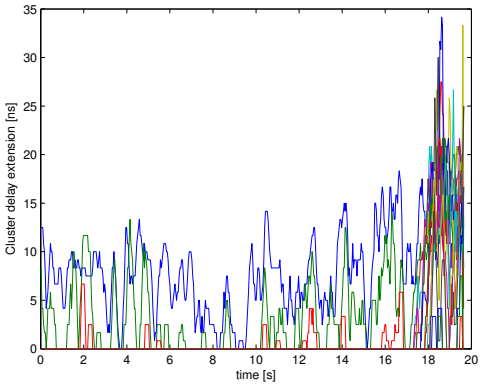

(d) Cluster delay extension - later-clusters

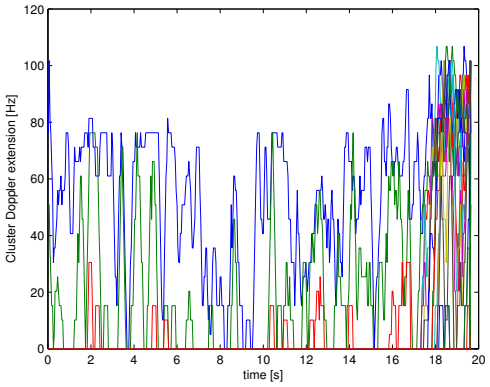

(e) Cluster Doppler extension - later-clusters

Figure A.31: Time-varying cluster parameters for on-bridge.

Bibliography

[1] P. A. Bello, "Characterization of randomly time-variant linear channels," *IEEE Transactions on Communications*, vol. 11, pp. 360–393, 1963.

[2] G. Matz, "On non-WSSUS wireless fading channels," *Wireless Communications, IEEE Transactions on*, vol. 4, no. 5, pp. 2465–2478, September 2005.

[3] L. Bernadó, A. Roma, A. Paier, T. Zemen, N. Czink, J. Karedal, A. Thiel, F. Tufvesson, A. F. Molisch, and C. F. Mecklenbräuker, "In-tunnel vehicular radio channel characterization," in *Vehicular Technology Conference (VTC Spring), 2011 IEEE 73rd*, May 2011, pp. 1 –5.

[4] J. Karedal, N. Czink, A. Paier, F. Tufvesson, and A. Molisch, "Path loss modeling for vehicle-to-vehicle communications," *Vehicular Technology, IEEE Transactions on*, vol. 60, no. 1, pp. 323 –328, January 2011.

[5] N. Czink, F. Kaltenberger, Y. Zhouz, L. Bernadó, T. Zemen, and X. Yinz, "Low-complexity geometry-based modeling of diffuse scattering," in *EUCAP 2010, 4th European Conference on Antennas and Propagation*, April 2010, pp. 1–5.

[6] F. Kaltenberger, T. Zemen, and C. W. Ueberhuber, "Low-complexity geometry-based MIMO channel simulation," *EURASIP J. Adv. Sig. Proc.*, vol. 2007, 2007.

[7] M. Peden, R. Scurfield, D. Sleet, D. Mohan, A. A. Hyder, E. Jarawan, and C. Mathers, *World report on road traffic injury prevention.* Geneva: World Health Organization (WHO), 2004.

[8] I. Davis, J.S. and J. Linnartz, "Vehicle to vehicle rf propagation measurements," in *Signals, Systems and Computers, 1994. 1994 Conference Record of the Twenty-Eighth Asilomar Conference on*, vol. 1, oct-2 nov 1994, pp. 470 –474 vol.1.

[9] R. Punnoose, P. Nikitin, J. Broch, and D. Stancil, "Optimizing wireless network protocols using real-time predictive propagation modeling," in *Radio and Wireless Conference, 1999. RAWCON 99. 1999 IEEE*, 1999, pp. 39 –44.

[10] G. Acosta, K. Tokuda, and M. Ingram, "Measured joint Doppler-delay power profiles for vehicle-to-vehicle communications at 2.4 GHz," in *Global Telecommunications Conference, 2004. GLOBECOM '04. IEEE*, vol. 6, nov.-3 dec. 2004, pp. 3813 – 3817 Vol.6.

[11] G. Acosta and M. A. Ingram, "Model development for the wideband expressway vehicle-to-vehicle 2.4 GHz channel," in *IEEE Wireless Communications and Networking Conference (WCNC) 2006*, 3-6 April 2006.

[12] D. Matolak, I. Sen, W. Xiong, and N. Yaskoff, "5 GHz wireless channel characterization for vehicle to vehicle communications," in *Military Communications Conference, 2005. MILCOM 2005. IEEE*, oct. 2005, pp. 3016 –3022 Vol. 5.

[13] A. da Silva and M. Nakagawa, "Radio wave propagation measurements in tunnel entrance environment for intelligent transportation systems applications," *Intelligent Transportation Systems, IEEE Proceedings*, pp. 883 –888, August 2001.

[14] I. Tan, W. Tang, K. Laberteaux, and A. Bahai, "Measurement and analysis of wireless channel impairments in DSRC vehicular communications," in *Communications, 2008. ICC '08. IEEE International Conference on*, May 2008, pp. 4882–4888.

[15] J. Kunisch and J. Pamp, "Wideband car-to-car radio channel measurements and model at 5.9 GHz," in *Vehicular Technology Conference, 2008. VTC 2008-Fall. IEEE 68th*, September 2008, pp. 1–5.

[16] P. Paschalidis, M. Wisotzki, A. Kortke, W. Keusgen, and M. Peter, "A wideband channel sounder for car-to-car radio channel measurements at 5.7 GHz and results for an urban scenario," in *Vehicular Technology Conference, 2008. VTC 2008-Fall. IEEE 68th*, sept. 2008, pp. 1 –5.

[17] A. Paier, J. Karedal, N. Czink, H. Hofstetter, C. Dumard, T. Zemen, F. Tufvesson, A. Molisch, and C. Mecklenbräuker, "Car-to-car radio channel measurements at 5 GHz: Pathloss, power-delay profile, and delay-Doppler spectrum," in *Wireless Communication Systems, 2007. ISWCS 2007. 4th International Symposium on*, October 2007, pp. 224–228.

[18] A. Paier, L. Bernadó and, J. Karedal, O. Klemp, and A. Kwoczek, "Overview of vehicle-to-vehicle radio channel measurements for collision avoidance applications," in *Vehicular Technology Conference (VTC 2010-Spring), 2010 IEEE 71st*, May 2010, pp. 1–5.

[19] O. Renaudin, V.-M. Kolmonen, P. Vainikainen, and C. Oestges, "Wideband MIMO car-to-car radio channel measurements at 5.3 GHz," in *Vehicular Technology Conference, 2008. VTC 2008-Fall. IEEE 68th*, September 2008, pp. 1–5.

[20] F. Pallares, F. Juan, and L. Juan-Llacer, "Analysis of path loss and delay spread at 900 MHz and 2.1 GHz while entering tunnels," *Vehicular Technology, IEEE Transactions on*, vol. 50, no. 3, pp. 767 –776, May 2001.

[21] D. Dudley, M. Lienard, S. Mahmoud, and P. Degauque, "Wireless propagation in tunnels," *Antennas and Propagation Magazine, IEEE*, vol. 49, no. 2, pp. 11 –26, April 2007.

[22] J. Maurer, T. Fugen, and W. Wiesbeck, "Narrow-band measurement and analysis of the inter-vehicle transmission channel at 5.2 GHz," in *Vehicular Technology Conference, 2002. VTC Spring 2002. IEEE 55th*, vol. 3, 2002, pp. 1274–1278.

[23] D. W. Matolak, I. Sen, and W. Xiong, "Channel modeling for v2v communications," in *Mobile and Ubiquitous Systems - Workshops, 2006. 3rd Annual International Conference on*, july 2006, pp. 1 –7.

[24] J. Yin, G. Holland, T. ElBatt, F. Bai, and H. Krishnan, "DSRC channel fading analysis from empirical measurement," in *Communications and Networking in China, 2006. ChinaCom '06. First International Conference on*, oct. 2006, pp. 1 –5.

[25] G. Acosta-Marum and M. Ingram, "Six time- and frequency- selective empirical channel models for vehicular wireless LANs," *Vehicular Technology Magazine, IEEE*, vol. 2, no. 4, pp. 4–11, December 2007.

[26] P. Paschalidis, K. Mahler, A. Kortke, M. Wisotzki, M. Peter, and W. Keusgen, "2 x 2 MIMO measurements of the wideband car-to-car channel at 5.7 GHz on urban street intersections," in *Vehicular Technology Conference (VTC Fall), 2011 IEEE*, sept. 2011, pp. 1 –5.

[27] L. Cheng, B. Henty, D. Stancil, F. Bai, and P. Mudalige, "Mobile vehicle-to-vehicle narrow-band channel measurement and characterization of the 5.9 GHz Dedicated Short Range Communication (DSRC) frequency band," *Selected Areas in Communications, IEEE journal on*, vol. 25, no. 8, pp. 1501–1516, October 2007.

[28] J. Karedal, F. Tufvesson, T. Abbas, O. Klemp, A. Paier, L. Bernadó, and A. Molisch, "Radio channel measurements at street intersections for vehicle-to-vehicle safety applications," in *Vehicular Technology Conference (VTC 2010-Spring), 2010 IEEE 71st*, may 2010, pp. 1 –5.

[29] P. Paschalidis, K. Mahler, A. Kortke, M. Peter, and W. Keusgen, "Pathloss and multipath power decay of the wideband car-to-car channel at 5.7 GHz," in *Vehicular Technology Conference (VTC Spring), 2011 IEEE 73rd*, May 2011, pp. 1–5.

[30] L. Cheng, B. Henty, F. Bai, and D. Stancil, "Highway and rural propagation channel modeling for vehicle-to-vehicle communications at 5.9 GHz," in *Antennas and Propagation Society International Symposium, 2008. AP-S 2008. IEEE*, July 2008, pp. 1–4.

[31] I. Sen and D. Matolak, "Vehicle-vehicle channel models for the 5-GHz band," *Intelligent Transportation Systems, IEEE Transactions on*, vol. 9, no. 2, pp. 235–245, June 2008.

[32] O. Renaudin, V.-M. Kolmonen, P. Vainikainen, and C. Oestges, "Wideband measurement-based modeling of inter-vehicle channels in the 5 GHz band," in *Antennas and Propagation (EUCAP), Proceedings of the 5th European Conference on*, April 2011, pp. 2881–2885.

[33] J. Karedal, F. Tufvesson, N. Czink, A. Paier, C. Dumard, T. Zemen, C. Mecklenbräuker, and A. Molisch, "A geometry-based stochastic MIMO model for vehicle-to-vehicle communications," *Wireless Communications, IEEE Transactions on*, vol. 8, no. 7, pp. 3646–3657, July 2009.

[34] J. Maurer, T. Fugen, T. Schafer, and W. Wiesbeck, "A new inter-vehicle communications (IVC) channel model," in *Vehicular Technology Conference, 2004. VTC2004-Fall. 2004 IEEE 60th*, vol. 1, September 2004, pp. 9–13.

[35] L. Reichardt, J. Maurer, T. Fugen, and T. Zwick, "Virtual drive: A complete V2X communication and radar system simulator for optimization of multiple antenna systems," *Proceedings of the IEEE*, vol. 99, no. 7, pp. 1295 –1310, July 2011.

[36] J. Pontes, L. Reichardt, and T. Zwick, "Investigation on antenna systems for car-to-car communication," *Selected Areas in Communications, IEEE Journal on*, vol. 29, no. 1, pp. 7–14, January 2011.

[37] F. Vatalaro and A. Forcella, "Doppler spectrum in mobile-to-mobile communications in the presence of three-dimensional multipath scattering," *Vehicular Technology, IEEE Transactions on*, vol. 46, no. 1, pp. 213–219, February 1997.

[38] "IEEE P802.11p: Part 11: Wireless LAN Medium Access Control (MAC) and Physical Layer (PHY) Specifications: Amendment 6: Wireless Access in Vehicular Environments," July 2010.

[39] M. Pätzold, B. Hogstad, and N. Youssef, "Modeling, analysis, and simulation of MIMO mobile-to-mobile fading channels," *Wireless Communications, IEEE Transactions on*, vol. 7, no. 2, pp. 510–520, February 2008.

[40] A. Zajic and G. Stuber, "Three-dimensional modeling, simulation, and capacity analysis of space-time correlated mobile-to-mobile channels," *Vehicular Technology, IEEE Transactions on*, vol. 57, no. 4, pp. 2042–2054, July 2008.

[41] X. Cheng, C.-X. Wang, D. Laurenson, S. Salous, and A. Vasilakos, "An adaptive geometry-based stochastic model for non-isotropic MIMO mobile-to-mobile channels," *Wireless Communications, IEEE Transactions on*, vol. 8, no. 9, pp. 4824–4835, September 2009.

[42] L.-C. Wang, W.-C. Liu, and Y.-H. Cheng, "Statistical analysis of a mobile-to-mobile rician fading channel model," *Vehicular Technology, IEEE Transactions on*, vol. 58, no. 1, pp. 32–38, January 2009.

[43] A. Chelli and M. Patzold, "The impact of fixed and moving scatterers on the statistics of MIMO vehicle-to-vehicle channels," in *Vehicular Technology Conference, 2009. VTC Spring 2009. IEEE 69th*, April 2009, pp. 1–6.

[44] P. Petrus, J. Reed, and T. Rappaport, "Geometrical-based statistical macrocell channel model for mobile environments," *Communications, IEEE Transactions on*, vol. 50, no. 3, pp. 495–502, March 2002.

[45] L. M. Correia, "COST 273 Final Report: Mobile Broadband Multimedia Networks," 2006.

[46] N. Czink and C. Oestges, "The COST 273 MIMO channel model: Three kinds of clusters," in *Spread Spectrum Techniques and Applications, 2008. ISSSTA '08. IEEE 10th International Symposium on*, aug. 2008, pp. 282 –286.

[47] H. Hofstetter, A. Molisch, and N. Czink, "A twin-cluster MIMO channel model," in *Antennas and Propagation, 2006. EuCAP 2006. First European Conference on*, nov. 2006, pp. 1 –8.

[48] A. Kumar, R. Bhattacharjee, and S. Goel, "A clustering based channel model for indoor wireless communication," in *Communications (NCC), 2011 National Conference on*, jan. 2011, pp. 1 –5.

[49] N. Czink, E. Bonek, L. Hentila, P. Kyosti, J.-P. Nuutinen, and J. Ylitalo, "The interdependence of cluster parameters in MIMO channel modeling," in *Antennas and Propagation, 2006. EuCAP 2006. First European Conference on*, nov. 2006, pp. 1 –6.

[50] C. Chen and M. Jensen, "A stochastic model of the time-variant MIMO channel based on experimental observations," *Vehicular Technology, IEEE Transactions on*, vol. 58, no. 6, pp. 2618 –2625, july 2009.

[51] S. Wyne, N. Czink, J. Karedal, P. Almers, F. Tufvesson, and A. Molisch, "A cluster-based analysis of outdoor-to-indoor office MIMO measurements at 5.2 GHz," in *Vehicular Technology Conference, 2006. VTC-2006 Fall. 2006 IEEE 64th*, sept. 2006, pp. 1 –5.

[52] L. Hentila, M. Alatossava, N. Czink, and P. Kyosti, "Cluster-level parameters at 5.25 GHz indoor-to-outdoor and outdoor-to-indoor MIMO radio channels," in *Mobile and Wireless Communications Summit, 2007. 16th IST*, july 2007, pp. 1 –5.

[53] G. Dahman, R. Bultitude, and R. Hafez, "Identifying and modelling multipath clusters in propagation measurement data," in *Vehicular Technology Conference Fall (VTC 2010-Fall), 2010 IEEE 72nd*, sept. 2010, pp. 1 –5.

[54] Y. Oda and T. Taga, "Clustering of local scattered multipath components in urban mobile environments," in *Vehicular Technology Conference, 2002. VTC Spring 2002. IEEE 55th*, vol. 1, 2002, pp. 11 – 15 vol.1.

[55] G. Matz, "Doubly underspread non-WSSUS channels: Analysis and estimation of channel statistics," Rome, Italy, June 2003, pp. 190–194.

[56] A. Gehring, M. Steinbauer, I. Gaspard, and M. Grigat, "Empirical channel stationarity in urban environments," in *Proc. Eur. Personal Mobile Communications Conf. (EPMCC)*, Vienna, Austria, February 2001.

[57] M. Herdin, N. Czink, H. Ozcelik, and E. Bonek, "Correlation matrix distance, a meaningful measure for evaluation of non-stationary MIMO channels," in *Vehicular Technology Conference, 2005. VTC 2005-Spring. 2005 IEEE 61st*, vol. 1, May-June 2005, pp. 136–140.

[58] R. Kattenbach, "Charakterisierung zeitvarianter Indoor-Funkkanle anhand ihrer System- und Korrelationsfunktionen," Ph.D. dissertation, Universität Gesamthochschule Kassel, 1997.

[59] A. Paier, T. Zemen, L. Bernadó, G. Matz, J. Karedal, N. Czink, C. Dumard, F. Tufvesson, A. F. Molisch, and C. F. Mecklenbräuker, "Non-WSSUS vehicular channel characterization in highway and urban scenarios at 5.2 GHz using the local scattering function," in *Smart Antennas, 2008. WSA 2008. International ITG Workshop on*, February 2008, pp. 9–15.

[60] O. Renaudin, V.-M. Kolmonen, P. Vainikainen, and C. Oestges, "Non-stationary narrowband MIMO inter-vehicle channel characterization in the 5-GHz band," *Vehicular Technology, IEEE Transactions on*, vol. 59, no. 4, pp. 2007–2015, May 2010.

[61] A. Ispas, G. Ascheid, C. Schneider, and R. Thoma, "Analysis of local quasi-stationarity regions in an urban macrocell scenario," in *Vehicular Technology Conference (VTC 2010-Spring), 2010 IEEE 71st*, may 2010, pp. 1 –5.

[62] T. Willink, "Wide-sense stationarity of mobile MIMO radio channels," *Vehicular Technology, IEEE Transactions on*, vol. 57, no. 2, pp. 704 –714, march 2008.

[63] D. Umansky and M. Patzold, "Stationarity test for wireless communication channels," in *Global Telecommunications Conference, 2009. GLOBECOM 2009. IEEE*, 30 2009-dec. 4 2009, pp. 1 –6.

[64] S. Kay, "A new nonstationarity detector," *Signal Processing, IEEE Transactions on*, vol. 56, no. 4, pp. 1440 –1451, april 2008.

[65] U. Chude-Okonkwo, R. Ngah, and T. Abd Rahman, "Time-scale domain characterization of non-WSSUS wideband channels," *EURASIP Journal on Advances in Signal Processing*, vol. 2011, no. 1, p. 123, 2011.

[66] L. Bernadó, T. Zemen, A. Paier, G. Matz, J. Karedal, N. Czink, F. Tufvesson, M. Hagenauer, A. F. Molisch, and C. F. Mecklenbräuker, "Non-WSSUS Vehicular Channel Characterization at 5.2 GHz - Spectral Divergence and Time-Variant Coherence Parameters," in *Assembly of the International Union of Radio Science (URSI)*, aug 2008, pp. 9–15.

[67] L. Bernadó, T. Zemen, A. Paier, J. Karedal, and B. Fleury, "Parametrization of the local scattering function estimator for vehicular-to-vehicular channels,"

in *Vehicular Technology Conference Fall (VTC 2009-Fall), 2009 IEEE 70th*, September 2009, pp. 1–5.

[68] L. Bernadó and, T. Zemen, J. Karedal, A. Paier, A. Thiel, O. Klemp, N. Czink, F. Tufvesson, A. Molisch, and C. Mecklenbräuker, "Multi-dimensional K-factor analysis for V2V radio channels in open sub-urban street crossings," in *Personal Indoor and Mobile Radio Communications (PIMRC), 2010 IEEE 21st International Symposium on*, sept. 2010, pp. 58 –63.

[69] L. Bernadó, T. Zemen, A. Paier, and J. Karedal, "Complexity reduction for vehicular channel estimation using the filter-divergence measure," in *Asilomar Conference on Signals, Systems, and Computers, November 7-10, 2010*, November 2010, pp. 1–5.

[70] L. Bernadó, A. Roma, N. Czink, A. Paier, and T. Zemen, "Cluster-based scatterer identification and characterization in vehicular channels," *Wireless Conference 2011 - Sustainable Wireless Technologies (European Wireless), 11th European*, pp. 1 –6, april 2011.

[71] L. Bernadó and, T. Zemen, F. Tufvesson, A. Molisch, and C. Mecklenbräuker, "The (in-)validity of the WSSUS assumption in vehicular channels," in *Personal Indoor and Mobile Radio Communications (PIMRC), 2012 IEEE 23rd International Symposium on,* submitted, sept. 2012.

[72] L. Bernadó, N. Czink, T. Zemen, A. Paier, C. F. Mecklenbräuker, and A. F. Molisch, *Vehicular Channels in the book: LTE Advanced and Beyond Wireless Networks: Channel Modeling and Propagation,* to be published. John Wiley & Sons Ltd., 2012.

[73] N. Czink, "The random-cluster model – a stochastic MIMO channel model for broadband wireless communication systems of the 3rd generation and beyond," Ph.D. dissertation, 2007.

[74] M. Ester, H.-P. Kriegel, J. Sander, and X. Xu, "A density-based algorithm for discovering clusters in large spatial databases with noise," *2nd ACM International Conference on Knowledge Discovery and Data Mining (KDD)*, August.

[75] "MEDAV GmbH," http://www.medav.de.

[76] R. Thomä, D. Hampicke, A. Richter, G. Sommerkorn, A. Schneider, U. Trautwein, and W. Wirnitzer, "Identification of time-variant directional mo-

bile radio channels," *Instrumentation and Measurement, IEEE Transactions on*, vol. 49, no. 2, pp. 357 –364, apr 2000.

[77] A. Thiel, O. Klemp, A. Paiera, L. Bernado, J. Karedal, and A. Kwoczek, "In-situ vehicular antenna integration and design aspects for vehicle-to-vehicle communications," in *Antennas and Propagation (EuCAP), 2010 Proceedings of the Fourth European Conference on*, april 2010, pp. 1 –5.

[78] A. Paier, "The Vehicular Radio Channel in the 5 GHz Band," Ph.D. dissertation, Vienna University of Technology, 2010.

[79] G. Matz, A. F. Molisch, F. Hlawatsch, M. Steinbauer, and I. Gaspard, "On the systematic measurement errors of correlative mobile radio channel sounders," *IEEE Transactions on Communications*, vol. vol. 50, no. no. 5, pp. 808–821, 2002.

[80] J. S. Bendat and A. G. Piersol, *Engineering Applications of Correlation and Spectral Analysis*. John Wiley & Sons, Inc, 1963.

[81] D. Percival and A. Walden, *Spectral analysis for physical applications: multitaper and conventional univariate techniques*, ser. Spectral Analysis for Physical Applications: Multitaper and Conventional Univariate Techniques. Cambridge University Press, 1993.

[82] D. Thomson, "Spectrum estimation and harmonic analysis," *Proceedings of the IEEE*, vol. 70, no. 9, pp. 1055–1096, September 1982.

[83] D. Slepian, "Prolate spheroidal wave functions, Fourier analysis, and uncertainty - V: The discrete case," *The Bell System Technical Journal*, vol. 57, no. 5, pp. 1371–1430, May-June 1978.

[84] A. Molisch, *Wireless Communications*. John Wiley & Sons Ltd., 2005.

[85] S. Kaiser, "Multi-carrier CDMA mobile radio systems-analysis and optimization of detection, decoding and channel estimation," Ph.D. dissertation, German Aerospace Center (DLR). Institute of Communications and Navigation, Germany, 1998.

[86] N. Wiener, *Extrapolation, Interpolation and Smoothing of Stationary Time Series*. New York Wiley, 1963.

[87] T. T. Georgiou, "Distances and Riemannian metrics for spectral density functions," *Signal Processing, IEEE journal on*, vol. 55, no. 8, pp. 3995–4003, August 2007.

[88] M. Steinbauer, "The Radio Propagation Channel - A Non-Directional, Directional, and Double-Directional Point-of-View," Ph.D. dissertation, Vienna University of Technology, 2001.

[89] S. Rice, *Statistical properties of a sine wave plus random noise*, ser. Technical publications: Monograph. Bell Telephone Laboratories, 1948, vol. 27.

[90] R. H. Clarke, *A statistical theory of mobile-radio reception.* Bell Telephone Laboratories, 1968, vol. 47.

[91] G. G. Messier and J. A. Hartwell, "An Empirical Model for Nonstationary Ricean Fading," *Vehicular Technology, IEEE Transactions on*, vol. 58, no. 1, pp. 14–20, January 2009.

[92] L. J. Greenstein, S. Michelson, D. G., and V. Erceg, "Moment-method estimation of the Ricean K-factor," vol. 3, no. 6, June 1999, pp. 175–176.

[93] C. Oestges, N. Czink, B. Bandemer, P. Castiglione, F. Kaltenberger, and A. J. Paulraj, "Experimental characterization and modeling of outdoor-to-indoor and indoor-to-indoor distributed channels," *Vehicular Technology, IEEE Transactions on*, vol. 59, no. 5, pp. 2253 –2265, jun 2010.

[94] A. F. Molisch and M. Steinbauer, "Condensed parameters for characterizing wideband mobile radio channels," *International Journal of Wireless Information Networks*, vol. 6, pp. 133–154, 1999, 10.1023/A:1018895720076.

[95] B. Fleury, "An uncertainty relation for WSS processes and its application to WSSUS systems," *Communications, IEEE Transactions on*, vol. 44, no. 12, pp. 1632 –1634, dec 1996.

[96] M. Toeltsch, J. Laurila, K. Kalliola, A. Molisch, P. Vainikainen, and E. Bonek, "Statistical characterization of urban spatial radio channels," *Selected Areas in Communications, IEEE Journal on*, vol. 20, no. 3, pp. 539 –549, apr 2002.

[97] L. Vuokko, P. Vainikainen, and J. Takada, "Clusters extracted from measured propagation channels in macrocellular environments," *Antennas and Propagation, IEEE Transactions on*, vol. 53, no. 12, pp. 4089 – 4098, dec. 2005.